nature aging

Article

https://doi.org/10.1038/s43587-025-00823-3

Subcellular proteomics and iPSC modeling uncover reversible mechanisms of axonal pathology in Alzheimer's disease

Received: 18 April 2024

Accepted: 29 January 2025

Published online: 10 March 2025

Check for updates

Yifei Cai[1] ✉, Jean Kanyo[2,15], Rashaun Wilson[2,15], Shveta Bathla[3,4,15], Pablo Leal Cardozo[4,15], Lei Tong[1,15], Shanshan Qin[5,15], Lukas A. Fuentes[6,15], Iguaracy Pinheiro-de-Sousa[7,15], Tram Huynh[1,15], Liyuan Sun[1,15], Mohammad Shahid Mansuri[3,4], Zichen Tian[1], Hao-Ran Gan[1], Amber Braker[8], Hoang Kim Trinh[1], Anita Huttner[9], TuKiet T. Lam[2,3,10], Evangelia Petsalaki[7], Kristen J. Brennand[4,11], Angus C. Nairn[3,4,12] & Jaime Grutzendler[1,13,14] ✉

Dystrophic neurites (also termed axonal spheroids) are found around amyloid deposits in Alzheimer's disease (AD), where they impair axonal electrical conduction, disrupt neural circuits and correlate with AD severity. Despite their importance, the mechanisms underlying spheroid formation remain incompletely understood. To address this, we developed a proximity labeling approach to uncover the proteome of spheroids in human postmortem and mouse brains. Additionally, we established a human induced pluripotent stem cell (iPSC)-derived AD model enabling mechanistic investigation and optical electrophysiology. These complementary approaches revealed the subcellular molecular architecture of spheroids and identified abnormalities in key biological processes, including protein turnover, cytoskeleton dynamics and lipid transport. Notably, the PI3K/AKT/mTOR pathway, which regulates these processes, was activated in spheroids. Furthermore, phosphorylated mTOR levels in spheroids correlated with AD severity in humans. Notably, mTOR inhibition in iPSC-derived neurons and mice ameliorated spheroid pathology. Altogether, our study provides a multidisciplinary toolkit for investigating mechanisms and therapeutic targets for axonal pathology in neurodegeneration.

A major hallmark in Alzheimer's disease (AD) is the accumulation of aggregated extracellular β-amyloid (Aβ) peptide deposits[1]. However, the mechanisms by which these deposits trigger neuronal changes and contribute to cognitive deficits remain unclear. Amyloid plaques are known to cause synapse loss[2] and dendritic spine reduction in their vicinity[3], but a less understood and potentially critical feature is the formation of axonal spheroids around plaques. Hundreds of axons, but not dendrites, near individual plaques develop enlarged spheroid-like structures (traditionally termed dystrophic neurites)[4–10]. These plaque-associated axonal spheroids (PAASs) correlate well with AD severity[4,11], disrupt axonal electrical conduction[4,12,13], impair neuronal networks[4] and may contribute to cognitive decline. PAASs contain enlarged, enzyme-deficient endolysosomal vesicles[4,14–16] and autophagosomes[15,17]. Spheroid enlargement may result from the accumulation of these vesicles[4] and disruption of axonal cytoskeleton and transport[16,18–22]. Ultimately, the presence of axonal spheroids may

A full list of affiliations appears at the end of the paper. ✉e-mail: yifei.cai@yale.edu; jaime.grutzendler@yale.edu

further impair axonal trafficking, leading to downstream synaptic dysfunction and axonal degeneration[3,23–25]. Additionally, PAASs may contribute to the propagation of tau pathology through neuronal networks[26]. Thus, PAASs may represent a critical neuropathological hub, driving circuit disruption and proteinopathy and contributing to cognitive decline in AD[3,4,12,13,23,27].

Axonal spheroids can form as a result of a variety of insults and are observed across acute neural injuries and age-related neurodegenerative conditions. Although they share morphological and subcellular cytoskeletal and organelle features, including the accumulation of proteins such as amyloid precursor protein (APP) and cathepsins[14,22], mechanistic differences exist given the diversity of pathological processes involved. In neural injury models, spheroid formation involves cytoskeletal disruption, membrane tension changes[22,28] and phosphatidylserine exposure, leading to glial phagocytosis[22,29]. In contrast, in AD, PAASs persist for very long intervals without significant glial clearance[4,30–32].

Despite these observations, PAASs have not been a major focus of mechanistic investigations, and the cell biological processes underlying their formation remain poorly understood. In the present study, we developed a proteomics approach to investigate the molecular composition of PAASs, by employing proximity labeling to selectively isolate the subcellular proteome of PAASs in human postmortem and mouse brains. This analysis revealed protein turnover, cytoskeleton dynamics and lipid transport as key biological processes in PAASs. Additionally, we identified hundreds of previously unknown proteins and signaling pathways expressed in PAASs, some of which could play important roles in their formation.

To investigate the structural dynamics, functional consequences and reversibility of PAASs, we established a human induced pluripotent stem cell (iPSC)-derived AD model that recapitulates PAAS pathology. This model enabled longitudinal imaging and optical electrophysiology, revealing patterns of spheroid growth and action potential conduction disruption. To further examine the mechanisms driving spheroid growth, we focused on the mTOR signaling pathway, identified through PAAS proteomics and confirmed to be expressed within PAASs in vivo. Genetic and pharmacological inhibition of mTOR in iPSC neurons and in mice led to marked reduction in PAAS pathology. As mTOR is a master regulator of protein turnover, lipid metabolism and axonal cytoskeletal remodeling[33–35], these findings highlight the importance of these biological processes in PAAS formation.

Altogether, the integration of subcellular proteomics in postmortem human brain, human iPSC AD modeling and molecular manipulation of PAASs in human neurons and mice provides new insights into the complex cell biology and reversibility of axonal pathology in AD.

Results

Proximity labeling of axonal spheroids in AD human brains

Proximity labeling is a methodology used to biotinylate proteins within specific cellular or subcellular compartments using genetic expression of localized peroxidases or biotin ligases[36–40], enabling the selective protein biotinylation, isolation and identification of proteomes using liquid chromatography with tandem mass spectrometry (LC–MS/MS)[41,42]. Recently, this approach was adapted for fixed tissues by targeting subcellular compartments with horseradish peroxidase (HRP)-conjugated antibodies, enabling localized protein biotinylation[43–46]. Leveraging these advancements, we devised and refined an antibody-based proximity labeling approach to characterize the PAAS proteome in postmortem AD human brains and 5×FAD mice (Fig. 1, Extended Data Figs. 1 and 2, Supplementary Figs. 1 and 2 and Supplementary Movie).

Our approach was based on the observation that phospholipase D3 (PLD3), an endolysosomal protein, is highly abundant within PAASs (Fig. 1c and Extended Data Fig. 1e–g)[4,47–50], specifically expressed in neurons[4,47] and absent in glial cells[4]. Although low levels of PLD3 are found in neuronal cell bodies (Extended Data Fig. 1), quantitative immunofluorescence demonstrated that most PLD3 originates from PAASs (Extended Data Fig. 1g). Leveraging this finding, we used PLD3 as a protein bait for proximity labeling proteomics of PAASs. This involved sequential incubation of postmortem AD human or mouse brains with a primary antibody against PLD3 and an HRP-conjugated secondary antibody, followed by a peroxidation reaction with H_2O_2 and Biotin-XX-Tyramide (Fig. 1d). This process resulted in robust biotinylation of proteins within PAASs, confirmed by streptavidin labeling with minimal background outside axonal spheroids (Fig. 1e–h). To validate the spatial precision of proximity labeling, we employed stimulated emission depletion (STED) super-resolution imaging, which confirmed the high precision of proximity biotinylation of axonal spheroids (Extended Data Fig. 2). Additionally, to demonstrate subcellular specificity, we conducted parallel proximity labeling experiments using the neuronal nuclear and perinuclear cytoplasm marker NeuN as a protein bait (Extended Data Fig. 1c,d).

We also optimized the protein lysis method, significantly improving protein extraction efficiency compared to previous studies[43]. This protocol involved increased sodium dodecyl sulfate (SDS) concentration to 2% in basic Tris-HCl solution (pH 8.0), which enhanced protein extraction by effectively de-crosslinking proteins in fixed postmortem tissue (Supplementary Fig. 2a and Methods). Using this approach, we performed pulldown of biotinylated proteins and detected them via streptavidin–HRP western blotting. The analysis revealed a diverse array of proteins, including the baits PLD3 and NeuN as well as axonal spheroid proteins RAGC and cathepsin B (Fig. 1i and Supplementary Figs. 2b–d). Thus, the refined proximity labeling method provides a robust approach for isolating proteins enriched in axonal spheroids, enabling comprehensive proteomic profiling.

Proteomic analysis of plaque-associated axonal spheroids

To uncover the proteome of axonal spheroids, samples from individuals with AD and unaffected controls were processed for PLD3 proximity labeling protein biotinylation (Fig. 2a and Extended Data Fig. 3). Human frontal cortex postmortem samples were obtained from 39 individuals from the Yale Alzheimer's Research Center ($n = 8$ AD and $n = 2$ control) and the Banner Sun Health Research Institute ($n = 17$ AD and $n = 12$ control), with detailed clinical and neuropathological data (Supplementary Fig. 1). Individuals with AD exhibited high amyloid plaque load, whereas controls had minimal or no plaque burden. For proteomics, we selected six individuals with AD (three females and three males) with the highest amyloid plaque burden (Supplementary Fig. 1c) and eight unaffected controls (three females and five males). An additional 25 AD cases (13 females and 12 males) and seven controls (two females and five males) were used for immunofluorescence validation.

Proteomic analysis identified 2,360 proteins through a three-step process (Fig. 2b,c). First, non-specific protein binders to beads were removed by comparing PLD3-labeled samples to no-antibody controls, using cutoffs of $P < 0.05$, false discovery rate (FDR) < 0.1 and fold change (FC) > 1.5. To ensure data stringency, we compared normalized total precursor intensity (NTPI) and normalized total spectra count (NTSC) methods (Supplementary Fig. 3). This analysis identified 870 proteins (NTSC) and 965 proteins (NTPI) after applying these statistical cutoffs, with 849 proteins shared between the two methods, which were then used for downstream analysis. Second, we searched for glial cell–specific proteins and found only two, which were excluded from the dataset. Third, we aimed to exclude proteins specific to neuronal soma and neuropil, by comparing the proteomes of PLD3-labeled AD samples to unaffected controls, using $P < 0.05$ and FC > 1.5 or FC < 0.67. Given that the PLD3 labeling in controls originates from neuronal soma and neuropil (due to the absence of plaques), proteins with FC > 1.5 (98 proteins) represented those enriched in PAASs and/or broadly increased in AD. Proteins with FC < 0.67 (51 proteins) represented those specific to neuronal soma and neuropil and/or those decreased in AD. To increase stringency, proteins with FC < 0.67 were removed from the PAAS proteomic dataset (Fig. 2b).

https://doi.org/10.1038/s43587-025-00823-3

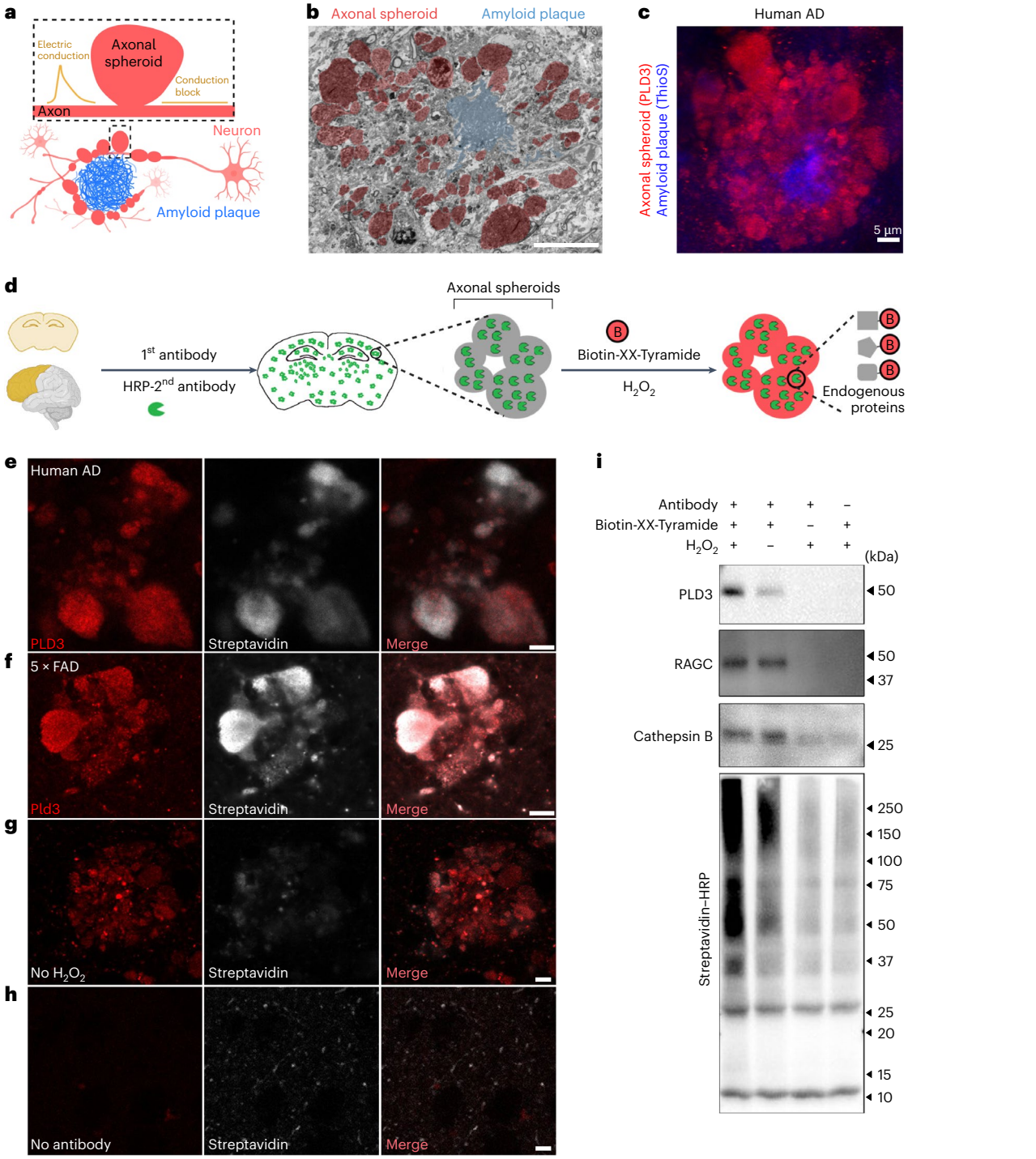

Fig. 1 | Proximity labeling of proteins within plaque-associated axonal spheroids. a, Schematic showing axons with spheroids (red) around an amyloid plaque (blue). Spheroids disrupt axonal electric conduction, causing delays and blockages[4]. **b**, FIB/SEM image of a 5×FAD mouse brain showing spheroids (red) around an amyloid plaque (blue). Scale bar, 20 µm. Related to Supplementary Movie. **c**, Immunofluorescence confocal deconvolved image demonstrating that PLD3 is highly enriched in axonal spheroids (red, PLD3) around amyloid plaques (blue, thioflavinS) in postmortem AD human brain. **d**, Schematic of the pipeline for proximity labeling PAAS proteomics in postmortem brains. AD human or mouse brain sections were incubated with a primary antibody against PLD3 and an HRP-conjugated secondary antibody, followed by a biotinylation reaction in the presence of Biotin-XX-Tyramide and H_2O_2. **e**–**h**, Proximity labeling biotinylation of proteins within PAASs: human AD brains (**e**) and 5×FAD mouse brains (**f**). **e**,**f**, Biotinylated proteins were visualized using streptavidin–Alexa Fluor 647. **g**,**h**, Control conditions include no-H_2O_2 (**g**) or no-antibody labeling (**h**), both of which showed markedly reduced biotinylation. Scale bar, 5 µm. **i**, Streptavidin–HRP western blot showing efficient streptavidin bead pulldown of biotinylated proteins, including PLD3 (protein bait) and known axonal spheroid proteins RAGC and cathepsin B. See also Extended Data Figs. 1 and 2 and Supplementary Figs. 1 and 2.

As a result, 821 proteins remained, representing the PAAS proteome in AD, all exhibiting an FC enrichment > 1.95 (Fig. 2b,c, Supplementary Figs. 4–6 and Supplementary Tables 1 and 2).

For comparative analysis, parallel experiments were conducted with 15-month-old 5×FAD mice (Extended Data Fig. 4). Using a similar proteomic strategy, we identified 856 PAAS proteins in mice (Fig. 2a–c,

https://doi.org/10.1038/s43587-025-00823-3

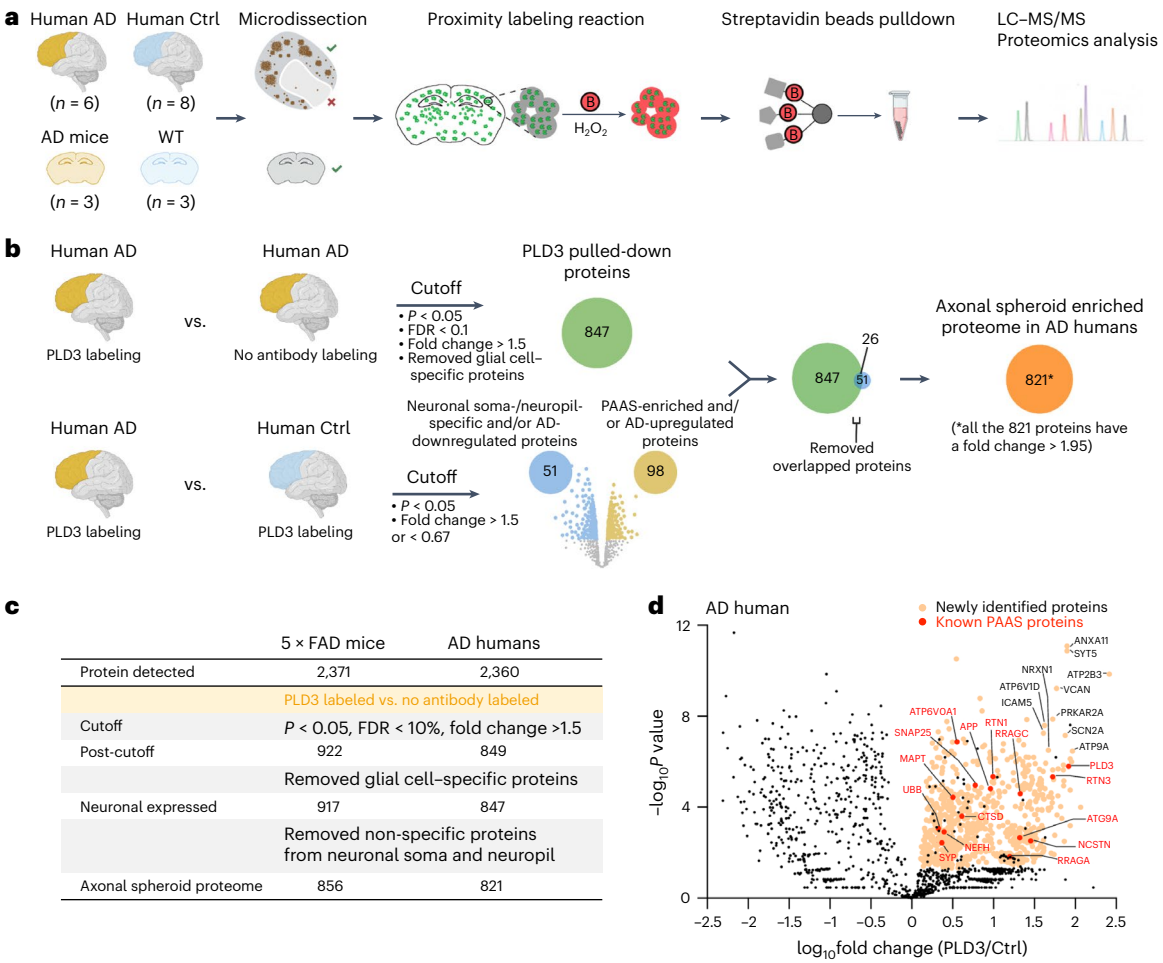

c

	5 × FAD mice	AD humans
Protein detected	2,371	2,360
	PLD3 labeled vs. no antibody labeled	
Cutoff	$P < 0.05$, FDR < 10%, fold change >1.5	
Post-cutoff	922	849
	Removed glial cell–specific proteins	
Neuronal expressed	917	847
	Removed non-specific proteins from neuronal soma and neuropil	
Axonal spheroid proteome	856	821

Fig. 2 | Proteomic analysis of plaque-associated axonal spheroids in humans with AD and 5×FAD mice. a, Schematic of the technical pipeline for PAAS proteomic analysis. Gray matter regions with high plaque load were microdissected from brain sections from human AD; gray matter was also dissected from unaffected controls under a fluorescence stereomicroscope. **b**, Statistical pipeline used to identify PAAS proteomes in humans (related to Fig. 2c and Extended Data Fig. 1e–g). The same pipeline was applied to uncover PAAS proteomes in 5×FAD mice. **c**, Table showing statistical cutoffs and summary of identified proteomic hits in humans with AD and 5×FAD mice. The human PAAS proteome includes 821 proteins (all with FC > 1.95), whereas the mouse PAAS proteome includes 856 proteins (all with FC > 1.66). **d**, Volcano plot showing proteins that passed statistical cutoffs (orange dots) in humans with AD. The top 10 proteomic hits, with the lowest *P* values and highest FCs, are labeled by their gene names in black. Selected known PAAS proteins are highlighted as red dots with red gene names. Black dots among yellow ones represent proteins filtered out by the statistical pipeline (Fig. 2b) (see Supplementary Table 1 for the full list of proteomic hits). **c**,**d**, Quantification was performed two-sided. See also Extended Data Figs. 3–7 and Supplementary Figs. 3–6. Ctrl, control.

Extended Data Fig. 4a and Supplementary Table 1). All 856 proteins exhibited FC > 1.66 (Supplementary Table 1), with 476 overlapping between humans with AD and 5×FAD mice (Extended Data Fig. 4b). Proteomic analyses in both humans and mice revealed hundreds of proteins previously unknown to be expressed in PAASs, alongside those already reported (Fig. 2d, Extended Data Fig. 4a, Supplementary Fig. 6 and Supplementary Table 2).

Various controls ensured specificity, including additional proteomics using Lamp1 as a bait in 5×FAD mice, which detected 510 overlapping hits with PLD3 but also identified numerous glial-derived proteins (Extended Data Fig. 5), consistent with Lamp1 expression in glial cells. To confirm the robustness of proteomic hits, anti-biotin bead pulldown of biotinylated peptides produced results consistent with streptavidin bead pulldown (Extended Data Fig. 6). To further examine subcellular specificity, we used NeuN, a neuronal nuclei and perinuclear cytoplasm marker[51], as a control bait. Unlike the PLD3-labeled PAAS proteome, the NeuN-labeled proteome showed distinct specificity to nuclei and neuronal soma (Extended Data Fig. 7 and Supplementary Table 1).

Uncovering key signaling pathways in axonal spheroids

To gain insights into the molecular mechanisms associated with axonal spheroid pathology, we conducted Gene Ontology (GO) annotation of biological process, molecular function and cellular component using the human PAAS proteomics dataset of 821 proteins, followed by pathway enrichment analysis. Results showed that proteomic hits were primarily associated with axons, synapses, cytoskeleton, lysosomes and proteasome complex (Fig. 3a and Supplementary Table 4). These findings reflect the axonal origin of PAASs and the accumulation of endolysosomal organelles, as shown by immunofluorescence and electron microscopy (Fig. 1b,c and Supplementary Movie)[4,14]. Many synapse-related proteins, such as the SNARE complex, are involved in both vesicle fusion and endolysosomal function. Because PAAS structures lack pre-synaptic and post-synaptic features (Supplementary Movie), SNARE complex proteins and other synapse-related signatures likely indicate vesicle fusion processes within the endolysosomal pathway.

We performed signaling pathway analysis using the human PAAS proteome and found that 10 of the top 17 central nervous system

(CNS)-related pathways involved three main modules, synapse/vesicle fusion, protein turnover and cytoskeleton (Fig. 3b), consistent with GO analysis findings (Fig. 3a). These included five pathways related to the cytoskeleton (for example, axonal guidance), three to synapse/vesicle fusion (for example, synaptogenesis) and two to protein turnover (for example, phagosome maturation) (Fig. 3b and Supplementary Table 5). Additional pathways included those related to synapse and vesicle fusion, such as clathrin-mediated endocytosis signaling and cytoskeleton growth and dynamics, such as actin cytoskeletal signaling and Rho family GTPase signaling (Fig. 3c). Pathways involved in protein turnover, including ubiquitination, autophagy and phagosome formation, were also identified. We also noted activation of the PI3K/AKT and mTOR pathways and inhibition of PTEN signaling (Fig. 3c), which have all been implicated in regulation of protein turnover and axonal growth[52]. Notably, subsets of proteomic hits from these pathways showed increased expression in humans with AD compared to controls (Fig. 3d).

To confirm the expression of proteomic hits in PAASs, we validated selected proteins from various pathways using high-resolution immunofluorescence confocal microscopy. These included proteins linked to synaptogenesis, vesicle fusion and calcium signaling (for example, SYT11 and CAMK2A) and cytoskeleton dynamics (for example, SPTBN1) (Fig. 3e, Supplementary Fig. 7 and Supplementary Table 2). A complete list of validated proteins is provided in Supplementary Fig. 6 and Supplementary Table 2. For immunofluorescence validation, we used SMI312 or PLD3 to visualize PAAS structures. SMI312, a neurofilament and pan-axonal marker, typically highlights axonal morphology but also accumulates in PAASs under AD conditions, reflecting cytoskeletal abnormalities. SMI312 is widely validated as a PAAS marker in pathological conditions[15,16] and is particularly useful for co-localization studies with other antibodies. However, SMI312 is expressed in only a subset of spheroids[14]. Similarly, newly validated proteins from our proteomic dataset exhibited heterogeneous expression levels. This variability in protein expression within spheroids suggests a potential mechanistic sequence of events occurring at different stages of spheroid formation and growth.

We also conducted parallel PAAS proteomics analysis in 5×FAD mice. Similar to the human PAAS proteome, GO terms related to axon, cytoskeleton, SNARE binding, lysosome and endosome transport were identified (Extended Data Fig. 4c). Additionally, signaling pathways associated with synapse/vesicle fusion, protein turnover and cytoskeleton dynamics were captured in the 5×FAD mouse PAAS proteome (Extended Data Fig. 4d,e).

Lipid transport signaling is markedly upregulated in axonal spheroids

To investigate aberrant signaling in PLD3-labeled AD brains compared to controls, we performed gene set enrichment analysis (GSEA) (Fig. 4a and Supplementary Table 6). GSEA revealed significant upregulation of lipid transport–related biological processes (Fig. 4a,b). Top-ranked proteins associated with these processes included ATP8A1, C3, APOE, ATG9A, ATP8A2, TMEM30A, HEXB and HDLBP (Fig. 4c), all of which were identified in the PAAS proteome and increased in AD (Fig. 4d, related to Fig. 2b and Supplementary Fig. 6). Conversely, GSEA showed downregulation of ribosome, translation and RNA metabolism in PLD3-labeled AD brains compared to controls (Fig. 4a). Because PLD3-labeled signals in unaffected brains are derived from neuronal soma and neuropil, the downregulated processes in unaffected controls likely correspond to protein functions specific to these subcellular compartments.

To validate the enrichment of top-ranked lipid-related proteomic hits in PAASs, including APOE, HDLBP, C3, HEXB and TMEM30A, we performed immunofluorescence confocal imaging (Fig. 4e,f and Extended Data Fig. 8a). Notably, APOE, the strongest genetic risk factor for AD and a lipid transporter[53], was among the top hits. We observed varying levels of expression of these proteins in axonal spheroids in AD human brains (Fig. 4e,f, Extended Data Fig. 8a and Supplementary Table 2). Complement C3 (C3), APOE and high-density lipid binding protein (HDLBP) exhibited the highest expression in axonal spheroids and aberrant axons around amyloid plaques, with much lower expression in axons away from plaques (Fig. 4e, Extended Data Fig. 8a and Supplementary Table 2). These proteins were also detected in cell bodies and in neuropil and plaque regions, aligning with their known distribution patterns (Extended Data Fig. 8a and Supplementary Table 2). Notably, HDLBP exhibited a distinct pattern of segregation within a subset of thickened axonal segments where the pan-axonal marker SMI312 was absent (Fig. 4g), suggesting that lipid metabolism dysregulation may precede spheroid enlargement. Regarding HEXB, which is primarily expressed in microglia in mice[54], we found it expressed in PAASs and neuronal cell bodies in human brains (Extended Data Fig. 8b), consistent with human single-cell transcriptional profiles[55].

mTOR signaling in axonal spheroids

The PAAS proteomics analysis highlighted the activation of the PI3K/AKT/mTOR axis within axonal spheroids (Fig. 3c and Extended Data Fig. 4e). This pathway is a master regulator of mRNA translation, metabolism and protein turnover[35,52]. Consistent with these roles, our proteomic analysis identified protein turnover, lipid metabolism and axonal cytoskeleton dynamics as prominent signatures (Figs. 3 and 4 and Extended Data Fig. 4d,e)[33–35]. Key proteins in the PI3K/AKT/mTOR axis were selected for validation. Among these, mTOR, RAGA (RRAGA), RAGC (RRAGC), LAMTOR1 and AKT1 were detected in the PAAS proteomes of humans and/or mice, whereas PIK3R4, RHEB and RAPTOR were not (Supplementary Fig. 6 and Supplementary Tables 1 and 2). Immunofluorescence staining confirmed the presence of all selected proteins in axonal spheroids in both postmortem AD human brains and 5×FAD mice (Fig. 5a). Proteins detected in the proteomes showed moderate to high immunofluorescence signals in PAASs, whereas those that were not detected exhibited moderate to low expression (Fig. 5a and Supplementary Table 2). Notably, phosphorylated-mTOR-S2448, a marker of mTOR activation, was expressed in axonal spheroids in AD human brains but not in unaffected controls (Fig. 5b–d). This finding

Fig. 3 | Pathway analyses reveal proteins involved in protein turnover and cytoskeleton as key components of PAASs. a, Pathway enrichment analysis of the PAAS proteome in AD human brains. The Enrichment Map represents a network of pathways, with edges connecting pathways that share many genes. Node color reflects the FDR of each pathway. Theme labels were curated based on the main pathways of each subnetwork. Subnetworks with a minimum of four pathways connected by edges are shown. **b**, IPA pathway analysis of the PAAS proteome in humans with AD. Top-ranking CNS-related signaling pathways are shown. The signaling pathways are summarized as four modules. The alluvium plot shows color-coded modules connecting to the differentially expressed genes (DEGs), and the DEGs connect to the pathways that they are involved in. **c**, IPA pathways related to the three modules (synapse/vesicle fusion, protein turnover and cytoskeleton) with $P < 0.01$ are listed. Heatmaps indicate either the $-\log_{10}$ (P value) or the z-score of each signaling pathway (pathways with a z-score in red are predicted to be activated, whereas blue ones are predicted to be inhibited). **d**, Bar chart shows representative proteomic hits from the signaling pathways in **c**. Newly identified proteins are shown in red; known PAAS proteins are shown in black. $n = 6$ human AD brains and $n = 8$ unaffected human control brains were analyzed. Error bars indicate s.e.m. **c**,**d**, Quantification was performed two-sided. **e**, Representative immunofluorescence confocal images of newly identified proteins (red) expressed in spheroids (gray) in AD postmortem brains. Scale bar, 5 µm. Zoom-out images are shown in Supplementary Fig. 7. Quantification was performed in $n = 10$ AD human brains. Protein expression quantifications can be found in Supplementary Table 2. See also Extended Data Fig. 4 and Supplementary Fig. 7. Ctrl, control.

https://doi.org/10.1038/s43587-025-00823-3

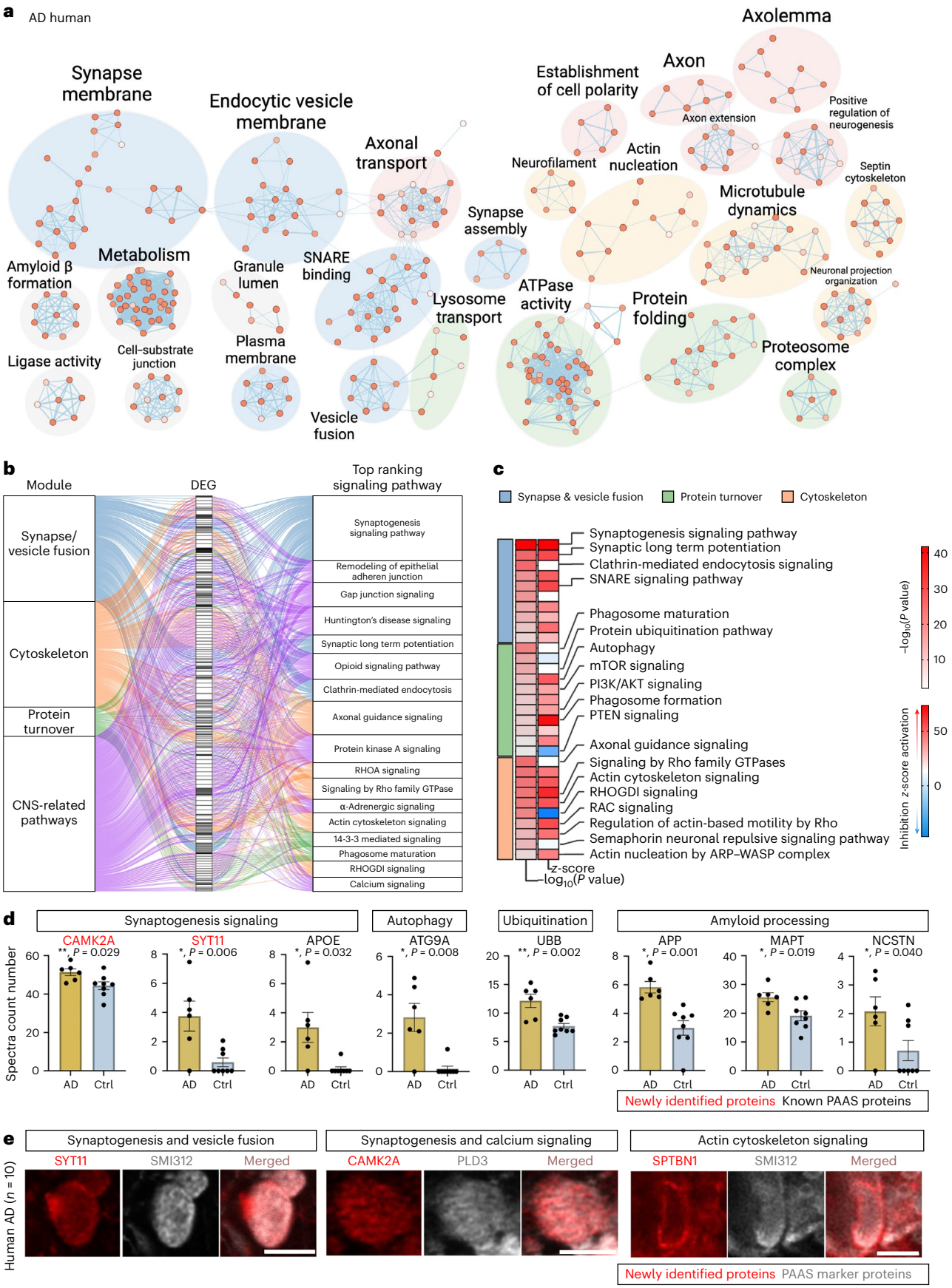

https://doi.org/10.1038/s43587-025-00823-3

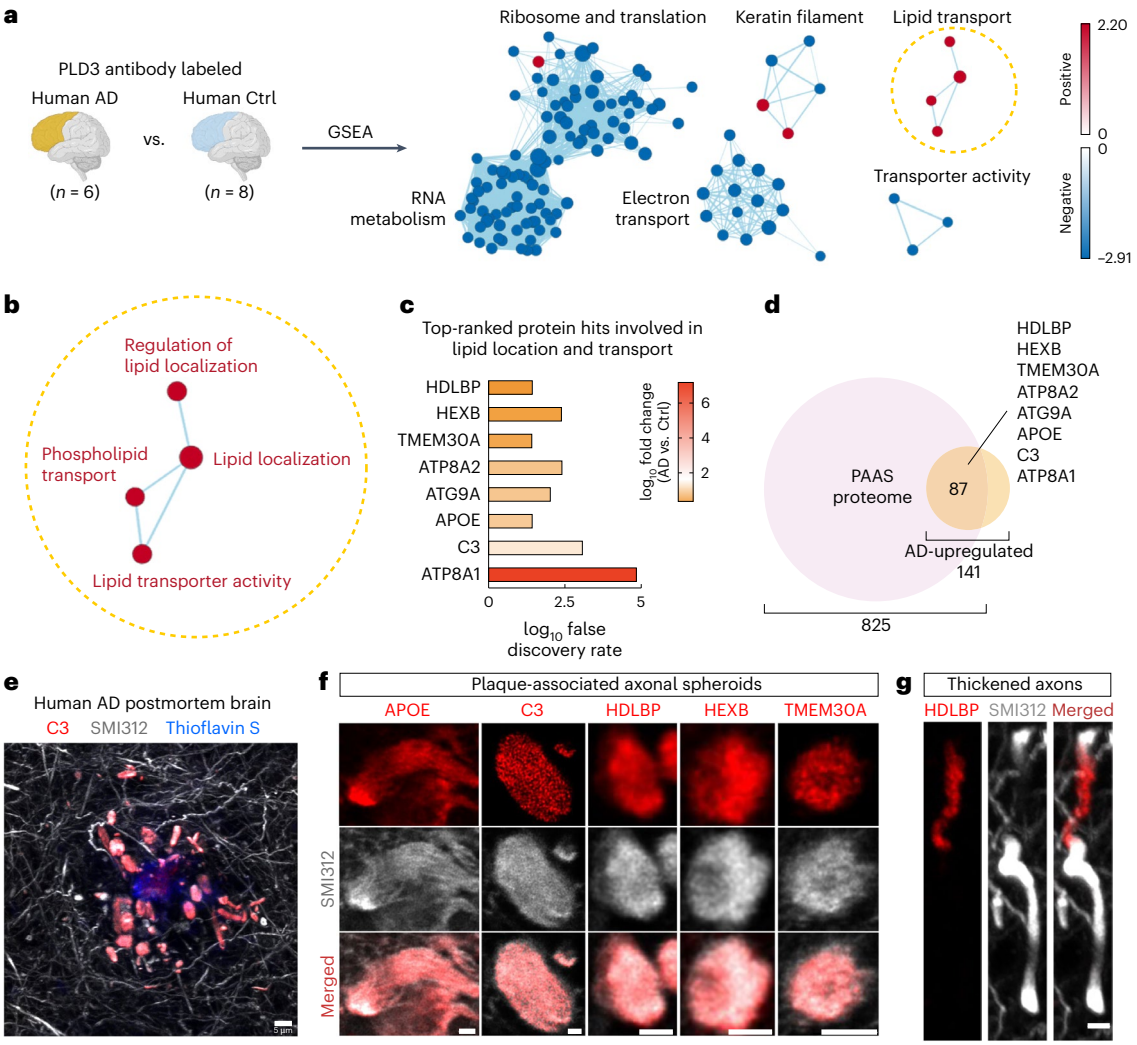

Fig. 4 | Proteins involved in lipid transport are upregulated in PAASs. a, GSEA was performed to compare PLD3-labeled proteins between humans with AD and unaffected controls. Pathway enrichment analysis was performed to cluster GSEA nodes. Each node represents a biological process or cellular component. The name of each cluster was curated based on the main GSEA biological processes and cellular components within each cluster. See also Supplementary Table 6. **b**, Detailed information on the lipid transport cluster. The biological process or cellular component of each node is listed. **c**, The eight top-ranked proteomic hits involved in the lipid transport cluster. The bar chart shows the FC and FDR of these hits by comparing PLD3-labeled humans with AD versus unaffected controls. **d**, Venn diagram showing that the eight top-ranked lipid transport–related proteins are shared between the human PAAS proteomes (821 proteins) and the AD upregulated proteins (98 proteins). A total of 75 proteins are shared between these two datasets. **e**,**f**, Representative zoomed-out (**e**) and zoomed-in (**f**) immunofluorescence confocal images of the top-ranked lipid-related proteomic hits in AD human brain, including C3, APOE, HDLBP, HEXB and TMEM30A. Scale bar, 5 µm. Zoomed-out images of all the proteins are shown in Extended Data Fig. 8. Quantification was performed in $n = 3$ AD human brains. Protein expression quantifications can be found in Supplementary Table 2. **g**, Representative immunofluorescence confocal images showing the anti-co-localized distribution of HDLBP (red) and the pan-axonal marker SMI312 (gray) within thickened axons in the AD human postmortem brain ($n = 3$). Scale bar, 5 µm. Ctrl, control.

suggests that phosphorylated-mTOR-S2448 may serve as a potential marker for disease progression. Overall, these results underscore the activation and involvement of the PI3K/AKT/mTOR axis in axonal spheroids in AD.

Human iPSC modeling replicates axonal spheroid pathology

To establish a comprehensive strategy for investigating selected proteomic hits and their roles in spheroid formation, we developed a long-term human iPSC-derived neuron and astrocyte co-culture AD model[56] (Fig. 6a,b and Extended Data Fig. 9a–d). A similar approach was recently shown to replicate axonal spheroid formation with exogenous aggregated Aβ1–42 (ref. 57). We simplified the induction protocol using the *NGN2*-induced glutamatergic neuron method[56], making it more accessible for most laboratories. Increasing the overall neuronal density enhanced the similarity to axonal spheroid halos observed around amyloid plaques in the human brain. Our optimized model generated thioflavin S–positive amyloid deposits surrounded by abundant axonal spheroids (Fig. 6b, Extended Data Figs. 9e,f and 10a–c and Supplementary Fig. 8a). These spheroids accumulated lysosomes and autophagosomes (Fig. 6b,c) and expressed phosphorylated Tau S235, S396 and S404 (Extended Data Fig. 9g), closely resembling human axonal spheroids[4,58].

This culture system enabled longitudinal structural and functional imaging, providing insights into the dynamics and consequences of spheroid pathology. Using reporter adeno-associated viruses (AAVs) to label neurons and lysosomes, we tracked spheroid formation after Aβ1–42 administration. Confocal microscopy of individual axons revealed gradual spheroid formation and lysosomal accumulation starting on day 1, with spheroids increasing in size over a 7-day observation period (Fig. 6c).

https://doi.org/10.1038/s43587-025-00823-3

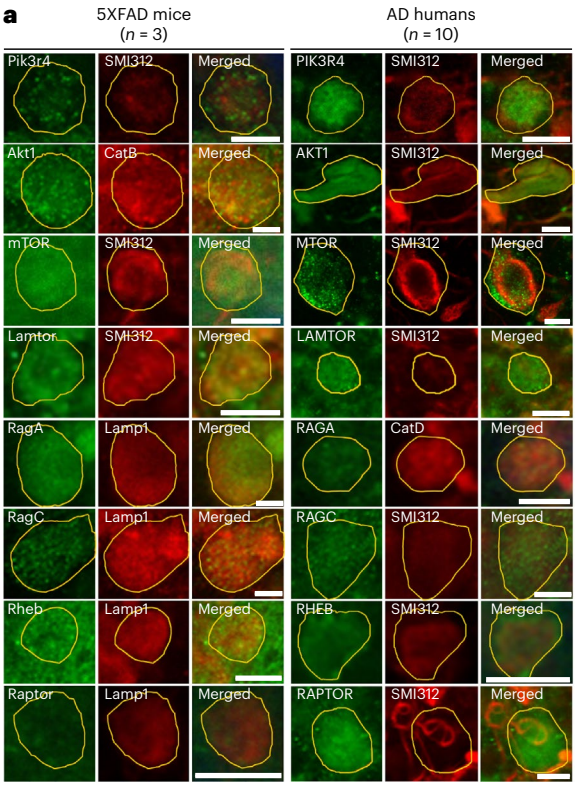

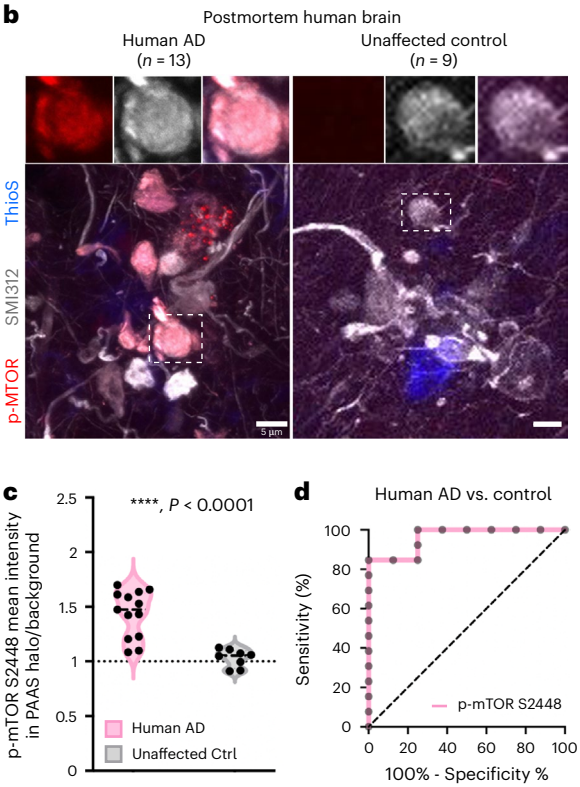

Fig. 5 | mTOR signaling is expressed in axonal spheroids and is associated with Alzheimer's pathology. a, Immunofluorescence confocal imaging validation of selected proteomic hits and the related proteins in the PI3K/AKT/mTOR axis reveals that signaling molecules of this axis are expressed in PAASs in both humans with AD and 5×FAD mice. PAASs were labeled using traditional markers, including neurofilament SMI312, cathepsin B (CatB), cathepsin D (CatD) or Lamp1. PAASs are outlined in yellow. Scale bar, 5 µm. Protein expression quantification results can be found in Supplementary Table 2. **b**, Phosphorylated-mTOR-S2448 (red) is highly enriched within PAASs (gray, SMI312) around amyloid plaques (blue, thioflavinS) in advanced AD. Scale bar, 5 µm. **c**, Quantification of the mean fluorescence intensity levels of p-mTOR-S2448 within axonal spheroid halos normalized to background fluorescence, comparing humans with AD ($n = 13$ brains) and unaffected controls ($n = 8$ brains). Mann–Whitney test, two-tailed, $^{****}P < 0.0001$. Black dashed line indicates the median. **d**, Receiver operating characteristic (ROC) curve demonstrates that the p-mTOR-S2448 level in PAASs significantly distinguishes AD brains from unaffected controls. Area under the ROC curve = 0.962, standard error = 0.038, 95% confidence interval: 0.888–1.000, $P = 0.0005$. Quantification was performed two-sided. Ctrl, control; ThioS, thioflavin S.

We also investigated the functional repercussions of spheroid formation in this human iPSC-derived model. Using calcium imaging with the reporter GCaMP8f, we measured Ca^{2+} rise times in axonal segments on both sides of axonal spheroids after electrical stimulation. Axonal segments with spheroids showed a significantly reduced calcium rise slope compared to those without spheroids (Fig. 6d–f), consistent with impaired action potential conduction across spheroids, as seen in our earlier in vivo findings in 5×FAD mice[4]. Additionally, axon segments with spheroids exhibited prolonged calcium decay times compared to normal processes and somata, indicating disrupted calcium homeostasis within spheroids (Fig. 6g,h).

mTOR inhibition reduces spheroid pathology in human neurons

We investigated the role of PI3K/AKT/mTOR signaling in axonal spheroid development and enlargement using the human iPSC-derived AD model. Consistent with findings in postmortem human brains (Fig. 5), we detected expression of proteins associated with the PI3K/AKT/mTOR pathway localized within axonal spheroids (Fig. 6i and Supplementary Fig. 8).

To evaluate the impact of mTOR inhibition, we treated 3-month-old iPSC-derived neuron and astrocyte co-cultures with Torin1, an inhibitor of both mTORC1 and mTORC2 (refs. 59,60). A 7-day treatment with Torin1 significantly suppressed mTOR signaling, as evidenced by reduced phosphorylation of downstream effectors p-p70 S6K (Thr 389) and p-4E BP1 (Thr 37/46), without affecting total protein levels (Fig. 6j and Supplementary Fig. 9). To assess the effects of Torin1 on spheroid formation and reversal, cultures were treated either before or after Aβ exposure. Pre-treatment with Torin1 before Aβ substantially decreased both the number and size of spheroids (Fig. 6k–p). Post-treatment with Torin1 after Aβ exposure reduced the number of spheroids but did not affect their size (Fig. 6q,r and Extended Data Fig. 10a–c). Notably, these effects were not due to axonal loss (Fig. 6n and Extended Data Fig. 10d), changes in neuronal density or amyloid plaque size (Fig. 6o,p and Extended Data Figs. 9h and 10e). These results indicate that mTOR signaling is critical for amyloid-induced spheroid formation and suggest that targeting mTOR could be a promising approach for both preventing and reversing spheroid pathology.

Amelioration of spheroid pathology in 5×FAD mice

To investigate the role of mTOR signaling in axonal spheroid pathology in vivo, we employed a viral-mediated Cre/lox-based approach to induce *Mtor* knockout in 5×FAD mice (Fig. 7a–c and Supplementary Fig. 1a–d). Using heterozygous *Mtor*-floxed 5×FAD mice[61] and AAV9-hsyn-cre-2a-tdTomato, we achieved partial loss of mTOR in infected neurons. Sparse neuronal infection enabled clear visualization of individual spheroids (Fig. 7d,e), showing a significant reduction in spheroid size after heterozygous *Mtor* knockout (Fig. 7f,g).

To evaluate the overall impact on spheroid size and number, we measured the axonal spheroid halo size around individual amyloid plaques. We infected *Mtor*-floxed 5×FAD mice with AAV-PHP.

eB-hSyn-Cre-GFP virus to achieve dense neuronal infection, inducing widespread *Mtor* heterozygous knockout in neurons (Fig. 7h and Supplementary Fig. 10b,d,e). This intervention significantly reduced the axonal spheroid halo size around plaques without affecting amyloid plaque size (Fig. 7i,j and Supplementary Fig. 10e–h). Notably, despite the role of mTOR in cell growth and maturation[35,59], heterozygous *Mtor* knockout did not change the size of neuronal cell bodies (Fig. 7k and Supplementary Fig. 10f). These findings in vivo, consistent with the results from human iPSC-derived neurons, underscore the potential of targeting PI3K/AKT/mTOR signaling for mitigating axonal spheroid pathology in AD.

Signaling pathways involved in lysosome biogenesis and autophagy likely contribute to the accumulation of aberrant endolysosomes in spheroids. Additionally, local mRNA translation, which has been shown to modulate axonal outgrowth, may play a role in spheroid formation[62,63]. Considering the known effects of mTOR on lysosome biogenesis, autophagy and local mRNA translation[35,52], we investigated related downstream molecules. Using AAV-PHPeB-hSyn-Cre, we achieved extensive neuronal infection in mTOR heterozygous floxed 5×FAD mice, enabling widespread mTOR heterozygous knockout in neurons (Fig. 7a–c,h). Immunofluorescence confocal imaging assessed expression levels of TFEB (lysosomal biogenesis transcription factor), p-p70S6K (regulator of local protein synthesis) and LC3B (autophagy marker) in neuronal somata. Automated quantitative analysis compared mTOR heterozygous knockout mice to controls (Fig. 7l–o). Results showed increased TFEB and LC3B expression (Fig. 7l,m), indicating enhanced lysosomal biogenesis and autophagy. Additionally, we observed decreased p-p70S6K (Fig. 7n,o), which may be associated with reduced local mRNA translation[52].

We investigated whether local mRNA translation occurs in axonal spheroids. Using RNAscope in 5×FAD mice, we probed for mRNA species in axonal spheroids with a poly(A) tail probe and compared it to a scrambled control probe (Fig. 7p and Supplementary Fig. 11a). The poly(A) probe showed signal localization within axonal spheroids, whereas the control probe did not, confirming the presence of mRNA in these structures (Fig. 7q and Supplementary Fig. 11b–d). To examine local mRNA translation, we performed an in vivo puromycylation assay in 5×FAD mice (Fig. 7r and Supplementary Fig. 12a). Nascent proteins labeled by puromycin were detected in axonal spheroids, and treatment with the protein translation inhibitor anisomycin reduced the degree of labeling (Fig. 7s and Supplementary Fig. 12a–c), indicating that local mRNA translation occurs within spheroids. To test whether mTOR can regulate nascent protein production in spheroids, we applied both pharmacological and genetic approaches. Treatment with Torin1 to inhibit mTOR in 5×FAD mice did not alter the puromycin signal. Additionally, we used mTOR-floxed mice and a PHPeB-hSyn-Cre virus to genetically knock out mTOR in neurons. Neither the heterozygous nor homozygous mTOR deletion significantly affected the puromycin signal (Fig. 7a–c and Supplementary Figs. 10a–d and 12d–f). These results indicate that, under our experimental conditions (Supplementary Fig. 12d–f), mTOR does not appear to control local protein translation within axonal spheroids. These experiments indicate that the reduction in axonal spheroid size and number observed after mTOR inhibition is likely due to its enhancement of lysosomal biogenesis and autophagy rather than modulation of local protein translation in spheroids.

Discussion

Plaque-associated axonal spheroids, also known as dystrophic neurites, have been recognized as a hallmark of AD for over a century[10,11,14,64,65], but their molecular composition and the mechanisms driving their progression remain largely unexplored due to methodological limitations. In the present study, we implemented a comprehensive approach to investigate the molecular and cellular mechanisms of PAAS formation. We developed a subcellular proximity labeling proteomics method for postmortem human and mouse brains[43], enabling detailed analysis of the protein composition and signaling pathways operating within PAASs (Fig. 8, Supplementary Fig. 6 and Supplementary Table 2). Bioinformatics analysis and high-resolution confocal imaging identified hundreds of proteins and pathways newly associated with PAASs, including lipid transport, protein turnover and cytoskeletal dynamics, with the PI3K/AKT/mTOR pathway emerging as a key regulator of these biological processes in PAASs. To explore the functional implications of these findings, we implemented an optimized human iPSC-derived AD model[57] that replicates amyloid plaque and PAAS formation. Pharmacological and genetic inhibition of mTOR signaling in this model and in AD-like mice significantly reduced PAAS pathology. Altogether, our study reveals the molecular architecture and functional impact of PAASs in human neurons and implicates the PI3K/AKT/mTOR axis as a key signaling pathway in PAAS formation and growth. It also suggests new therapeutic targets for mitigating axonal pathology independently of amyloid removal.

Proximity labeling proteomics with subcellular resolution overcame the cellular and subcellular specificity limitations of conventional tissue proteomics, including those using micro-dissected amyloid plaques[66–68]. Using an antibody-based biotinylation method[43,44], we tagged proteins in axonal spheroids without requiring exogenous peroxidase or biotin ligase overexpression[36,37,41], enabling comparative proteomics from widely available postmortem tissues. PLD3 was chosen as the antibody bait due to its high enrichment in PAASs of both humans and mice[47,48] and its neuron-predominant expression[4,47], minimizing contamination from other cell types. Comparison of PLD3-labeled

Fig. 6 | A human iPSC-derived AD model demonstrates that mTOR signaling inhibition reduces PAAS pathology. a, Workflow of the human iPSC-derived AD model. **b**, Image showing axonal spheroids (SMI312, gray) around amyloid deposits (thioflavinS, blue) and expressing ATG9A (red). **c**, Time-lapse imaging shows a spheroid forming (arrowhead) from a neurite (AAV9-hSyn-mCherry labeled) near Aβ deposits (gray) and enlarging over time. Lysosomes (AAV2-CMV-LAMP1-GFP labeled) accumulate within spheroids. **d**–**h**, Neuronal GCaMP8f imaging in the human iPSC AD model. **d**, Images of CAMKII-GCaMP8f-labeled neuronal processes with (upper) or without (lower) axonal spheroids and representative traces of calcium dynamics. *y* axis indicates $\Delta F/F$, and dotted black lines indicate the calcium rise slope. Quantification of calcium rise time (**e**) and calcium rise speed (**f**). Each dot represents a neuronal process from three independent experiments (two-tailed Mann–Whitney test). **g**, Images showing that calcium decay time is slower in spheroids (pink asterisk) than in neuronal processes (blue asterisks). **h**, Quantification of calcium decay time in neuronal soma (blue), processes with (light pink) or without (light blue) spheroids and spheroids (pink). Each dot represents a neuronal process from three independent experiments (one-way ANOVA). **i**, mTOR signaling in iPSC-derived axonal spheroids (SMI312). **j**, Western blot showing that Torin1 treatment reduces mTOR downstream effectors phosphorylated 4E-BP1 and phosphorylated p70 S6K, whereas their total protein levels remain unchanged. **k**–**r**, Torin1 reduced axonal spheroids (SMI312) around Aβ deposits (thioflavin S). **l**–**p**, Pre-Aβ administration Torin1 treatment quantification: **l**, axon with spheroid percentage ($n = 3$ in each group). Paired *t*-test two-tailed, $P = 0.005$. **m**, spheroid size (paired *t*-test two-tailed, $P = 0.013$, $n = 4$ per group). Dots represent experiments (20–30 ROIs). **n**, Axon number around plaques in each ROI (Torin1 $n = 56$; vehicle $n = 55$; unpaired *t*-test two-tailed, $P = 0.880$). **o**, Soma size. Dots represent neuronal somata (Torin1 $n = 298$, vehicle $n = 316$. Unpaired *t*-test two-tailed, $P = 0.927$; related to Extended Data Fig. 8i). **p**, Plaque size. Dots represent amyloid plaques (Torin1 $n = 201$, vehicle $n = 253$. Unpaired *t*-test two-tailed, $P = 0.419$). **q**,**r**, Post-Aβ administration Torin1 treatment (related to Extended Data Fig. 10). Spheroid number normalized to axon density (**q**) and spheroid size (**r**) (Mann–Whitney test, two-tailed, $n = 4$ per group). Scale bar, 5 µm, except scale bar, 10 µm in **g**. **e**,**f**,**h**,**l**–**r**, Data presented as mean values ± s.e.m. See also Extended Data Figs. 9 and 10 and Supplementary Fig. 8. NS, not significant; ThioS, thioflavin S.

https://doi.org/10.1038/s43587-025-00823-3

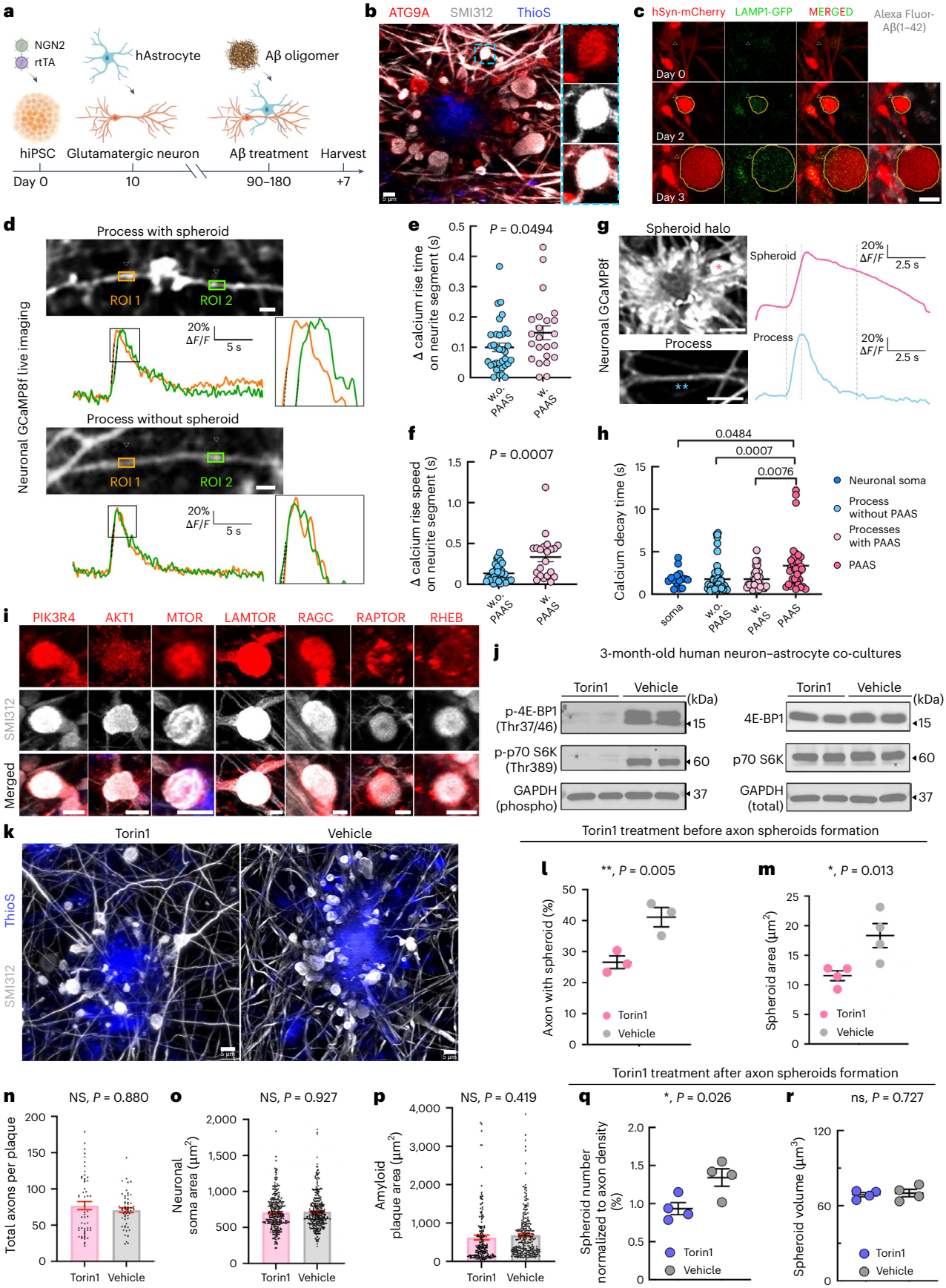

and Lamp1-labeled proteomes in 5×FAD mice confirmed that the PLD3-labeled proteome is highly specific for neuronal and axonal structures (Extended Data Fig. 5).

Using this proteomic strategy, we identified numerous proteins enriched in PAASs, including previously unknown ones, alongside those already associated with these structures (Fig. 8, Supplementary Fig. 6 and Supplementary Tables 1 and 2). Proteomic analysis in humans with AD revealed three key biological processes likely involved in PAAS formation and growth (Figs. 3 and 4). (1) Proteolysis Dysfunction: This was indicated by the accumulation of proteins related to endocytosis, phagosome, proteosome, ubiquitin-mediated proteolysis and lysosome acidification (Figs. 3, 5 and 8 and Supplementary Table 2). Previous studies demonstrated that accumulation of enlarged protease-deficient lysosomes and autophagosomes within PAASs[14] mediates spheroid growth[4], highlighting the critical role of impaired lysosomal function. Some of the identified proteins are also expressed in synapses, raising the possibility that PAASs may originate from pre-synaptic structures, although electron microscopy did not reveal pre-synaptic or post-synaptic features in PAASs (Supplementary Movie). (2) Cytoskeletal Dysregulation: Activated signaling pathways, such as actin cytoskeletal signaling, RAC signaling and actin nucleation by the ARP–WASP complex, were enriched within PAASs, whereas pathways such as RHOGDI signaling, which regulates Rho family GTPase, were inhibited (Fig. 3c and Extended Data Fig. 4e)[69,70]. These findings suggest that ongoing cytoskeletal reorganization and plasticity within PAASs play a key role their formation and enlargement. Moreover, these cytoskeletal changes may disrupt retrograde and anterograde axonal cargo transport, leading to accumulation of endolysosomal vesicles[18,28,71] and further spheroid expansion. (3) Lipid Transport and Metabolism: Lipid-related signaling was highly activated in PAASs (Fig. 4a–d), with proteins involved in lipid transport and metabolisms, such as APOE, HDLBP and C3, prominently expressed in PAASs and aberrant axons (Fig. 4b–g and Extended Data Fig. 8a). Among these, APOE, the most significant AD risk gene, acts as a lipid carrier[53]. TMEM30A, ATP8A1 and ATP8A2 (Fig. 4c,e), which form the P4–ATPase complex, regulate asymmetric membrane lipid distribution, membrane stability and vesicle-mediated protein transport[72]. These proteins are likely related to the massive accumulation of endolysosomal vesicles within PAASs, requiring active lipid transport, synthesis and metabolism and aligning with findings that lipids participate in axonal lysosome delivery and spheroid formation[21]. Interestingly, complement C3, crucial for complement system activation[73] and lipid metabolism[74,75], exhibited the highest expression in axonal spheroids and aberrant axons (Fig. 4e,f and Extended Data Fig. 8a). This aligns with prior research linking complement proteins to dystrophic neurites around compact amyloid plaques[76–78] and suggests a potential connection between complement pathway activation and spheroid formation. On the basis of our previous work showing that microglia rarely engulf spheroids and that spheroids persist for long periods[4,31,32], we propose that C3 is playing a role independent of traditional neuroimmune interactions, warranting further investigation.

The PI3K/AKT/mTOR was identified as a key activated signaling pathway within PAASs (Fig. 3c and Extended Data Fig. 4e), with its activation in human postmortem brains strongly correlating with AD severity (Fig. 5b,c). The PI3K/AKT/mTOR pathway is known to inhibit autophagy, endosome and autophagosome maturation[79], lysosomal biogenesis and proteasome assembly[52] while promoting axonal outgrowth[62,63,80] and lipid synthesis[52,81]. Interestingly, lipids such as phosphatidic acid and cholesterol can activate the mTORC1 complex[82,83], suggesting that lipids within PAASs may mediate mTOR activation. This, in turn, could modulate PAAS formation by regulating the three key biological processes that we identified in PAASs: lipid transport, protein turnover and cytoskeletal dynamics (Figs. 3 and 4).

Our findings demonstrate that pharmacological inhibition of mTOR signaling in the human iPSC-derived AD model significantly reduced PAAS pathology (Fig. 6). Separate in vivo experiments with neuron-specific mTOR heterozygous knockout in 5×FAD mice excluded glial contributions, confirming a neuronal cell-autonomous effect of mTOR on PAASs (Fig. 7). Investigation of downstream mechanisms revealed that mTOR knockdown enhanced autophagy, likely acting both at the whole cell level and locally within axonal spheroids, consistent with the extensive accumulation of endolysosmal vesicles in these structures. Additionally, the presence of mRNA and nascent proteins in axonal spheroids suggested potential for local translation at these sites. However, although mTOR signaling is known to modulate local translation in neurons[62,63,84], our study did not detect changes in local translation levels after mTOR knockout or pharmacological inhibition (Supplementary Fig. 12d–f).

In addition to PI3K/AKT/mTOR, we observed activation of other signaling pathways within PAASs, including calcium signaling and amyloid processing (Figs. 3c and 8). Proteins involved in calcium signaling, such as CAMK2 and calmodulin, were identified in PAASs (Fig. 3e, Supplementary Fig. 7 and Supplementary Table 2), suggesting a role for local calcium signaling dysregulation in PAAS pathogenesis. This is supported by our longitudinal calcium imaging in human neurons, which showed that axonal spheroids disrupt calcium rise and decay times after electrical stimulation, indicating impaired action potential conduction and calcium homeostasis within PAASs. Additionally, recent studies have shown that abnormal local calcium efflux from

Fig. 7 | mTOR signaling inhibition reduces axonal spheroid pathology in vivo. **a**, Schematic of neuronal-specific conditional knockout of *Mtor* in heterozygous floxed mice. **b**,**c**, Images showing neuronal-specific Cre-mediated *Mtor* knockout: homozygous (**b**) and heterozygous (**c**), using AAV9-hSyn-Cre-2A-tdTomato or AAV PHPeB-hSyn-Cre-EGFP in *Mtor*-floxed mice, respectively. **b**, mTOR expression (gray) was absent in Cre-expressing neurons compared to adjacent NeuN-labeled neurons without Cre expression. **c**, mTOR expression was reduced in Cre-expressing neurons compared to neurons without Cre expression. Scale bar, 5 µm. **d**, Experimental design to study mTOR knockout effects on individual spheroids. **e**, Images showing AAV9-hSyn-Cre-2A-tdTomato sparsely labeling individual spheroids (red) within a spheroid halo (Lamp1, gray). **f**, Quantification of spheroid size. Dots represent animals (mTOR-flox-AD $n = 5$, 5×FAD $n = 4$. Unpaired *t*-test, two-tailed, $P = 0.027$). **g**, Using the same data in **f**, comparison of spheroid size distribution and visualization using a quantile–quantile (Q–Q) plot. Dashed lines indicate spheroid area at 10 µm^2. 5×FAD mice have significantly more large spheroids (area > 10 µm^2) compared to mTOR-KO-AD (two-sample test for equality of proportions with continuity correction, two-tailed, $P = 0.0004$). **h**, Experimental design to assess the effect of *Mtor* knockout on spheroid halo size. **i**, Quantification of spheroid halo size. Dots represent animals ($n = 3$; unpaired *t*-test, two-tailed, $P = 0.041$). **j**, Quantified by axonal spheroid halos (knockout group $n = 66$ and control group $n = 109$. Unpaired *t*-test, two-tailed, $P < 0.0001$). **k**, Quantification of neuronal soma size. Dots represent animals ($n = 3$). Unpaired *t*-test, two-tailed, $P = 0.90$. **l**–**o**, Investigation of mTOR heterozygous knockout downstream signaling effectors. Immunofluorescence intensity of TFEB (**l**), LC3B (**m**), P-p70S6K Thr389 (**n**) and p70S6K (**o**). Littermates and sex were paired in **l**–**o**, paired *t*-test. Dots represent animals ($n = 3$ in each group). **p**, RNAscope in 5×FAD mice cortices showing mRNA species (poly(A) probe, magenta) present in spheroids (NHS ester-labeled, yellow, and DAPI negative). NHS ester (yellow) labels the spheroid halo and amyloid plaques. Nuclei are labeled with DAPI (blue). Scale bar, 5 µm. **q**, Quantification of poly(A) probe fluorescence intensity versus negative control probe within spheroids in cortices of 5×FAD mice ($n = 3$). Unpaired *t*-test, parametric, two-tailed, $P = 0.001$. **r**, Representative images showing puromycin labeling. Scale bar, 5 µm. **s**, Quantification of puromycin fluorescence intensity in axonal spheroids of 5×FAD mice ($n = 3$). Unpaired *t*-test, parametric, two-tailed, $P = 0.028$. **j**,**q**,**s**, Data are presented as mean values ± s.e.m. See also Supplementary Figs. 10–12. mo, months; NS, not significant.

https://doi.org/10.1038/s43587-025-00823-3

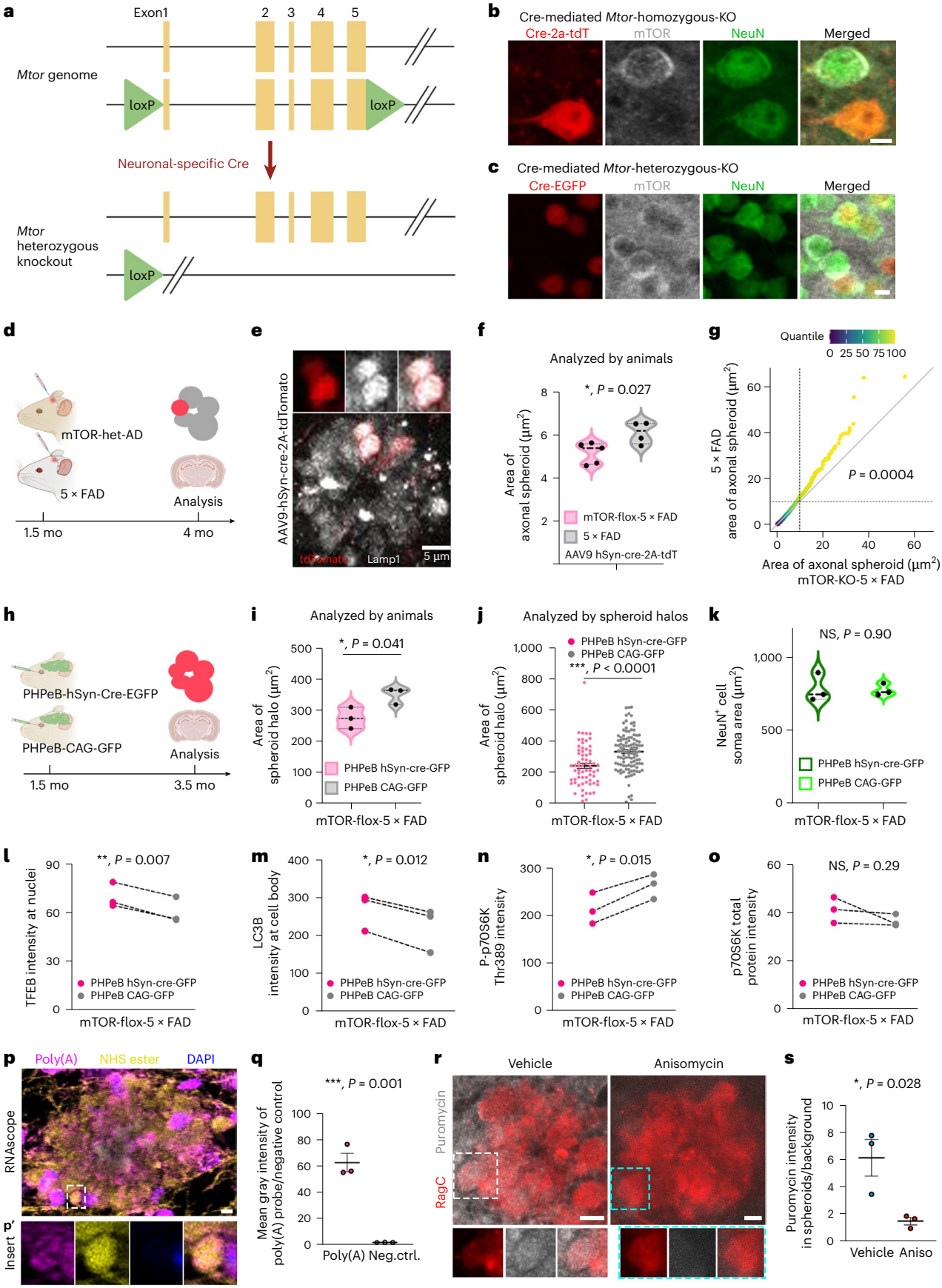

https://doi.org/10.1038/s43587-025-00823-3

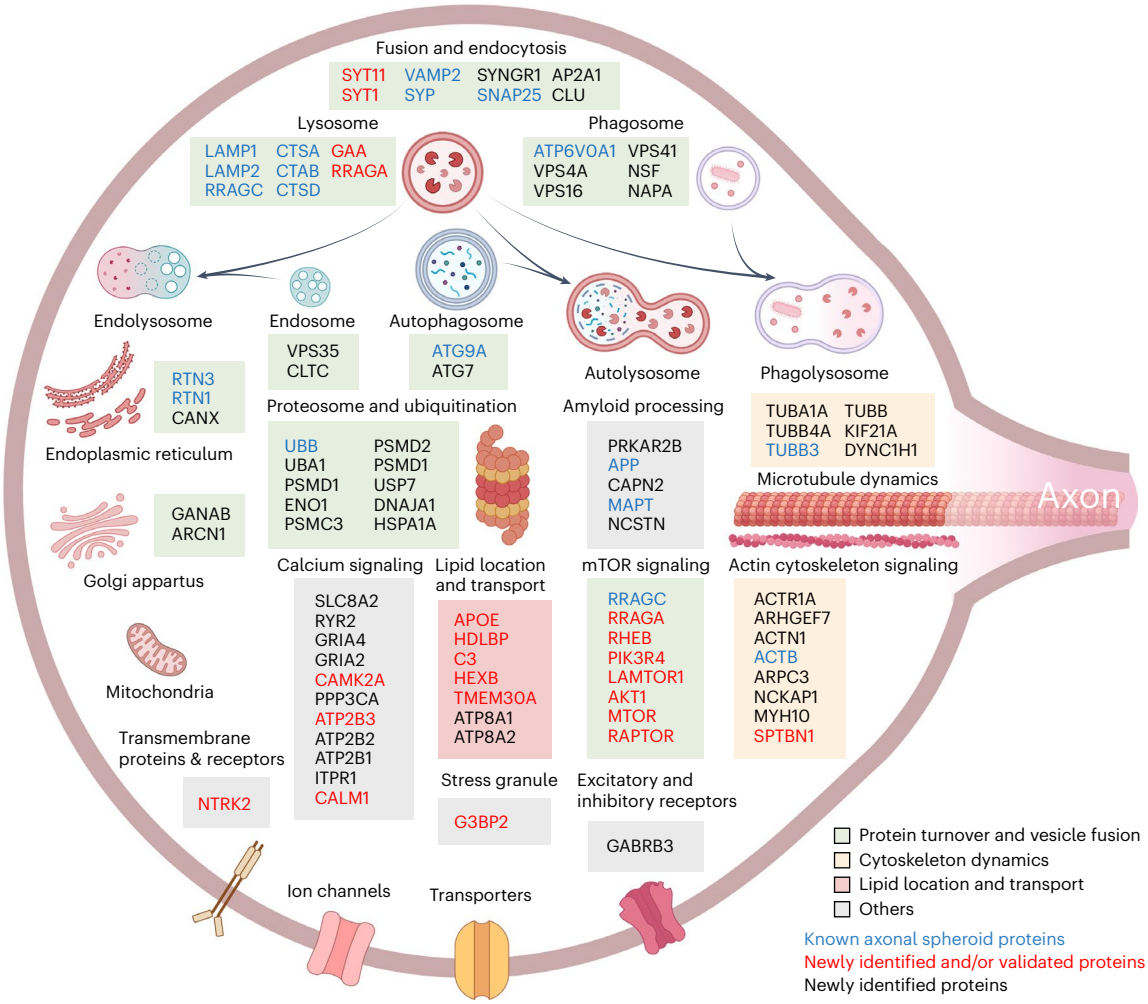

Fig. 8 | Schematic of the molecular architecture of plaque-associated axonal spheroids. Proximity labeling proteomics reveals proteins associated with various subcellular organelles, the ubiquitin–proteosome system and cytoskeleton. These proteins and their signaling pathways are linked to biological functions, including protein turnover and vesicle fusion (green box); cytoskeletal dynamics (yellow box); lipid localization and transport (red box); and others (gray box). Highlighted here are selected newly identified and validated proteins, alongside those previously known to be enriched in PAASs, such as lysosomal proteins LAMP1 (ref. 4), cathepsin B and D[14], RAGC[14] and PLD3 (refs. 47,48); autophagosome protein ATG9A[112]; endoplasmic reticulum proteins RTN3 (ref. 112) and RTN1 (ref. 113); cytoskeletal neurofilament protein[114]; microtubule protein TUBB3 (ref. 20); synaptic proteins synaptophysin[5] and VAMP2 (ref. 14); as well as APP[31], Tau (MAPT)[26] and ubiquitin[71,112] (Supplementary Table 2).

de-acidified late endosomes and amphisomes can disrupt axonal transport of these vesicles[85], highlighting the complex interplay between calcium signaling and other pathways during PAAS development.

The human iPSC-derived AD model effectively replicated PAAS pathology, characterized by abundant spheroid formation around thioflavin S–positive amyloid plaques and significant accumulation of endolysosomal vesicles, cytoskeletal elements and phosphorylated tau within PAASs. The administration of exogenous Aβ in this model (Fig. 6a–d) supports the theory that spheroids form in response to extracellular amyloid deposition rather than acting as the source of these deposits[18,86]. Longitudinal imaging of individual axons in human neurons revealed rapid spheroid formation and lysosome accumulation within days of Aβ administration, with axons exhibiting active growth during spheroid formation rather than a dying-back pattern (Fig. 6c), consistent with previous in vivo mouse studies[4]. Despite widespread exposure to oligomeric Aβ in this model, axonal spheroids were predominantly observed next to compact thioflavin S–positive plaques (Fig. 6b and Extended Data Figs. 9e,f and 10b,c). This is consistent with human observations, where diffuse amyloid deposits (thioflavin S negative) rarely induce PAASs, whereas thioflavin S–positive deposits are closely associated with PAAS pathology[31]. These findings suggest that specific β amyloid conformations are critical for triggering PAAS formation.

This study has several potential limitations. First, although STED super-resolution imaging showed that the radius of antibody-based proximity labeling in brain tissue was less than 50 nm, some proteins distal to PLD3 may not have been captured in the PAAS proteome. However, the high enrichment of PLD3 in axonal spheroids likely increased biotinylation efficiency, resulting in our ability to capture most proteins previously described in PAASs, including endolysosomal-related proteins as well as cytoskeletal proteins (for example, SPTBN1) and cell surface receptors (for example, NTRK2) (Figs. 2d and 8, Extended Data Fig. 4a, Supplementary Fig. 6 and Supplementary Table 2). Second, although PLD3 is abundant in spheroids in both AD human and mouse brains, some labeling does occur at neuronal cell bodies and neuropil (~27% of PLD3 signal) (Extended Data Fig. 1e–g). We addressed this by excluding proteins potentially originating from neuronal cell bodies (Fig. 2b and Methods), but the presence of some neuronal cell body–specific proteins in the PAAS proteome cannot be entirely ruled out. For instance, a protein upregulated in AD but expressed solely in the neuronal soma could theoretically appear as a false positive, although we have not found such cases so far. Third, the low number

of plaques and axonal spheroids in early-stage AD limited our ability to compare levels of the various PAAS proteins across disease stages due to insufficient protein yield. Future studies could leverage multiplexed high-resolution quantitative imaging[87] for comparisons at different disease stages. Finally, the human iPSC-derived AD model in our study recapitulates spheroid formation around amyloid plaques but does so through a rapid process that may not fully mimic in vivo mechanisms. Refining these models to allow for more chronic amyloid buildup and incorporating co-cultures with other cell types, such as microglia, could better replicate the in vivo plaque microenvironment.

Altogether, the proteomics resources and methodologies developed in this study enable the investigation of axonal pathology in human postmortem brains, iPSC-derived human neurons and in vivo mouse models. Although this study focused on amyloid plaque-associated axonal spheroids, similar structures are observed in other neurodegenerative disorders[21,88–90]. Therefore, the multidisciplinary strategies, and the datasets generated, mapping the molecular architecture of axonal spheroids will facilitate studies into the diverse mechanisms underlying axonal spheroid pathology in AD and other neurodegenerative conditions, providing a foundation for hypothesis generation and therapeutic target testing.

Methods

Human postmortem brain tissue

Snap-frozen postmortem human brain specimens of frontal cortices from patients with AD and age-matched controls were obtained from the Yale Alzheimer's Disease Research Center and the Banner Sun Health Research Institute. Detailed demographic and clinical information can be found in Supplementary Fig. 1. For proximity labeling proteomics, six AD cases with intermediate to high AD level[64] and eight age-matched unaffected controls were used. To reduce inter-sample variability and maximize signal to noise by avoiding brains with low-density amyloid deposition, we carefully inspected approximately 40 individual postmortem brains using microscopy and selected for proteomic analysis six AD brains with the highest density of amyloid plaques and axonal spheroids within the frontal cortex. The gray matter regions with high plaque load were microdissected out from AD brain sections under visual guidance using a fluorescence stereomicroscope (Leica). Similarly, the gray matter regions were dissected from unaffected control brain sections. For immunofluorescence proteomic validations, 25 severe AD and 14 unaffected control cases were used (Supplementary Fig. 1).

Human iPSC line and human primary astrocytes

Two fully characterized, de-identified control human iPSC lines, NSB3182-3 (female) and NSB2607 (male), were used in all experiments[91]. *NGN2*-induced glutamatergic neurons[56] were generated and co-cultured with human primary astrocytes (Thermo Fisher Scientific, N7805200, or ScienCell, 1800) for all experiments[57].

Mice

All animal procedures were approved by the Institutional Animal Care and Use Committee at Yale University. Animals were housed at the Yale University Animal Facility, with a 12-hour light/dark cycle, temperature at 65–75 °F and with 40–60% humidity. Wild-type (WT) (C57BL/6J) mice, 5×FAD (Tg6799) mice[92] and mTOR-flox (The Jackson Laboratory (JAX), 011009) mice[61] were obtained from JAX. 5×FAD and WT mice, used for proximity labeling proteomics, were euthanized at 15 months of age, followed by transcardial perfusion. Three male mice per genotype (WT and 5×FAD) were used. Animals used for immunofluorescence proteomic validation were euthanized at 2–3 months or 12–15 months of age, with three biological replicates per experiment. mTOR-flox mice were cross-bred with 5×FAD mice to create an mTOR-flox 5×FAD line. For AAV-mediated mTOR heterozygous knockout experiments, mTOR-flox 5×FAD mice were injected with AAVs at 6 weeks of age. Five biological replicates (combining male and female mice) in each group were used for the AAV9-hSyn-cre-2a-tdT experiment, and three male mice in each group were used for the AAV-PHPeB experiment.

Antibodies and reagents

The full list of primary antibodies for newly validated and known PAAS proteins can be found in Supplementary Table 2, including catalog number, RRID, dilution factors and brief staining instructions. In brief, anti-PLD3 antibody, anti-SMI312 and anti-cathepsin D were used to label PAASs in both mice and humans. Anti-Lamp1 and anti-cathepsin B antibodies were used to label PAASs in mice. For proteomic hits validation, anti-GAA, anti-GBA, anti-TPP1, anti-ATP6V0A1, anti-SYT11, anti-G3BP1, anti-G3BP2, anti-ITM2B, anti-SPTBN1, anti-SV2A, anti-ATP2B3, anti-CAMK2A, anti-calmodulin, anti-SYT1, anti-CACNA2D1, anti-CACNA1B, anti-NTRK2, anti-mTOR, anti-p-mTOR S2448, anti-PIK3R4, anti-AKT1, anti-LAMTOR, anti-RAGA, anti-RAGC, anti-RHEB, anti-RAPTOR, anti-HDLBP, anti-APOE, anti-C3, anti-HEXB and anti-TMEM30A were used for validating newly identified PAAS proteins. Anti-RAGC, anti-ATG9A, anti-ubiquitin, anti-RTN3, anti-PKC, anti-synaptophysin, anti-SNAP25, anti-VAMP2 and anti-beta tubulin III were used for immunostaining of known PAAS proteins. To reveal GFP and tdTomato protein expression, anti-GFP (1:500, RRID: AB_10000240) and anti-RFP (1:200, RRID: AB_2209751) were used, respectively. For staining neuronal and glial markers in iPSC-derived human neurons, anti-neurofilament H (1:1,000, RRID: AB_2149761), anti-NeuN (1:1,000, RRID: AB_10711040), anti-NeuN (1:200, RRID: AB_2532109), anti-Synapsin1/2 (1:500, RRID: AB_2622240), anti-PSD95 (1:200, RRID: AB_10807979), anti-S100b (1:500, RRID: AB_2814881) and anti-IBA1 (1:100, RRID: AB_2891289) were used. To stain Aβ deposits, anti-6e10 (1:200, RRID: AB_2565328) was used. To stain phosphorylated Tau, anti-phospho-Tau S235 (1:1,000; Thermo Fisher Scientific), anti-phospho-Tau S396 (1:200) and anti-phospho-Tau S404 (1:200) were used (see RRIDs in Supplementary Table 2). Dendritic marker MAP2 (1:200, RRID: AB_776174) was used. To detect mTOR signaling substrates such as phosphor-4E-BP1 and p70S6K, an mTOR substrate antibody sampler kit (Cell Signaling Technology (CST), 9862) and anti-4E-BP1 antibody (CST, 9452) were used. For puromycylation, anti-puromycin 647 (1:1,000, RRID: AB_2736876) was used. Thioflavin S (Sigma-Aldrich, T1892, 2% w/v stock solution, 1:10,000 staining) was used to label amyloid plaques. Alexa Fluor dye-conjugated secondary antibodies were used (1:600; Thermo Fisher Scientific).

Tissue fixation

We compared the impact of different tissue fixation approaches on the proximity labeling efficacy and protein extraction efficiency. For human brain samples, snap-frozen postmortem human brains coupled with fresh fixation in 4% paraformaldehyde (PFA) at 4 °C for approximately 24 hours worked the best. For mice, freshly perfused mouse brains and fixed in 4% PFA at 4 °C for approximately 24 hours performed the best in both proximity labeling efficacy and protein extraction efficiency. We found that long-term fixation and storage with the formalin-fixed paraffin-embedded (FFPE) method markedly reduced both proximity labeling and protein extraction efficiencies.

Proximity labeling in brain tissue

Proximity labeling in human and mouse tissue was performed based on ref. 43 with optimizations. Detailed procedures are described below. Axonal spheroids were proximity labeled by using anti-PLD3 or anti-Lamp1 antibodies in mice and humans. Neuronal soma were proximity labeled using anti-NeuN antibody. In brief, frozen postmortem human brain specimens were fixed by submerging into ice-cold 4% PFA and put onto a shaker at 4 °C for approximately 24 hours. For mice, after transcardial perfusion, brains were fixed in 4% PFA at 4 °C for approximately 24 hours while shaking. Human and mouse brains were vibratome sectioned at 50-µm thickness. Ten sections

(approximately 1 cm × 0.8 cm each) for human or mouse brain were used in each reaction per biological replicate. Human sections contained mostly gray matter. Six to eight human biological replicates were used in each group, and three biological replicates were used in each mouse group. Sections were permeabilized by PBS with 0.5% Triton X-100 for 7 minutes, followed by rinsing with PBST (0.1% Tween 20 in PBS). To quench the endogenous peroxidase activity, sections were incubated in 0.1% H_2O_2 for 10 minutes, followed by rinsing with PBST twice. Primary antibody diluted in blocking buffer (0.1% Tween 20 with 1% BSA in PBS) was incubated overnight at 4 °C on a shaker, followed by PBST washes for three times at 20 minutes per wash. Secondary antibodies conjugated with HRP were incubated in blocking buffer for 1 hour at room temperature, followed by PBST washes for three times at approximately 40 minutes per wash. Proximity labeling was performed by using Biotin-XX-Tyramide dissolved in 50 mM Tris-HCl buffer (pH 7.4) with H_2O_2 for 5 minutes, according to the user's manual (Thermo Fisher Scientific, B40921). Specifically, every 1 ml of reaction solution was made of 10 µl of 1× Biotin-XX-Tyramide and 10 µl of 1× H_2O_2 in 50 mM Tris-HCl buffer. Biotinylation reactions were terminated by rinsing sections with freshly made 500 mM sodium ascorbate for three times, followed by PBST washes for three times.

Enrichment of biotinylated proteins using streptavidin beads

We performed proximity labeling proteomics on fixed brain specimens, which may reduce the protein extraction yield compared to other proximity labeling methods using fresh tissue. Thus, we optimized the protein extraction protocol and largely increased the protein extraction yield compared to previously published methods (Supplementary Fig. 2a)[43]. Specifically, brain sections from proximity labeling experiments were lysed and de-crosslinked in 100 mM Tris-HCl buffer (pH 8.0) with 2% SDS and protease inhibitor (Roche) at 95 °C for 45 minutes with constant shaking. For every 10 brain sections, 500 µl of lysis buffer was used. Protein lysate was sonicated using Sonic Dismembrator Model 500 (Thermo Fisher Scientific) for three times, 3 seconds per time at 4 °C. Protein lysate was centrifuged at 12,000 relative centrifugal force (rcf) for 5 minutes. Then, 450 µl of protein lysate supernatant was collected from each sample, incubated with 550 µl of PBST containing 200 µl of pre-washed streptavidin magnetic beads (Thermo Fisher Scientific, 88817), protease inhibitor and phosphatase inhibitor, to meet a final 1-ml volume. Samples were then incubated on a 360° rotator at 4 °C overnight. The rest of protein lysates were used for protein concentration measurement by BCA (Thermo Fisher Scientific). After incubation, beads were sequentially washed once with PBST, twice with PBST with 1 M NaCl and twice with PBS. Biotinylated proteins were eluted in elution buffer (20 µl of 20 mM dithiothreitol (DTT) and 2 mM biotin in 1× NuPAGE LDS lysis buffer (Thermo Fisher Scientific) with protease inhibitor and phosphatase inhibitor) at 95 °C for 5 minutes. Supernatant was collected and centrifuged at 12,000 rcf for 1 minute, followed by running into a 4–20% Tris-glycine gel (Invitrogen) at constant 150 V until all the proteins had run into the gel (approximately 10 minutes). Gel was rinsed once in ultrapure water (AmericanBio) and incubated in approximately 50 ml of Coomassie blue R-250 staining solution (Bio-Rad) for 1-hour incubation. Gel was de-stained with Coomassie blue R-250 destaining solution (Bio-Rad) for 2 hours with three times buffer changes. Gel was rinsed with ultrapure water for three times. Gel containing protein samples was visualized, cut with clean blades and kept at −20 °C.

Enrichment of biotinylated peptides using anti-biotin antibody

The labeled tissue was lysed using 100 mM Tris-HCl buffer (pH 8.0) with 2% SDS and protease inhibitor (Roche). The lysates were sonicated and then centrifuged at 16,500*g* for 10 minutes at 4 °C. The proteins were precipitated using acetone, and the pellet was dissolved in 8 M urea and 50 mM ammonium bicarbonate (ABC) and then sonicated for 30 seconds to re-solubilize the proteins. A Bradford assay was performed to determine protein concentration, and 2 mg of protein was used to process further. Proteins were reduced with 5 mM DTT for 45 minutes at room temperature and subsequently carbamidomethylated with 10 mM iodoacetamide for 30 minutes at room temperature in the dark. Before digestion, the urea concentration was reduced to 2 M with 50 mM ABC and digested with trypsin at an enzyme:substrate ratio of 1:50 overnight at 37 °C. After digestion, samples were acidified with 10% formic acid and de-salted using Nest Group C18 macro-spin columns (HMMS18V) as per the manufacturer's instructions. Biotinylated peptides were enriched using anti-biotin antibody-based immunoprecipitation. The peptides were dissolved in IAP buffer containing 50 mM MOPS, 10 mM HNa_2PO_4 and 50 mM NaCl at pH 7.5. Anti-biotin beads (ImmuneChem Pharmaceuticals) were washed twice in IAP buffer before the samples were added to the beads for incubation on a rotator for 2 hours at 4 °C. The beads were washed twice with IAP buffer and twice with water (high-performance liquid chromatography (HPLC) grade). The biotinylated peptides were eluted from the beads using 80% acetonitrile (ACN) and 0.15% trifluoroacetic acid (TFA) with vortexing, followed by a 10-minute incubation at room temperature. The elution was repeated twice, and the supernatants were collected and vacuum dried.

Western blotting

For western blotting, 4–20% Tris-glycine gels (Invitrogen) were used for protein electrophoresis following the manufacturer's protocol. Proteins were transferred to nitrocellulose membranes (Bio-Rad) at constant 350 mA for approximately 50 minutes. After blocking with 5% BSA in TBST (Tris-buffered saline with 0.1% Tween 20) for 1 hour, membranes were incubated with primary antibodies (anti-PLD3 1:250; anti-CatB 1:1,000; anti-RAGC 1:1,000; anti-NeuN 1:1,000; anti-GAPDH 1:1,000) diluted in 5% BSA in TBST on a shaker at 4 °C overnight, followed by three times of 15-minute washes with TBST. Membranes were then incubated with HRP-conjugated secondary antibodies diluted in 5% BSA in TBST for 1 hour at room temperature, followed by three times of 15-minute washes with TBST. To blot biotinylated proteins on the same membrane, stripping buffer (Thermo Fisher Scientific, 46430) was used to cover the whole membrane and incubated at room temperature with shaking for 10–12 minutes, followed by rinsing with PBST for three times. HRP-conjugated streptavidin (1:1,000) was diluted in blocking buffer for 1–2 hours at room temperature or 4 °C overnight. Clarity Western ECL blotting substrate (Bio-Rad) and ChemiDoc MP Imaging System (Bio-Rad) were used for chemiluminescence development and detection.

In-gel digestion

Gel slices were cut into small pieces and washed with 600 µl of water on a tilt table for 10 minutes, followed by 20-minute wash with 600 µl of 50% ACN/100 mM NH_4HCO_3 (ABC). The samples were reduced by the addition of 100 µl of 4.5 mM DTT in 100 mM ABC with incubation at 37 °C for 20 minutes. The DTT solution was removed, and the samples were cooled to room temperature. The samples were alkylated by the addition of 100 µl of 10 mM iodoacetamide (IAN) in 100 mM ABC with incubation at room temperature in the dark for 20 minutes. The IAN solution was removed, and the gels were washed for 20 minutes with 600 µl of 50% ACN/100 mM ABC and then washed for 20 minutes with 600 µl of 50% ACN/25 mM ABC. The gels were briefly dried by SpeedVac and then resuspended in 100 µl of 25 mM ABC containing 500 ng of digestion-grade trypsin (Promega, V5111) and incubated at 37 °C for 16 hours. The supernatants containing the tryptic peptides were transferred to new Eppendorf tubes. Residual peptides in the gel bands were extracted with 250 µl of 80% ACN/0.1% TFA for 15 minutes and then combined with the original digests and dried in a SpeedVac. Peptides were dissolved in 24 µl of MS loading buffer (2% ACN, 0.2% TFA), with 5 µl injected for LC–MS/MS analysis.

LC–MS/MS data collection

LC–MS/MS analysis was performed on a Thermo Fisher Scientific Q Exactive Plus equipped with a Waters nanoAcquity UPLC system using a binary solvent system (A: 100% water, 0.1% formic acid; B: 100% ACN, 0.1% formic acid). Trapping was performed at 5 µl min^{-1}, 99.5% buffer A for 3 minutes using an ACQUITY UPLC M-Class Symmetry C18 Trap Column (100 Å, 5 µm, 180 µm × 20 mm, 2G, V/M; Waters, 186007496). Peptides were separated at 37 °C using an ACQUITY UPLC M-Class Peptide BEH C18 Column (130 Å, 1.7 µm, 75 µm × 250 mm; Waters, 186007484) and eluted at 300 nl min^{-1} with the following gradient: 3% buffer B at initial conditions; 5% B at 2 min; 25% B at 140 min; 40% B at 165 min; 90% B at 170 min; 90% B at 180 min; return to initial conditions at 182 minutes. MS scans were acquired in profile mode over the 300–1,700 *m/z* range using one microscan, 70,000 resolution, AGC target of 3×10^6 and a maximum injection time of 45 ms. Data-dependent MS/MS scans were acquired in centroid mode on the top 20 precursors per MS scan using one microscan, 17,500 resolution, AGC target of 1×10^5, maximum injection time of 100 ms and an isolation window of 1.7 *m/z*. Precursors were fragmented by HCD activation with a collision energy of 28%. MS/MS scans were collected on species with an intensity threshold of 1×10^4, charge states 2–6 and peptide match preferred. Dynamic exclusion was set to 30 seconds.

Peptide identification

Data were analyzed using Proteome Discoverer software version 2.2 (Thermo Fisher Scientific). Data searching was performed using the Mascot algorithm (version 2.6.1) (Matrix Science) against the SwissProt database with taxonomy restricted to human (20,368 sequences) or mouse (17,034 sequences) as well as a streptavidin sequence. The search parameters included tryptic digestion with up to two missed cleavages, 10-ppm precursor mass tolerance and 0.02-Da fragment mass tolerance and variable (dynamic) modifications of methionine oxidation and carbamidomethyl cysteine. Normal and decoy database searches were run, with the confidence level set to 95% ($P < 0.05$). Scaffold version 5.1.2 (Proteome Software) was used to validate MS/MS-based peptide and protein identifications. Peptide identifications were accepted if they could be established at greater than 95.0% probability by the Scaffold Local FDR algorithm. Protein identifications were accepted if they could be established at greater than 99.0% probability and contained at least two identified peptides (one uniquely assignable to the protein). Proteins that contained similar peptides and could not be differentiated based on MS/MS analysis alone were grouped to satisfy the principles of parsimony. Proteins sharing significant peptide evidence were grouped into clusters. Label-free quantification was performed with Scaffold software. Spectral intensity values were used for protein quantification between groups.

To search for biotinylation sites in the anti-biotin antibody pull-down samples, the variable modifications of Biotin-XX-Tyramide were configured to account for marker ions resulting from fragmentation of biotinylated peptides. These marker ions have the following *m/z* values and elemental composition losses from the fully modified amino acid: dehydrobiotin (*m/z* 227.08), Biotin-X ion (*m/z* 340.25), Biotin-XX ion (*m/z* 453.25), immonium of tyrosine-Bxxp with loss of ammonia (*m/z* 706.38) and immonium of tyrosine-Bxxp (*m/z* 723.38).

Proteomic data analysis

Before the data analysis, missing values were removed. For example, if a protein A had 0 spectra count detected in all the samples, including tests and controls, then protein A was removed from the list. NTSC and NTPI are two common methods for proteomic quantification. For PLD3-labeled PAAS proteomes in humans, we compared NTSC and NTPI methods and used the shared proteomic hits for downstream analysis. For PLD3-labeled PAAS proteomes in mice, Lamp1-labeled proteomes in mice and NeuN-labeled neuronal nuclei and perinuclear cytoplasm proteomes in mice, we used NTSC for quantification. To obtain the PAAS proteome, differentially expressed proteins were analyzed by comparing proteomic hits obtained from PLD3-labeled samples versus those from control samples using no antibody. This allowed the filtering of endogenously biotinylated proteins and non-specific binders to streptavidin beads. To obtain the optimal cutoff values for the statistical analysis, we tested different degrees of stringency for FDR (0.1, 0.05 and 0.01) and FC (1 and 1.5). An optimum cutoff $P < 0.05$, FDR < 0.1 and FC > 1.5 was used for these datasets, as it captures the maximum numbers of known PAAS proteins while excluding the maximum numbers of potential contaminants. Post-cutoff proteomic lists were scrutinized for possible glial contaminations by cross-validations using single-cell RNA sequencing (scRNA-seq) transcriptomics in mice[55] and humans[93] and Tissue Atlas in the Human Protein Atlas[94]. When a gene had a fragments per kilobase of transcript per million mapped reads (FPKM) < 10 in neurons and an FPKM > 10 in other cell types in the mice scRNA-seq dataset[55], or the mean expression level was less than 0.03 in neurons but greater than 0.03 in glia in the AD pathology human scRNA-seq dataset[93], and protein expression was not detected in neurons from the Tissue Atlas[94], this gene was excluded from the proteomic results. Two such genes (EPHX1 and PSAT1) were excluded from the PAAS proteome in humans with AD, and five such genes (Gsn, Ephx2, Gfap, Myh9 and Anxa2) were excluded from the PAAS proteome in AD mice. Proteomic hits that passed these thresholds were considered the final PAAS proteomes in humans with AD or AD mice. Lists of raw and filtered proteomic hits of PAASs and neuronal soma proteomes in humans with AD and AD mice can be found in Supplementary Table 1.

For GO analysis (Fig. 3a and Extended Data Figs. 4c and 7b), we uploaded the final proteomes to https://geneontology.org/ (refs. 95,96), g:profiler[97] or the ToppGene Suite search portal[98] and plotted the top 10 or top 20 retrieved terms on cellular compartment or biological process with the lowest FDRs. Pathway enrichment analysis was performed by retrieving GO biological process, cellular component and molecular function terms from g:profiler[97] using terms size 5–200. The enrichment map was visualized in Cytoscape (version 3.9.1)[99]. For Ingenuity Pathway Analysis (IPA) (Fig. 3b,c and Extended Data Fig. 4d,e), the human or mouse PAAS proteome was imported into IPA software (Qiagen, 2022 release version)[100] for canonical pathway analysis. The top IPA pathways with the lowest FDRs and potential relevance to PAAS pathology are listed. For GSEA (Fig. 4a), PLD3-labeled proteomes of humans with AD and unaffected controls were uploaded into Broad Institute GSEA software 4.3.2 (ref. 101) to perform GO analysis using default values, except the size was set to 200 to remove the larger sets from analysis. GSEA results were loaded into Cytoscape (version 3.9.1) for pathway enrichment analysis using EnrichmentMap[102] and AutoAnnotate[103] plugins with default values. Principal component analysis was performed using Qlucore Omics Explorer version 3.6 (Qlucore AB).

Immunofluorescence of fixed specimens and human iPSC-derived co-culture

The complete list of antibodies, dilution factors and immunofluorescence instructions for immunofluorescence staining of fixed specimens of humans and mice can be found in Supplementary Table 2. In brief, for mouse and human brains, fixation and vibratome sectioning was the same as described in the 'Proximity labeling in brain tissue' subsection. Heat-induced sodium citrate antigen retrieval was performed when necessary (see immunofluorescence instructions in Supplementary Table 2). Immunofluorescence staining was then performed with the following protocol: tissue was boiled in 50 mM sodium citrate with 0.05% Tween 20 at 95 °C for 45 minutes, followed by a 30-minute cool down at room temperature and rinse with PBS for three times. Primary antibody incubation was 12 hours to 3 days at 4 °C in blocking buffer (PBS with 1% BSA and 0.1% Tween 20), and secondary antibodies were incubated in blocking buffer at 4 °C overnight.

Thioflavin S (Sigma-Aldrich, T1892, 2% w/v stock solution, 1:10,000 staining) was used for labeling amyloid deposits. Three times washes with PBST were performed before mounting tissues on slides with PermaFluor (Thermo Fisher Scientific, TA-030-FM).

For immunofluorescence of human iPSC-derived neuron–astrocyte co-culture, cells were washed three times with pre-warmed PBS before fixing with 4% PFA (ice cold) at room temperature for 20 minutes. Cells were washed with PBS for 15 minutes three times and were blocked with blocking buffer (1% BSA in PBS, plus 0.1% Tween 20) for 1 hour. Primary antibodies were diluted in blocking buffer and incubated with cells at 4 °C overnight. Cells were washed with PBST for 15 minutes three times. Secondary antibodies were diluted in blocking buffer and incubated with cells at 4 °C overnight. Thioflavin S (2% w/v stock solution, 1:10,000 staining) was diluted in PBS and incubated with cells at room temperature for 5 min. Cells were washed with PBST for 15 min three times before imaging.

Fixed tissue and live cell time-lapse confocal microscopy imaging

An upright or an inverted Leica SP8 confocal microscope was used to generate all images. Laser and detector settings (GaAsP hybrid detection system, photon counting mode) were maintained constant. For all analyses, single z-stack images or tiled images were obtained in the somatosensory cortex in mice. All images were obtained using a ×63 oil immersion objective (numerical aperture (NA) 1.40), ×40 water immersion objective (NA 1.10) or ×25 water immersion objective (NA 0.95) at 1,024 × 1,024-pixel resolution and z-step size of 1 µm, as we previously described[31]. When indicated, deconvolution was performed using the default setting in Leica SP8 LAS X software. For time-lapse imaging of spheroid growth in human neurons, 96-well plates were imaged in a Leica SP8 incubator, with the temperature set at 37 °C and supplied with CO_2. Tilling images were obtained using a ×63 oil immersion objective (NA 1.40) at 512 × 512-pixel resolution, zoom factor at 3 and z-step size of 1 µm or 1.5 µm at every day for 7 days.

Lentivirus plasmid purification, lentivirus production and concentration

Escherichia coli stocks for pMDLg/pRRE (MDL), pRSV-Rev (Rev), pCMV-VSV-G (VSVG), FUW-M2rtTA and pLV-TetO-hNGN2-eGFP-Puro were purchased from Addgene (12251, 12253, 8454, 20342 and 79823, respectively). Bacteria was grown in 500 ml of LB broth (Thermo Fisher Scientific, DF0446-07-5) with 100 µg ml^{-1} ampicillin (Sigma-Aldrich, A9518) overnight at 37 °C with shaking. The next day, bacterial cells were pelleted by centrifugation at 4,000*g* for 10 minutes at 4 °C. The supernatant was discarded, and plasmids were purified using a PureLink HiPure Plasmid Filter Maxiprep Kit (Invitrogen, K210017), following the manufacturer's instructions.

Third-generation lentiviral vectors were produced as we previously described[104]. In brief, HEK293T cells (Invitrogen, R700-07) were grown in 15-cm plates (Falcon, 353025) in DMEM (Gibco, 12430054) supplemented with 10% FBS (Gibco, 10438026) until reaching 70–80% confluency. For cell transfection, the following solution was prepared in 500 µl of pre-warmed Opti-MEM (Gibco, 31985062) per plate: 12.2 µg of transfer plasmid, 8.1 µg of MDL, 3.1 µg of Rev, 4.1 µg of VSVG and 110 µL of polyethylenimine (1 µg µl^{-1}; Polysciences, 23966-2). This solution was incubated for 10 minutes at room temperature, vortexed gently and added dropwise onto HEK293T cells for transfection. Medium was changed after 6 hours of incubation and harvested at 48 hours and 72 hours after transfection. Media containing viral particles were sterile filtered and concentrated using a Lenti-X Concentrator (Takara Bio, 631231), according to the manufacturer's instructions.

Human neuron–astrocyte co-culture AD model

Human iPSC control lines 3182-3 and 2607 were used in this study, as we first described this line in ref. 91. Maintenance and passaging of human iPSCs were performed as we previously described[105]. Human primary astrocytes (Thermo Fisher Scientific, N7805200, or ScienCell, 1800) were maintained as described in the user manual. iPSC-derived NGN2-induced glutamatergic neuron generation was performed as we previously described[105]. In brief, human iPSCs maintained in six-well plates were harvested by incubating in Accutase (Innovative Cell Technologies, AT104) 1 ml per well plus 10 µM ROCK inhibitor THX (RI) (Tocris, 1254) at 37 °C for 20 minutes. Dissociated iPSCs were then collected in a 50-ml Falcon tube and mixed well with DMEM (Thermo Fisher Scientific, 11966025) (preferably 1:3 Accutase: DMEM). iPSCs were centrifuged for 4 minutes at room temperature at 1,000*g*. iPSCs were resuspended in 1–2 ml of StemFlex (Thermo Fisher Scientific) with 10 µM RI and counted and diluted in StemFlex with THX to a cell suspension concentration of 1×10^6 cells per milliliter. Lentiviruses NGN2-Puro and rtTA (titer 4.40×10^{10} gc ml^{-1}) at 50 µl per 10^6 cells of suspension were added. Cells were mixed and dispensed at 120,000 cells per well (six-well size) coated with 1× Geltrex (Thermo Fisher Scientific). Cells were incubated at 37 °C in an incubator overnight. Days in vitro (DIV) 1: media were replaced with induction media (DMEM F-12 with GlutaMAX and sodium pyruvate (Thermo Fisher Scientific, 10565018), 1% N-2 (Thermo Fisher Scientific, 17502048), 2% B-27-RA (Thermo Fisher Scientifiic, 12587010) and doxycycline for a final concentration of 1 µg ml^{-1}). DIV2 and DIV3: media were replaced with induction media containing puromycin (2 µg ml^{-1}) on each day. DIV4: neurons were dissociated with Accutase plus 10 µM RI for 20 minutes, washed off with 1:3 DMEM, resuspended and centrifuged at 1,000*g* for 5 minutes. Pellet was resuspended at a concentration of 1×10^6 cells per milliliter in neuron media (BrainPhys; STEMCELL Technologies, 05790), 1% N-2, 2% B-27-RA, 1 µg ml^{-1} Natural Mouse Laminin (Thermo Fisher Scientific, 23017015), 20 ng ml^{-1} BDNF (R&D Systems, 248), 20 ng ml^{-1} GDNF (R&D Systems, 212), 250 µg ml^{-1} dibutyryl cyclic-AMP (Sigma-Aldrich, D0627), 200 µM L-ascorbic acid (Sigma-Aldrich, A4403) and 1× Anti-Anti (Thermo Fisher Scientific) with doxycycline 1 µg ml^{-1}, puromycin 2 µg ml^{-1}, 4 µM AraC (Sigma-Aldrich, C6645) and 10 µM RI. Neurons were re-plated onto 2× Geltrex-coated 96-well-plates (PerkinElmer, 6055302) and seeded at 1×10^5 per well (96-well plate size). DIV5: media were replaced with neuron medium containing puromycin 2 µg ml^{-1} and AraC 4 µM. DIV6: media were replaced with neuron medium with 4 µM AraC. DIV8: media were replaced with neuron medium with 2 µM AraC. DIV10: human primary astrocytes were dissociated with TrypLE (Thermo Fisher Scientific), washed with DMEM, centrifuged at 400 rcf for 5 minutes, counted and plated into NGN2 neurons culture at 20,000 cells per well (96-well plate size). Human iPSC-derived neuron–astrocyte co-culture was maintained as previously described[57] with modifications. In brief, human neuron–astrocyte co-cultures were maintained in neuron media plus 1.5% FBS for 1 week and then FBS was reduced to 0.5% for another week. Media were half-changed every other day. After that, human neuron–astrocyte co-cultures were maintained in neuron maintenance medium (1× BrainPhys Basal (STEMCELL Technologies), 1× B27 with vitamin A (Thermo Fisher Scientific), 1× N2 (Thermo Fisher Scientific), 5 µg ml^{-1} cholesterol (Sigma-Aldrich), 1 mM creatine (Sigma-Aldrich), 10 nM β-estradiol, 200 nM ascorbic acid, 1 mM cAMP (Sigma-Aldrich), 20 ng ml^{-1} BDNF (PeproTech), 20 ng ml^{-1} GDNF (PeproTech), 1 µg ml^{-1} laminin, 0.5 mM GlutaMAX (Thermo Fisher Scientific), 1 ng ml^{-1} TGF-β1 (PeproTech), 1× normocin (InvivoGen), 50 U ml^{-1} penicillin– streptomycin (Thermo Fisher Scientific)) with half-change of media every other day until harvest or other assays. For AD modeling, Aβ1–42 peptide (AnaSpec, AS-72216) was oligomerized to prepare soluble Aβ species as previously described[57,106]. In brief, soluble Aβ species were added to the neuron maintenance medium at a final concentration of 5 µM and applied to the human neuron–astrocyte co-culture for 7 days, with half-change of media every other day as previously described[57].

For mTOR signaling inhibition, Torin1 (Tocris, 4247) or vehicle DMSO was added to the neuron maintenance medium at a final concentration of 250 nM (ref. 59) and applied to the human neuron–astrocyte co-culture 3 days before Aβ treatment. Then, Torin1 or vehicle DMSO was added to the neuron maintenance medium at 250 nM concentration, along with soluble Aβ species at 5 µM concentration, and applied to the human neuron–astrocyte co-culture for 7 days, with a half-change of media every other day. For Torin1 treatment after axon spheroid formation, soluble Aβ species at 5 µM concentration was applied to the human neuron–astrocyte co-culture for 7 days, and then Torin1 or vehicle DMSO was added to the neuron maintenance medium at 250 nM concentration for another 7 days.

For time-lapse imaging of spheroid growth in human neurons, AAV9-hSyn-mCherry (Addgene, 114472) and AAV2-CAG-LAMP1-GFP (home produced as we previously described[4]) were co-transduced at 2×10^9 vg per 100 µl of medium in 4-month-old co-cultures. Human neuron–glia co-cultures were treated with amyloid at day 150. Time-lapse confocal imaging was performed several hours before the treatment and imaged every day after treatments.

Calcium imaging in iPSC-derived human neurons

AAV1-CAMKII-GCamp8f (Addgene, 176750, 7×10^{12} vg ml^{-1}) was transduced in 2-month-old iPSC-derived human neurons, along with AAV9-CB7-mCherry (Addgene, 105544, 1×10^{13} vg ml^{-1}) at 1 µl per 0.2 Mio cells. Transduced cells were maintained with regular media changes. Calcium imaging was performed 1 month after transduction. Calcium imaging was performed using an Andor Dragonfly spinning disk confocal on a Nikon Ti2-E microscope. A ×20/0.75 NA air objective and a Zyla scientific complementary metaloxide semiconductor (sCMOS) camera were used. Imaging was performed in culture medium, and a stage-top incubator and objective heater (Oko-Lab) maintained the sample temperature at 37 °C. For stimulated calcium imaging, a pair of tinfoil wire electrodes separated approximately 1.5 mm apart were placed in the bottom of the well using a micromanipulator and used for electrical stimulation. Electric stimulation was performed using the trigger out function in the Andor software. GCaMP8f-labeled neurons were imaged through excitation at 488-nm wavelength with the acquisition speed of 20 Hz and 512 × 512 resolution. Stimulation trains of 20-ms pulses were delivered to the electrodes at 50 Hz (20-ms interval) with 300–700-µA currents for 1 second. Electric stimulation was triggered automatically at the 100-frame timepoint, and image for 300–500 frames in total. The calcium responses within the imaging window were monitored upon stimulation.

Calcium imaging raw data were de-noised using DeepCAD-RT[107]. The denoising model was trained with the different datasets acquired with the same imaging conditions. The denoised GCaMP8f fluorescence intensity was normalized to $\Delta F/F$ for analysis. Several regions of interest (ROIs) were selected on each axon. The average ΔF before stimulation was used as the baseline measurement. The raw fluorescence intensity over time ($F(t)$) contained background noise. To isolate the stimulus-evoked signal, we first calculated the average background fluorescence intensity (F_0) using data from before stimulus presentation. We then normalized the signal by subtracting F_0 at each timepoint:

$$\frac{\Delta F}{F} \equiv \frac{F(t) - F_0}{F_0}$$

This normalized signal was smoothed using a Savitzky–Golay filter with a window length of 21 data points (1 second) and a polynomial order of 3. This filtering reduced noise while preserving the overall shape of the signal. To quantify the rising slope of the calcium response, we identified the peak of the smoothed signal. The timepoint halfway to this peak ($t_{1/2}$) was then determined. A linear regression was performed using the nine data points surrounding $t_{1/2}$. The slope of this regression line provided an estimate of the rising slope of the calcium signal in response to the sensory stimulus.

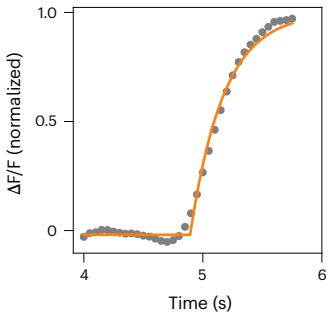

To determine the onset time of the response for each ROI after electrical stimulation, we employed an exponential growth model to fit the rising phase of the signal. Before reaching its peak, the normalized calcium trace can be effectively approximated using the following piecewise function:

$$f(t) = \begin{cases} f_0, & t < t_s \\ f_0 + (f_{\max} - f_0)(1 - e^{-(t-t_s)/\tau}), & t \geq t_s \end{cases}$$

The curve fitting procedure was performed using the curve_fit function available in the scipy.optimize package. In this context, f_0 and $f_{\max}$ represent the baseline and maximum normalized calcium signals, respectively. The parameter τ characterizes the timescale of the rising phase, and t_s denotes the response time—the specific timepoint at which the calcium signal initiates its ascent.

The calcium decay time constant (τ) was estimated by fitting 2.5-second calcium trace beginning from the peak to an exponential equation: $Y = a \times \exp(-x/\tau)$.

Viral-mediated *Mtor* heterozygous knockout in *Mtor*-floxed 5×FAD mice

mTOR is known to be a regulator of cell growth[35,59], and previous studies showed that cell size was indistinguishable between the *Mtor* heterozygous knockout and WT cells[108], which suggests that the effects of *Mtor* knockout on cell size is *Mtor* gene copy dose dependent. Thus, we obtained *Mtor* heterozygous floxed AD mice to achieve conditional *Mtor* heterozygous knockout, which had no effect on cell body size (Fig. 6o and Supplementary Fig. 10d). To achieve global neuronal *Mtor* heterozygous knockout in *Mtor*-floxed 5×FAD mice, 10 µl of AAV-PHPeB-hsyn-cre-eGFP (Addgene, 105540, titer ~1×10^{13} vg ml^{-1}) or AAV-PHPeB-CAG-GFP (Addgene, 37825, titer ~1×10^{13} vg ml^{-1}) was retro-orbitally injected into 6-week-old *Mtor*-floxed 5×FAD mice. To achieve sparse neuronal *Mtor* heterozygous knockout, 1 µl of AAV9-hsyn-cre-2a-tdT (Addgene, 107738, titer ~1×10^{13} vg ml^{-1}) was diluted with 3 µl of PBS and injected into the subarachnoid space of one hemisphere at the level of somatosensory cortex in *Mtor*-floxed 5×FAD mice, as we previously described[31]. Mouse brains were collected 2 months after virus injection in the AAV-PHPeB experiment or at 2.5 months for the AAV9-hsyn-cre-2a-tdT-injected mice. Brains were sliced, stained and imaged with confocal microscopy as mentioned above and as we previously described[31]. For sparsely PHP.eB-hSyn-Cre-GFP virus labeling in mouse brains, 3 µl of AAV-PHPeB-hsyn-cre-eGFP (Addgene, 105540, titer ~1×10^{13} vg ml^{-1}) was diluted in 30 µl of PBS and retro-orbitally injected.

RNAscope in 5×FAD mice brain slices

5×FAD mice brains were freshly dissected and immediately froze in Tissue-Tek optimal cutting temperature (OCT) compound (Sakura) and kept in dry ice with 70% ethanol for 5 –10 minutes and then transferred to −80 °C for long-term storage. Frozen brain blocks were sectioned at 10-µm thickness by cryostat (Leica). RNAscope was performed using an RNAscope Multiplex Fluorescent Kit V2 (ACD, 323270) according to the fresh frozen tissue protocol. Poly(A) probe (ACD, 318631) or negative control probe (ACD, 320871) was used during probe incubation.

Before counterstain with DAPI and mounting media, Atto 657 NHS ester (Millipore, 07376) was diluted 1:100, and brain sections were stained for 10 minutes, followed by three-times PBS washes, 5 minutes per wash. Negative control samples were used to set the baseline parameters for confocal imaging, before imaging the poly(A) probe samples.

NHS ester was used to label the spheroid halo, because when we attempted to perform RNAscope and co-stain with axonal spheroid markers, such as PLD3, SMI312, APP, RAGC, ATP9A, and ATP6V0A1, we found that these antibodies were not compatible with the RNAscope protocol, a well-known limitation of this technique. Therefore, we leveraged the knowledge from pan-expansion microscopy[109] that NHS ester can be used to non-specifically label tissues and reveal subcellular structures using confocal imaging. We applied NHS ester after RNAscope, ensuring that the NHS ester staining did not interfere with the poly(A) probe signal from RNAscope. Interestingly, in the cortex of 5×FAD mice, NHS ester highlighted the neuritic plaque nicely, allowing us to use it as a marker for spheroids, especially at the periphery of the halo.

Puromycylation in live mouse brains

Puromycylation was performed as previously described[110] with a few modifications. In brief, 25 mg of puromycin (Sigma-Aldrich, P7255) was diluted in 278 µl of DMSO to make the puromycin stock solution. Puromycin working solution includes 10 µl of puromycin stock solution, 10 µl of DMSO and 80 µl of PEG400 (puromycin final concentration at 9 mg ml^{-1}). Anisomycin (Sigma-Aldrich, 9789) stock solution was made as follows: 20 µl of DMSO was added to 5 mg of anisomycin and centrifuged at 200*g* for 3 minutes. Heat in a 42 °C water bath for 2–3 minutes, until the pipette completely dissolves. Then, 40 µl of PEG400 was added dropwise with agitation. Solution should be kept clear with no precipitation. Anisomycin working solution was made as follows: 30 µl of anisomycin stock solution, 10 µl of puromycin stock solution (or DMSO vehicle) and 60 µl of PEG400. To make Torin1 stock solution, 10 mg of Torin1 was added to 3.292 ml of DMSO and 3.292 ml of PEG400 (Torin1 final concentration at 2.5 mM). Torin1 working solution was made as follows: 30 µl of Torin1 stock, 10 µl of puromycin stock (or DMSO vehicle) and 60 µl of PEG400. All the reagents were freshly made and checked that there was no precipitation during the experiment. Mice craniotomy at the somatosensory cortex was done as we previously described[4]. After removing dura, vehicle or anisomycin or Torin1 working solution was topically applied to the cranial window. For anisomycin assay, solution was applied for 30 minutes and then quickly removed and replaced with anisomycin plus puromycin solution for 10 minutes. After quick PBS washes, mice were transcardially perfused with PBS and 4% PFA. For Torin1 treatment, drugs were incubated for 2 hours, with reapplication three times to avoid drying. Brains were vibratome sectioned at 50-µm thickness. Sections were incubated for 20 minutes with co-extraction buffer (50 mM Tris-HCl, pH 7.5, 5 mM $MgCl_2$, 25 mM KCl, protease inhibitor (Roche) and 0.015% digitonin (Wako Chemicals, 043-21376)). After three rinses with PBS, sections were incubated in blocking buffer (0.05% saponin, 10 mM glycine and 5% FBS in PBS) for 30 minutes. Then, sections were incubated in blocking buffer with puromycin 647 antibody (Millipore, MAB E343-AF647, 1:1,000), NeuN antibody (Abcam, ab177487, 1:200) or Lamp1 (Developmental Studies Hybridoma Bank, 1D4B, 1:200) for 72 hours at 4 °C. Sections were washed with PBS 3 × 10 minutes and then incubated with secondary antibodies along with puromycin 647 at 4 °C overnight, followed by PBS washes 3 × 15 minutes.

STED imaging

STED imaging was performed as we previously described[111]. In brief, human postmortem brain tissues underwent processing using immunofluorescence staining and proximity labeling techniques outlined in the 'Proximity labeling in brain tissue' and 'Immunofluorescence of fixed specimens' subsections until the stage involving secondary antibodies and streptavidin labeling. The axonal spheroids and biotinylated proteins were labeled using STED-compatible secondary antibody Atto 594 (Sigma-Aldrich) (1:100 dilution) and Atto 647N–streptavidin (Sigma-Aldrich) (1:100 dilution). Subsequently, the tissues were mounted with Prolong Gold (Thermo Fisher Scientific) following the user manual and left in the dark at room temperature for 24–72 hours before imaging. STED imaging was carried out using a Leica SP8 STED 3X equipped with a pulsed white light laser (NKT Photonics, SuperK Extreme EXW-12) for excitation and a 775-nm pulsed laser for depletion (Onefive Katana-08HP). The alignment of excitation and STED beams was accomplished using 200-nm Crimson FluoSpheres (Thermo Fisher Scientific, F8782). Sample imaging was performed using the following parameters: Sequence 1: 594-nm laser was at 1.15 µW. Sequence 2: 646-nm laser was at 6.4 µW. Sequence 3: 646-nm laser was at 34 µW. Sequence 4: 594-nm laser was 14 µW. Sequences 3 and 4: 775-nm STED laser was at 33 mW.

Samples for focus ion beam/scanning electron microscopy

Mice brains or fixed postmortem human brains were vibratome sectioned into 50-µm thickness as described in the 'Proximity labeling in brain tissue' subsection[4]. Trimmed tissue samples were fixed in 2.5% glutaraldehyde and 2% PFA in 0.1 M sodium cacodylate buffer, pH 7.4, containing 2 mM calcium chloride for 1 hour and then rinsed in buffer and post-fixed in 1% osmium tetroxide and 1.5% potassium ferrocyanide for another hour. After rinsing well, the samples were immersed in aqueous 1% thiocarbohydrazide for 30 minutes and then well rinsed. They were then placed in 1% osmium tetroxide in water for 1 hour at room temperature, followed by rinsing in distilled water. An overnight en bloc stain in aqueous 1% uranyl acetate was followed by rinsing in distilled water, and then the samples were placed into warm lead aspartate and kept at 600 °C for 1 hour. After 1 hour of rinsing in distilled water, the samples were dehydrated through an ethanol series to 100%, followed by 100% propylene oxide. The samples were infiltrated with Durcupan (Electron Microscopy Sciences) resin over 2 days and then placed in silicone molds and baked at 600 °C for at least 48 hours. The resin block was trimmed to a rough area of interest, and the surface was cleanly cut. The entire pyramid was carefully removed with a fine blade and mounted on an aluminum stub using conductive carbon adhesive and silver paint (Electron Microscopy Sciences) and then sputtered with approximately 15-nm Platinum/Palladium (80/20) using Cressington HR sputter coating equipment (Ted Pella) to reduce charging effects.

A dual-beam focus ion beam/scanning electron microscopy (FIB/SEM) instrument (Zeiss, CrossBeam 550) using a gallium ion source was used to mill, and an SE2 secondary electron detector was used to image the samples. A SmartSEM (Zeiss) was used to set up initial parameters and to find the ROIs by SEM images at 10 kV, 45-µm width and 30-µm height. The actual depth was 22 µm with 10 nm per pixel and 10 nm per slice. A platinum protective layer was deposited at the ROI with the FIB (30 kV, 3 nA) to protect the structure and reduce charging. Milling and highlighting were done at 30 kV and 50 pA, with a carbon deposit (30 kV, 3 nA). A course trench was milled (30 kV, 30 nA), followed by fine milling (30 kV, 3 nA), and, for final acquisition, a cuboid the area of interest was milled at 30 kV and 300 pA. After milling each slice, an image was taken by detecting backscattered electrons of a primary electron beam (acceleration voltage of 1.5 kV, imaging current of 2 nA and aperture diameter of 100 µm) with a pixel dwell time of 3 µs Atlas5 (Zeiss) was used for preliminary SEM stack alignment, and FIB/SEM image stacks were saved as tiff and MRC files. The images were imported into Dragonfly software (Object Research Systems) for further alignment, segmentation and three-dimensional (3D) video.

FIB/SEM image annotation and segmentation

Images from the z-stack at different z-locations were imported into APEER (Zeiss). Spheroids and plaques within the images were then

manually annotated. After annotating 37 images, models were trained to predict each object. Then, individual spheroid and plaque segmentation models were downloaded and imported into Vision4D 4.1.0 (Arivis) for object segmentation. The entire z-stack was then segmented in the analysis pipeline via the Deep Learning Segmenter operation with all the z-stacks within the dataset. Next, non-specific and overlapping annotations were manually corrected using the Draw Objects tool. Object color and opacity were modified using the Set Object Style tab to show raw data. The z-stack was then played using the Movie Player and recorded using Capture.

Image analysis and quantification

All analyses were processed with FIJI (ImageJ) software, unless otherwise described.

1. Quantification of PLD3 raw integrated fluorescence intensity in human brain. After PLD3 immunolabeling, we compared the number and intensity of pixels corresponding to the PAAS halo versus the rest of the field of view, representing mostly neuronal soma and neuropil. For this, we used three AD postmortem brains that had been used for PAAS proteomics. Immunofluorescence staining of PLD3 and thioflavin S staining were performed, followed by confocal imaging. Background autofluorescence signals were measured in unstained brain slices and subtracted from all subsequent image quantifications to better reflect true PLD3 signal. PAAS halos were manually circled, and the raw integrated intensity (RawInt) was measured. The RawInt was also measured for the whole field of view. The sum of RawInt derived from PAAS halos was subtracted from the RawInt from the whole field of view. By subtracting the halo RawInt from the total RawInt, we obtained a measurement of the PLD3 labeling outside of plaques, which mainly consists of neuronal cell bodies, neuropil and any minimal background fluorescence.
2. p-mTOR S2448 fluorescence intensity measurement. In human AD or no/mild AD postmortem brains, each zoom 1 z-stack image, containing SMI312-positive axonal spheroids around amyloid plaques, was maximum projected. Then, SMI312-positive spheroid halos were circled, and mean fluorescence intensity of the p-mTOR S2448 channel was measured within the selected circle. In the same field of view, regions without spheroids were considered as background. Three such background regions were selected and circled, and p-mTOR mean intensity was measured. The three 'background' p-mTOR mean intensity values from each field of view were averaged. Mean intensity (p-mTOR dystrophy halo) / mean intensity (p-mTOR background) was calculated to represent the p-mTOR expression level in each axonal spheroid halo. Three fields of view were quantified in each patient with severe AD, and 1–3 fields of view were quantified in each patient with no/mild AD. The averaged p-mTOR expression level in each patient was used for statistical analysis.
3. Measurement of the size of individual axon spheroids in human iPSC-derived neurons in the Torin1 treatment experiment. SMI312 was used to label spheroids, and thioflavin S was used to label amyloid plaques. Tiling images were taken in each well from a 96-well plate and were maximum projected. For Torin1 treatment before amyloid plaque and spheroid formation, individual axonal spheroids were circled using the freehand tool in ImageJ, and the circle area was measured. The total number of axonal spheroid halos analyzed ranged from 50 to 150 within each tilling image. Two technical replicate wells were analyzed in each experiment, and three batches of experiments were performed for quantification. For Torin1 treatment after amyloid plaque and spheroid formation, machine-learning-based image analysis software Aivia version 12 (Leica) was used to quantify the size and number of spheroids and amyloid plaques as well as axon density in an automated fashion. The pixel classifier tool was used to classify each channel.
4. Measurement of the percentage of axonal segments with spheroids in human iPSC-derived neurons in the Torin1 treatment experiment. The SMI312 staining revealed both axonal spheroids (the spheroid shape) and axons (the linear shape), therefore allowing us to recognize individual axon segments. To quantify axons with spheroids, we traced individual axon segments with linear and continuous signal across the z-stacks within the field of view. An axon with one or more spheroids formed was defined as axon with spheroid, whereas axon segments without spheroids observed within the z-stack were defined as axons without spheroids. In Fig. 6l, the percentage of axons with spheroids was calculated by comparing the number of axonal segments with spheroids over the total number of axonal segments that were observed within the field of view.
5. Measurement of human neuron cell body size with or without Torin1 treatment. iPSC co-cultures were infected by AAV2-CB7-GFP (Addgene, 105542) at titer ~7×10^9 vg ml^{-1} 1 week before Torin1 and Aβ treatment. Cells were stained with NeuN and GFP antibodies. Large field tilling imaging was performed in each well. Tilling images were maximum projected, and neurons with both NeuN and GFP positive signals were measured by size, using the freehand tool in ImageJ. Three technical replicate wells were analyzed in each experiment, and two batches of experiments were done for quantification.
6. Individual axonal spheroid size measurement in the AAV9-hSyn-cre-2a-tdT infected *Mtor*-flox 5×FAD mice. Anti-Lamp1 antibody was used for immunofluorescence staining to showcase the spheroid halo around amyloid plaques; thioflavin S was used to label amyloid plaques; and anti-RFP antibody was used to reveal the tdTomato expression in infected neurons. Tilling images were taken at the somatosensory cortex of each animal. Three serial brain sections were used for tilling imaging for each mouse. An individual spheroid was counted when it was both tdTomato positive and Lamp1 positive. The individual spheroid size was measured using the freehand tool in ImageJ to circle the outline of spheroids, where it had the maximum diameter, followed by measurement of the circled area. The total number of axonal spheroid halos analyzed ranged from 50 to 150 in each tilling image.
7. Measurement of spheroid halo size in the AAV-PHPeB-infected *Mtor*-flox 5×FAD experiment. Anti-Lamp1 antibody was used for immunofluorescence staining to showcase the spheroid halo around the amyloid plaque, and thioflavin S was used to label amyloid plaques. Tilling images were taken at the somatosensory cortex of each animal. Three serial brain sections were used for tilling imaging for each mouse. A customized ImageJ macro was used to segment individual Lamp1-positive spheroid halos and amyloid plaques. Using a customized MATLAB program, the segmented images were processed to measure the area of individual spheroid halos and amyloid plaque area, automatically. The spheroid halo area was excluding the area in the center occupied by the amyloid plaque. The number of axonal spheroid halos and amyloid plaques analyzed ranged from 30 to 70 in each tilling image from the *Mtor*-flox 5×FAD experiment.
8. Measurement of RNA signals within axonal spheroids. The ImageJ freehand tool was used to circle axonal spheroid structures labeled by Atto 647 NHS ester, and fluorescence intensity from poly(A) probe channel or negative control probe channel was measured. For measuring puromycin signals within axonal spheroids or neuronal cell bodies, similarly, the ImageJ freehand tool was used to circle axonal spheroid or cell bodies labeled by Lamp1 or NeuN, respectively, and fluorescence intensity from puromycin channel was measured.

9. Measurement of NeuN-positive neuronal cell soma area in AAV-PHPeB-infected *Mtor*-flox 5×FAD mice. A customized CellProfiler program was used for automated measurement. In brief, tilling images were taken from one hemisphere of the somatosensory cortex. Tilling images were maximum projected before importing them into CellProfiler (Broad Institute). The NeuN channel was set as the primary object and was used as the marker for size measurement. Three tilling images were taken from three brain sections of each animal. Three animals were used in each group.
10. Investigation of mTOR heterozygous knockout downstream signaling effectors in mTOR-floxed 5×FAD mice. Similarly, a customized CellProfiler program was used for automated measurement. Tilling images were maximum projected before analysis. To analyze fluorescence intensity in the nuclei, we used DAPI staining as the primary object and measured signals from the NeuN-positive cells. To measure fluorescence intensity from the cell bodies, the NeuN channel was set as the primary object and was used as the marker for fluorescence intensity measurement. We compared mice injected with PHPeB-hSyn-cre-GFP viruses to those injected with control viruses PHPeB-CAG-GFP. The littermates and sex were paired for comparison. Immunofluorescence intensity of TFEB was measured in neuronal nuclei, whereas LC3B, P-p70S6K Thr389 and p70S6K were measured in neuronal soma in an automated fashion.

Statistics and reproducibility

Each experiment was repeated independently for at least three times with similar results. Human or mouse samples were grouped by disease stages or ages. Mice were paired by littermate and sex, as indicated in the figure legends. No statistical method was used to predetermine sample size, but our sample sizes were similar to those generally employed in the field. No data were excluded from the analyses. The investigators were not blinded to allocation during experiments and outcome assessment, but we used codes or software to analyze data in an automated and unbiased way whenever possible. Excel (Microsoft), Prism (GraphPad Software), Qlucore Omics Explorer version 3.6 (Qlucore AB), CellProfiler version 4.2.1 (Broad Institute), MATLAB and RStudio (4.0.2) were used for data analysis and plotting. Statistical methods used and *P* values are described in the figure legend of each relevant panel. All statistical tests were two-sided, including all figures and tables in the main text, extended data or supplementary data.

Reporting summary

Further information on research design is available in the Nature Portfolio Reporting Summary linked to this article.

Data availability

Raw proteomics data are provided in Supplementary Table 1. The mass spectrometry proteomics data have been deposited to the ProteomeXchange Consortium via the PRIDE partner repository with the dataset identifier PXD040310. The Lamp1 dataset is under the identifier PXD048097. For sample information, see Supplementary Table 3. All other data are available from the corresponding author upon reasonable request.

Code availability

Custom codes for FIJI and MATLAB were deposited at GitHub (https://github.com/PaulYJ/Axon-spheroid) as we previously described[4].

The Python and R codes for the analysis of calcium imaging and spheroid size distribution can be accessed at the following GitHub repository: https://github.com/ShawnQin/calcium_trace.

The code for the analysis of STED imaging data can be accessed at https://github.com/bewersdorflab/Yifei-Lukas-Collab.

References

1. Knopman, D. S. et al. Alzheimer disease. *Nat. Rev. Dis. Primers* **7**, 33 (2021).
2. Spires-Jones, T. L. & Hyman, B. T. The intersection of amyloid beta and tau at synapses in Alzheimer's disease. *Neuron* **82**, 756–771 (2014).
3. Tsai, J. et al. Fibrillar amyloid deposition leads to local synaptic abnormalities and breakage of neuronal branches. *Nat. Neurosci.* **7**, 1181–1183 (2004).
4. Yuan, P. et al. PLD3 affects axonal spheroids and network defects in Alzheimer's disease. *Nature* **612**, 328–337 (2022).
5. Adalbert, R. et al. Severely dystrophic axons at amyloid plaques remain continuous and connected to viable cell bodies. *Brain* **132**, 402–416 (2009).
6. Nardocci, N. & Zorzi, G. Axonal dystrophies. *Handb. Clin. Neurol.* **113**, 1919–1924 (2013).
7. Tourtellotte, W. G. & Hoesen, G. W. Van The axonal origin of a subpopulation of dystrophic neurites in Alzheimer's disease. *Neurosci. Lett.* **129**, 11–16 (1991).
8. Vickers, J. C. et al. Dystrophic neurite formation associated with age-related beta amyloid deposition in the neocortex: clues to the genesis of neurofibrillary pathology. *Exp. Neurol.* **141**, 1–11 (1996).
9. Yasuhara, O. et al. Two types of dystrophic neurites in senile plaques of Alzheimer disease and elderly non-demented cases. *Neurosci. Lett.* **171**, 73–76 (1994).
10. Alzheimer, A. et al. An English translation of Alzheimer's 1907 paper, 'Uber eine eigenartige Erkankung der Hirnrinde'. *Clin. Anat.* **8**, 429–431 (1995).
11. McKee, A. C., Kosik, K. S. & Kowall, N. W. Neuritic pathology and dementia in Alzheimer's disease. *Ann. Neurol.* **30**, 156–165 (1991).
12. Kolaric, K. V. et al. Focal axonal swellings and associated ultrastructural changes attenuate conduction velocity in central nervous system axons: a computer modeling study. *Physiol. Rep.* **1**, e00059 (2013).
13. Wu, Y. T., Gilpin, K. & Adnan, A. Effects of focal axonal swelling level on the action potential signal transmission. *J. Comput. Neurosci.* **48**, 253–263 (2020).
14. Gowrishankar, S. et al. Massive accumulation of luminal protease-deficient axonal lysosomes at Alzheimer's disease amyloid plaques. *Proc. Natl Acad. Sci. USA* **112**, E3699–E3708 (2015).
15. Nixon, R. A. et al. Extensive involvement of autophagy in Alzheimer disease: an immuno-electron microscopy study. *J. Neuropathol. Exp. Neurol.* **64**, 113–122 (2005).
16. Lee, S., Sato, Y. & Nixon, R. A. Lysosomal proteolysis inhibition selectively disrupts axonal transport of degradative organelles and causes an Alzheimer's-like axonal dystrophy. *J. Neurosci* **31**, 7817–7830 (2011).
17. Wolfe, D. M. et al. Autophagy failure in Alzheimer's disease and the role of defective lysosomal acidification. *Eur. J. Neurosci.* **37**, 1949–1961 (2013).
18. Stokin, G. B. et al. Axonopathy and transport deficits early in the pathogenesis of Alzheimer's disease. *Science* **307**, 1282–1288 (2005).
19. Pigino, G. et al. Disruption of fast axonal transport is a pathogenic mechanism for intraneuronal amyloid beta. *Proc. Natl Acad. Sci. USA* **106**, 5907–5912 (2009).
20. Sadleir, K. R. et al. Presynaptic dystrophic neurites surrounding amyloid plaques are sites of microtubule disruption, BACE1 elevation, and increased Aβ generation in Alzheimer's disease. *Acta Neuropathol.* **132**, 235–256 (2016).
21. Roney, J. C. et al. Lipid-mediated motor-adaptor sequestration impairs axonal lysosome delivery leading to autophagic stress and dystrophy in Niemann-Pick type C. *Dev. Cell* **56**, 1452–1468 (2021).

22. Yong, Y. et al. Axonal spheroids in neurodegeneration. *Mol. Cell. Neurosci.* **117**, 103679 (2021).
23. Sanchez-Varo, R. et al. Abnormal accumulation of autophagic vesicles correlates with axonal and synaptic pathology in young Alzheimer's mice hippocampus. *Acta Neuropathol.* **123**, 53–70 (2012).
24. Essuman, K. et al. The SARM1 Toll/interleukin-1 receptor domain possesses intrinsic NAD^+ cleavage activity that promotes pathological axonal degeneration. *Neuron* **93**, 1334–1343 (2017).
25. Gerdts, J. et al. SARM1 activation triggers axon degeneration locally via NAD^+ destruction. *Science* **348**, 453–7 (2015).
26. He, Z. et al. Amyloid-β plaques enhance Alzheimer's brain tau-seeded pathologies by facilitating neuritic plaque tau aggregation. *Nat. Med.* **24**, 29–38 (2018).
27. Knowles, R. B. et al. Plaque-induced neurite abnormalities: implications for disruption of neural networks in Alzheimer's disease. *Proc. Natl Acad. Sci. USA* **96**, 5274–5279 (1999).
28. Vickers, J. C. et al. Axonopathy and cytoskeletal disruption in degenerative diseases of the central nervous system. *Brain Res. Bull.* **80**, 217–223 (2009).
29. Yong, Y. et al. Regulation of degenerative spheroids after injury. *Sci. Rep.* **10**, 15472 (2020).
30. Wang, Y. et al. TREM2-mediated early microglial response limits diffusion and toxicity of amyloid plaques. *J. Exp. Med.* **213**, 667–675 (2016).
31. Yuan, P. et al. TREM2 haplodeficiency in mice and humans impairs the microglia barrier function leading to decreased amyloid compaction and severe axonal dystrophy. *Neuron* **92**, 252–264 (2016).
32. Condello, C. et al. Microglia constitute a barrier that prevents neurotoxic protofibrillar Aβ42 hotspots around plaques. *Nat. Commun.* **6**, 6176 (2015).
33. Sardiello, M. et al. A gene network regulating lysosomal biogenesis and function. *Science* **325**, 473–477 (2009).
34. Manning, B. D. & Toker, A. AKT/PKB signaling: navigating the network. *Cell* **169**, 381–405 (2017).
35. Saxton, R. A. & Sabatini, D. M. mTOR signaling in growth, metabolism, and disease. *Cell* **168**, 960–976 (2017).
36. Branon, T. C. et al. Efficient proximity labeling in living cells and organisms with TurboID. *Nat. Biotechnol.* **36**, 880–887 (2018).
37. Rhee, H. W. et al. Proteomic mapping of mitochondria in living cells via spatially restricted enzymatic tagging. *Science* **339**, 1328–1331 (2013).
38. Roux, K. J. et al. A promiscuous biotin ligase fusion protein identifies proximal and interacting proteins in mammalian cells. *J. Cell Biol.* **196**, 801–810 (2012).
39. Uezu, A. et al. Identification of an elaborate complex mediating postsynaptic inhibition. *Science* **353**, 1123–1129 (2016).
40. Mathew, B. et al. Deciphering spatial protein–protein interactions in brain using proximity labeling. *Mol. Cell. Proteomics* **21**, 100422 (2022).
41. Li, J. et al. Cell-surface proteomic profiling in the fly brain uncovers wiring regulators. *Cell* **180**, 373–386 (2020).
42. Loh, K. H. et al. Proteomic analysis of unbounded cellular compartments: synaptic clefts. *Cell* **166**, 1295–1307 (2016).
43. Bar, D. Z. et al. Biotinylation by antibody recognition—a method for proximity labeling. *Nat. Methods* **15**, 127–133 (2018).
44. Killinger, B. A. et al. In situ proximity labeling identifies Lewy pathology molecular interactions in the human brain. *Proc. Natl Acad. Sci. USA* **119**, e2114405119 (2022).
45. Hashimoto, N. et al. Proteomic analysis of ganglioside-associated membrane molecules: substantial basis for molecular clustering. *Proteomics* **12**, 3154–3163 (2012).
46. Li, X. W. et al. New insights into the DT40 B cell receptor cluster using a proteomic proximity labeling assay. *J. Biol. Chem.* **289**, 14434–14447 (2014).
47. Nackenoff, A. G. et al. PLD3 is a neuronal lysosomal phospholipase D associated with β-amyloid plaques and cognitive function in Alzheimer's disease. *PLoS Genet.* **17**, e1009406 (2021).
48. Satoh, J. et al. PLD3 is accumulated on neuritic plaques in Alzheimer's disease brains. *Alzheimers Res. Ther.* **6**, 70 (2014).
49. Gonzalez, A. C. et al. Unconventional trafficking of mammalian phospholipase D3 to lysosomes. *Cell Rep.* **22**, 1040–1053 (2018).
50. Cruchaga, C. et al. Rare coding variants in the phospholipase D3 gene confer risk for Alzheimer's disease. *Nature* **505**, 550–554 (2014).
51. Gusel'nikova, V. V. & Korzhevskiy, D. E. NeuN as a neuronal nuclear antigen and neuron differentiation marker. *Acta Naturae* **7**, 42–47 (2015).
52. Liu, G. Y. & Sabatini, D. M. mTOR at the nexus of nutrition, growth, ageing and disease. *Nat. Rev. Mol. Cell Biol.* **21**, 183–203 (2020).
53. Martins, I. J. et al. Apolipoprotein E, cholesterol metabolism, diabetes, and the convergence of risk factors for Alzheimer's disease and cardiovascular disease. *Mol. Psychiatry* **11**, 721–736 (2006).
54. Masuda, T. et al. Novel Hexb-based tools for studying microglia in the CNS. *Nat. Immunol.* **21**, 802–815 (2020).
55. Zhang, Y. et al. Purification and characterization of progenitor and mature human astrocytes reveals transcriptional and functional differences with mouse. *Neuron* **89**, 37–53 (2016).
56. Zhang, Y. et al. Rapid single-step induction of functional neurons from human pluripotent stem cells. *Neuron* **78**, 785–798 (2013).
57. Bassil, R. et al. Improved modeling of human AD with an automated culturing platform for iPSC neurons, astrocytes and microglia. *Nat. Commun.* **12**, 5220 (2021).
58. Ballatore, C., Lee, V. M. & Trojanowski, J. Q. Tau-mediated neurodegeneration in Alzheimer's disease and related disorders. *Nat. Rev. Neurosci.* **8**, 663–672 (2007).
59. Thoreen, C. C. et al. An ATP-competitive mammalian target of rapamycin inhibitor reveals rapamycin-resistant functions of mTORC1. *J. Biol. Chem.* **284**, 8023–32 (2009).
60. Zhao, J. et al. mTOR inhibition activates overall protein degradation by the ubiquitin proteasome system as well as by autophagy. *Proc. Natl Acad. Sci. USA* **112**, 15790–15797 (2015).
61. Risson, V. et al. Muscle inactivation of mTOR causes metabolic and dystrophin defects leading to severe myopathy. *J. Cell Biol.* **187**, 859–874 (2009).
62. Poulopoulos, A. et al. Subcellular transcriptomes and proteomes of developing axon projections in the cerebral cortex. *Nature* **565**, 356–360 (2019).
63. Terenzio, M. et al. Locally translated mTOR controls axonal local translation in nerve injury. *Science* **359**, 1416–1421 (2018).
64. Hyman, B. T. et al. National Institute on Aging–Alzheimer's Association guidelines for the neuropathologic assessment of Alzheimer's disease. *Alzheimers Dement.* **8**, 1–13 (2012).
65. Su, J. H., Cummings, B. J. & Cotman, C. W. Identification and distribution of axonal dystrophic neurites in Alzheimer's disease. *Brain Res.* **625**, 228–37 (1993).
66. Drummond, E. et al. The amyloid plaque proteome in early onset Alzheimer's disease and Down syndrome. *Acta Neuropathol. Commun.* **10**, 53 (2022).
67. Drummond, E. et al. Proteomic differences in amyloid plaques in rapidly progressive and sporadic Alzheimer's disease. *Acta Neuropathol.* **133**, 933–954 (2017).
68. Liao, L. et al. Proteomic characterization of postmortem amyloid plaques isolated by laser capture microdissection. *J. Biol. Chem.* **279**, 37061–37068 (2004).
69. Dovas, A. & Couchman, J. R. RhoGDI: multiple functions in the regulation of Rho family GTPase activities. *Biochem. J.* **390**, 1–9 (2005).
70. Garcia-Mata, R., Boulter, E. & Burridge, K. The 'invisible hand': regulation of RHO GTPases by RHOGDIs. *Nat. Rev. Mol. Cell Biol.* **12**, 493–504 (2011).

71. Torres, M. et al. Defective lysosomal proteolysis and axonal transport are early pathogenic events that worsen with age leading to increased APP metabolism and synaptic Abeta in transgenic APP/PS1 hippocampus. *Mol. Neurodegener.* **7**, 59 (2012).
72. Yang, Y. et al. Disruption of *Tmem30a* results in cerebellar ataxia and degeneration of Purkinje cells. *Cell Death Dis.* **9**, 899 (2018).
73. Toapanta, F. R. & Ross, T. M. Complement-mediated activation of the adaptive immune responses: role of C3d in linking the innate and adaptive immunity. *Immunol. Res.* **36**, 197–210 (2006).
74. Barbu, A. et al. The role of complement factor C3 in lipid metabolism. *Mol. Immunol.* **67**, 101–107 (2015).
75. Garcia-Arguinzonis, M. et al. Alternative C3 complement system: lipids and atherosclerosis. *Int. J. Mol. Sci.* **22**, 5122 (2021).
76. Stoltzner, S. E. et al. Temporal accrual of complement proteins in amyloid plaques in Down's syndrome with Alzheimer's disease. *Am. J. Pathol.* **156**, 489–499 (2000).
77. Chen, S., Frederickson, R. C. & Brunden, K. R. Neuroglial-mediated immunoinflammatory responses in Alzheimer's disease: complement activation and therapeutic approaches. *Neurobiol. Aging* **17**, 781–787 (1996).
78. Eikelenboom, P. et al. Distribution pattern and functional state of complement proteins and α 1-antichymotrypsin in cerebral β/A4 deposits in Alzheimer's disease. *Res. Immunol.* **143**, 617–620 (1992).
79. Kim, Y. M. et al. mTORC1 phosphorylates UVRAG to negatively regulate autophagosome and endosome maturation. *Mol. Cell* **57**, 207–218 (2015).
80. Park, K. K. et al. Promoting axon regeneration in the adult CNS by modulation of the PTEN/mTOR pathway. *Science* **322**, 963–966 (2008).
81. Peterson, T. R. et al. mTOR complex 1 regulates lipin 1 localization to control the SREBP pathway. *Cell* **146**, 408–420 (2011).
82. Menon, D. et al. Lipid sensing by mTOR complexes via de novo synthesis of phosphatidic acid. *J. Biol. Chem.* **292**, 6303–6311 (2017).
83. Castellano, B. M. et al. Lysosomal cholesterol activates mTORC1 via an SLC38A9–Niemann-Pick C1 signaling complex. *Science* **355**, 1306–1311 (2017).
84. Wong, H. H., Watt, A. J. & Sjostrom, P. J. Synapse-specific burst coding sustained by local axonal translation. *Neuron* **112**, 264–276 (2023).
85. Lie, P. P. Y. et al. Axonal transport of late endosomes and amphisomes is selectively modulated by local Ca^{2+} efflux and disrupted by PSEN1 loss of function. *Sci. Adv.* **8**, eabj5716 (2022).
86. Meyer-Luehmann, M. et al. Rapid appearance and local toxicity of amyloid-β plaques in a mouse model of Alzheimer's disease. *Nature* **451**, 720–724 (2008).
87. Goltsev, Y. et al. Deep profiling of mouse splenic architecture with CODEX multiplexed imaging. *Cell* **174**, 968–981 (2018).
88. Satoh, J. I. et al. Alzheimer's disease pathology in Nasu-Hakola disease brains. *Intractable Rare Dis. Res.* **7**, 32–36 (2018).
89. Foulds, N. et al. Adult-onset leukoencephalopathy with axonal spheroids and pigmented glia caused by a novel R782G mutation in *CSF1R*. *Sci. Rep.* **5**, 10042 (2015).
90. DiFiglia, M. et al. Aggregation of huntingtin in neuronal intranuclear inclusions and dystrophic neurites in brain. *Science* **277**, 1990–1993 (1997).
91. Hoffman, G. E. et al. Transcriptional signatures of schizophrenia in hiPSC-derived NPCs and neurons are concordant with post-mortem adult brains. *Nat. Commun.* **8**, 2225 (2017).
92. Oakley, H. et al. Intraneuronal β-amyloid aggregates, neurodegeneration, and neuron loss in transgenic mice with five familial Alzheimer's disease mutations: potential factors in amyloid plaque formation. *J. Neurosci.* **26**, 10129–10140 (2006).
93. Mathys, H. et al. Single-cell transcriptomic analysis of Alzheimer's disease. *Nature* **570**, 332–337 (2019).
94. Uhlen, M. et al. Proteomics. Tissue-based map of the human proteome. *Science* **347**, 1260419 (2015).
95. Ashburner, M. et al. Gene ontology: tool for the unification of biology. The Gene Ontology Consortium. *Nat. Genet.* **25**, 25–29 (2000).
96. Gene Ontology Consortium. The Gene Ontology resource: enriching a GOld mine. *Nucleic Acids Res.* **49**, D325–D334 (2021).
97. Raudvere, U. et al. g:Profiler: a web server for functional enrichment analysis and conversions of gene lists (2019 update). *Nucleic Acids Res.* **47**, W191–W198 (2019).
98. Chen, J. et al. ToppGene Suite for gene list enrichment analysis and candidate gene prioritization. *Nucleic Acids Res.* **37**, W305–W311 (2009).
99. Shannon, P. et al. Cytoscape: a software environment for integrated models of biomolecular interaction networks. *Genome Res.* **13**, 2498–2504 (2003).
100. Kramer, A. et al. Causal analysis approaches in Ingenuity Pathway Analysis. *Bioinformatics* **30**, 523–530 (2014).
101. Subramanian, A. et al. Gene set enrichment analysis: a knowledge-based approach for interpreting genome-wide expression profiles. *Proc. Natl Acad. Sci. USA* **102**, 15545–15550 (2005).
102. Merico, D. et al. Enrichment map: a network-based method for gene-set enrichment visualization and interpretation. *PLoS ONE* **5**, e13984 (2010).
103. Kucera, M. et al. AutoAnnotate: a Cytoscape app for summarizing networks with semantic annotations. *F1000Res.* **5**, 1717 (2016).
104. Li, A. et al. Using the dCas9–KRAB system to repress gene expression in hiPSC-derived *NGN2* neurons. *STAR Protoc.* **2**, 100580 (2021).
105. Ho, S. M. et al. Rapid *Ngn2*-induction of excitatory neurons from hiPSC-derived neural progenitor cells. *Methods* **101**, 113–124 (2016).
106. Wang, M. et al. Transformative network modeling of multi-omics data reveals detailed circuits, key regulators, and potential therapeutics for Alzheimer's disease. *Neuron* **109**, 257–272 (2021).
107. Li, X. et al. Real-time denoising enables high-sensitivity fluorescence time-lapse imaging beyond the shot-noise limit. *Nat. Biotechnol.* **41**, 282–292 (2023).
108. Murakami, M. et al. mTOR is essential for growth and proliferation in early mouse embryos and embryonic stem cells. *Mol. Cell. Biol.* **24**, 6710–6718 (2004).
109. M'Saad, O. & Bewersdorf, J. Light microscopy of proteins in their ultrastructural context. *Nat. Commun.* **11**, 3850 (2020).
110. Biever, A. et al. Monosomes actively translate synaptic mRNAs in neuronal processes. *Science* **367**, eaay4991 (2020).
111. Schroeder, L. K. et al. Dynamic nanoscale morphology of the ER surveyed by STED microscopy. *J. Cell Biol.* **218**, 83–96 (2019).
112. Sharoar, M. G. et al. Sequential formation of different layers of dystrophic neurites in Alzheimer's brains. *Mol. Psychiatry* **24**, 1369–1382 (2019).
113. Shi, Q. et al. RTN1 and RTN3 protein are differentially associated with senile plaques in Alzheimer's brains. *Sci. Rep.* **7**, 6145 (2017).
114. Masliah, E. et al. An antibody against phosphorylated neurofilaments identifies a subset of damaged association axons in Alzheimer's disease. *Am. J. Pathol.* **142**, 871–878 (1993).

Acknowledgements

This project was supported by National Institute of Health (NIH) grants RF1AG058257, R01NS115544 and R01NS111961 (J.G.); a Cure Alzheimer's Fund Research Grant (J.G.); an Edward N. and Della L. Thome Memorial Foundation Grant (J.G.); a Yale/NIDA Neuroproteomics Center Pilot Project Grant 2019 (Y.C.); the BrightFocus Foundation Postdoctoral Fellowship Program in Alzheimer's Disease Research (A2021003F) (Y.C.); a Yale ADRC Research Scholar Award (Y.C.); an Alzheimer's Association Research Fellowship (23AARF-1020552) (Y.C.); Yale ADRC Grant P30 AG066508

(A.C.N.); and the following grants to K.J.B.: R01AG068030, RF1AG065926 and R56AG071291. We thank K. Williams, S. Leslie, B. Mathew and the Yale/NIDA Neuroproteomics Center (P30 DA018343) for providing experimental design advice, technical support and funding opportunities. We thank F. Collin and W. Wang from the Keck MS & Proteomics Resource at the Yale School of Medicine for processing the proteomics samples for LC–MS/MS data collections. We also thank the Keck MS & Proteomics Resource at the Yale School of Medicine for providing the necessary mass spectrometers and the accompany biotechnology tools funded, in part, by the Yale School of Medicine and by the Office of The Director, NIH (S10OD02365101A1, S10OD019967 and S10OD018034). The funders had no role in study design, data collection and analysis, decision to publish or preparation of the manuscript. I.P.S. and E.P. were supported by EMBL-EBI Core funding. We thank A. Huttner and the Yale ADRC (P30 AG066508) for providing human postmortem AD and control brain tissues. Additional MCI and AD brain tissue was provided by the Banner Sun Health Research Institute Brain and Body Donation Program of Sun City, Arizona, supported by the National Institute of Neurological Disorders and Stroke (U24 NS072026), the National Institute on Aging (P30 AG19610), the Arizona Department of Health Services (contract 211002) and the Arizona Biomedical Research Commission (contracts 4001, 0011, 05-901 and 1001). We thank N.-T. Rahman and R. Garcia Milian from the Yale Medical Library Bioinformatics Support Program for providing advice and technical support for bioinformatics analysis. We thank X. Liu, M. Graham and the Center for Cellular and Molecular Imaging Electron Microscopy Facility at Yale Medical School for assistance with the electron microscopy experiments (National Science Foundation Major Instrument Grant 1725480). We thank P. Yuan, L. Tong and M. Zhang for providing MATLAB and FIJI ImageJ coding for plaque and axonal spheroid quantification. We thank M. Zhang for generating the AAV2-CMV-LAMP-GFP viruses. We thank J. Platisa, P. O'Brien, V. Pieribone, I. Kondratiuk, D. Chowdhury, T. Biederer, S. Qiao, Y. Xue and J. Zhou for their generous help and critical advice on the calcium imaging experiments. Calcium imaging was performed using a Dragonfly spinning disk confocal from the Biederer laboratory, supported by NIH grant R01 DA018928 (to T.B.). We thank T. Spano and E. Schuman for their generous help and critical advice on the in vivo puromycylation experiments. We created schematic figures with BioRender.

Author contributions

Y.C. and J.G. conceived and designed the study. Y.C. performed proximity labeling experiments. Y.C., R.W., M.S.M., T.T.L., S.B. and A.C.N. designed the protein extraction, enrichment and digestion protocol. Y.C. performed protein extraction, enrichment and western blotting. J.K., R.W., S.B. and T.T.L. performed LC–MS/MS, protein mapping and searching. Y.C. performed proteomics data analysis. Y.C., I.P.S. and E.P. performed bioinformatics analysis. A.C.N. supervised the proteomics experiments and analysis. L.A.F. and Y.C. performed STED imaging. L.A.F., T.H. and Y.C. performed STED imaging analysis. Y.C., L.T. and L.S. performed calcium imaging in the iPSC model. L.T. and S.Q. performed calcium imaging data analysis. A.H. performed pathological evaluation of human brain specimens and provided the tissues. Y.C. and T.H. performed immunofluorescence and confocal imaging. T.H. performed immunofluorescence quantification of newly identified proteomic hits and automated tilling image analysis. Y.C., P.L.C. and K.J.B. established the human iPSC-derived neuron–astrocyte co-culture protocol. P.L.C. performed lentivirus packaging. Y.C. performed AD human neuron–astrocyte co-culture. K.J.B. supervised the human neuron–astrocyte co-culture experiment. Y.C. performed mTOR inhibition in transgenic mice. Y.C., T.H., Z.T., A.B. and K.T. performed quantifications. Y.C. and T.H. performed statistical analysis. H.-R.G. annotated the FIB/SEM video. Y.C. and J.G. prepared the manuscript. J.G. supervised the study.

Competing interests

The authors declare no competing interests.

Additional information

Extended data is available for this paper at https://doi.org/10.1038/s43587-025-00823-3.

Supplementary information The online version contains supplementary material available at https://doi.org/10.1038/s43587-025-00823-3.

Correspondence and requests for materials should be addressed to Yifei Cai or Jaime Grutzendler.

Peer review information *Nature Aging* thanks Matthew Rowan and the other, anonymous, reviewer(s) for their contibution to the peer review of this work.

Reprints and permissions information is available at www.nature.com/reprints.

Publisher's note Springer Nature remains neutral with regard to jurisdictional claims in published maps and institutional affiliations.

[1]Department of Neurology, Yale School of Medicine, New Haven, CT, USA. [2]Keck MS & Proteomics Resource, Yale School of Medicine, New Haven, CT, USA. [3]Yale/NIDA Neuroproteomics Center, Yale University, New Haven, CT, USA. [4]Department of Psychiatry, Yale University, New Haven, CT, USA. [5]John A. Paulson School of Engineering and Applied Sciences, Harvard University, Cambridge, MA, USA. [6]Department of Cell Biology, Yale University School of Medicine, New Haven, CT, USA. [7]European Molecular Biology Laboratory, European Bioinformatics Institute, Hinxton, UK. [8]Yale College, Department of Neuroscience, Yale University, New Haven, CT, USA. [9]Department of Pathology, Yale University, New Haven, CT, USA. [10]Department of Molecular Biophysics and Biochemistry, Yale University, New Haven, CT, USA. [11]Department of Genetics, Yale University, New Haven, CT, USA. [12]Department of Pharmacology, Yale University, New Haven, CT, USA. [13]Department of Neuroscience, Yale University, New Haven, CT, USA. [14]Wu Tsai Institute, Yale University, New Haven, CT, USA. [15]These authors contributed equally: Jean Kanyo, Rashaun Wilson, Shveta Bathla, Pablo Leal Cardozo, Lei Tong, Shanshan Qin, Lukas A. Fuentes, Iguaracy Pinheiro-de-Sousa, Tram Huynh, Liyuan Sun. ✉e-mail: yifei.cai@yale.edu; jaime.grutzendler@yale.edu

https://doi.org/10.1038/s43587-025-00823-3

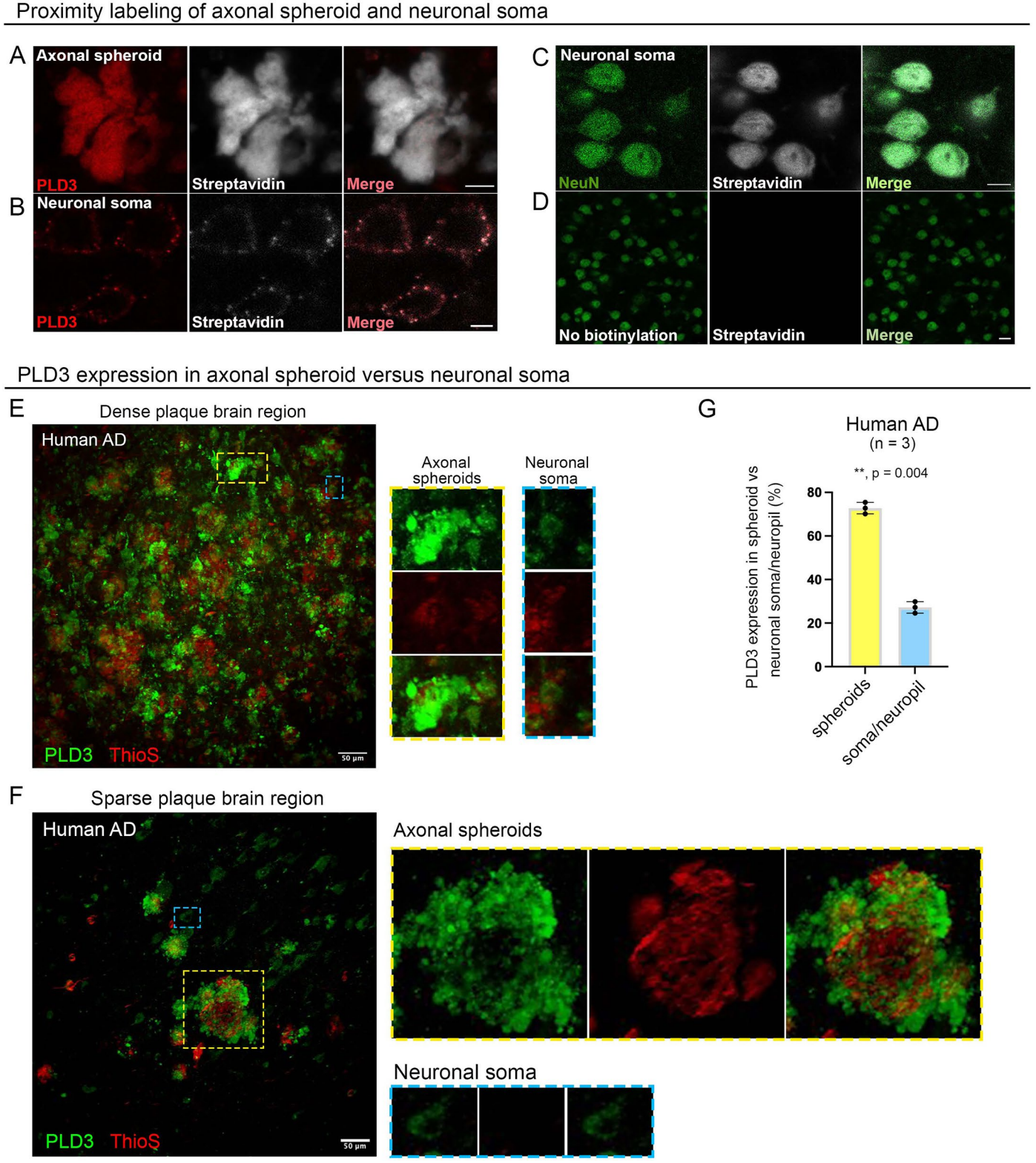

Extended Data Fig. 1 | PLD3 expression and proximity labeling of axonal spheroids versus neuronal somata. A-B. Proximity labeling of PLD3 (red) in (**A**) axonal spheroids versus (**B**) neuronal somata. **C.** Proximity labeling of NeuN (green, a neuronal soma marker). (**A-C**) Scale bar 5 µm. **D.** No biotinylation reaction control shows that the streptavidin signal was eliminated. Scale bar 50 µm. **E-G.** Comparison of PLD3 expression in axonal spheroids versus neuronal soma. Representative images of PLD3 immunofluorescence staining in AD postmortem brains with (**E**) dense amyloid plaques (ThioflavinS stained) and (**F**) sparse amyloid plaques. Inserts show axonal spheroid halos around amyloid plaques (yellow squares) or neuronal soma (blue squares). Scale bar 50 µm. **G.** Quantification of PLD3 expression in axonal spheroids versus neuronal soma/neuropil in AD human postmortem brains (n = 3 brains). Data are presented as mean values with SEM.

https://doi.org/10.1038/s43587-025-00823-3

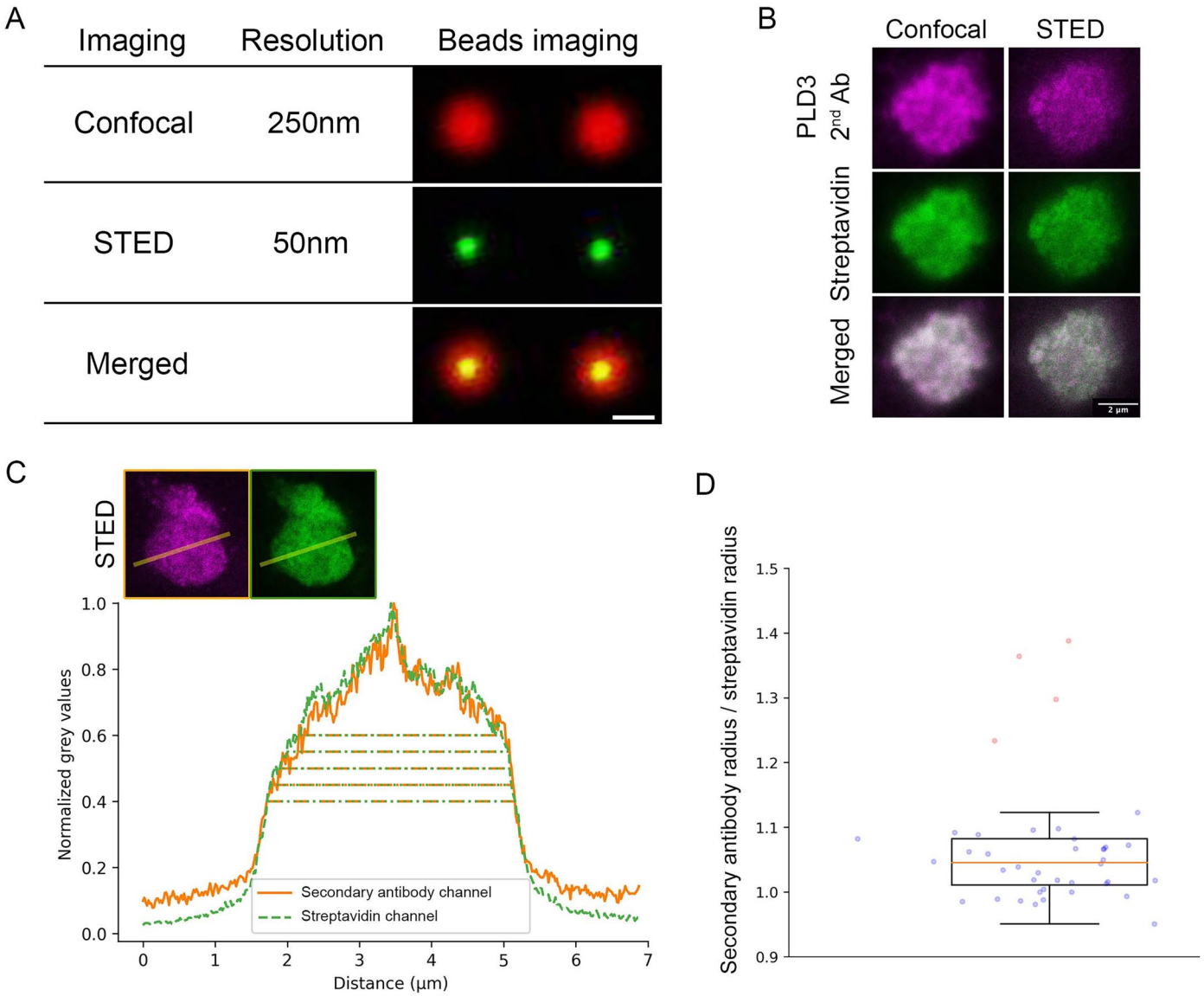

Extended Data Fig. 2 | Super-resolution STED imaging reveals high spatial precision of proximity labeling in AD human brain. A. Imaging of beads illustrates the resolution contrast between confocal microscopy (250 nm) and STED microscopy (50 nm). Scale bar = 250 nm. **B-C.** Representative confocal and STED images showing proximity labeling of axonal spheroids (magenta, anti-PLD3 labeled) in AD human postmortem brains. Biotinylated proteins were labeled by streptavidin (green). Scale bar = 2 µm. **C.** A line plot representative of the radius measurements illustrates the signals from both the secondary antibody channel (magenta) and the streptavidin channel (green). **D.** Dot plot depicting the radius ratio between the secondary antibody channel (magenta) and the streptavidin channel (green). Average radius ratio = 141.0 nm, average ratio = 1.04, standard deviation = 0.04. The median value is represented by the orange line, the lower and upper edges corresponding to the 25th (Q1) and 75th (Q3) percentiles, respectively. Whiskers extend to the minima and maxima within 1.5 times the IQR from the lower and upper quartiles. Data points beyond the whiskers are plotted as individual outliers (denoted by pink circles), and are subsequently excluded. Each dot represents a spheroid, n = 39.

https://doi.org/10.1038/s43587-025-00823-3

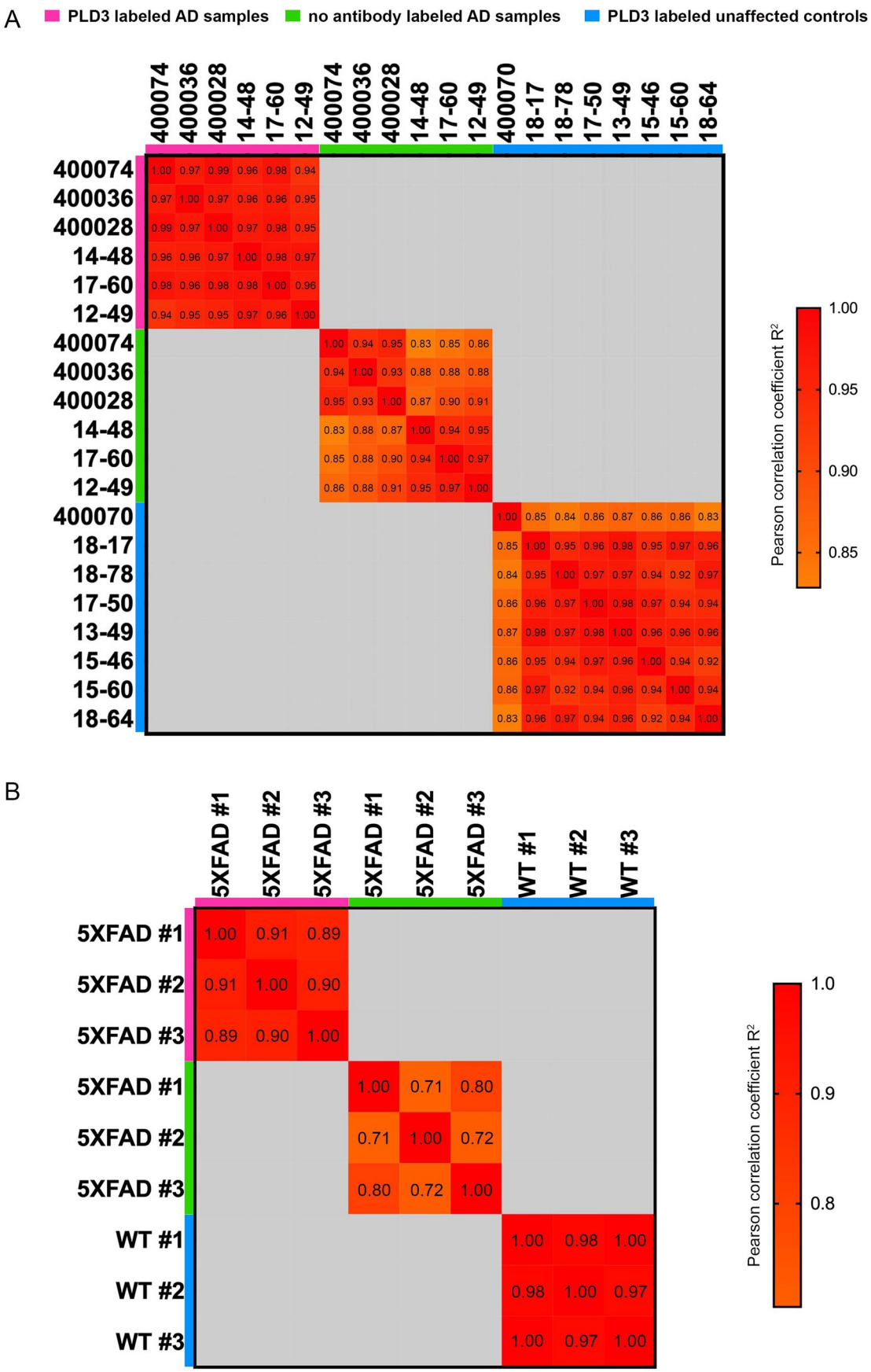

Extended Data Fig. 3 | Correlation analysis of proteomics samples in humans and mice. Correlation analysis among biological replicates of PLD3-labeled and no antibody-labeled proteomic samples in (**A**) humans and (**B**) mice. Pearson correlation coefficient R^2 of each comparison is listed in each box.

https://doi.org/10.1038/s43587-025-00823-3

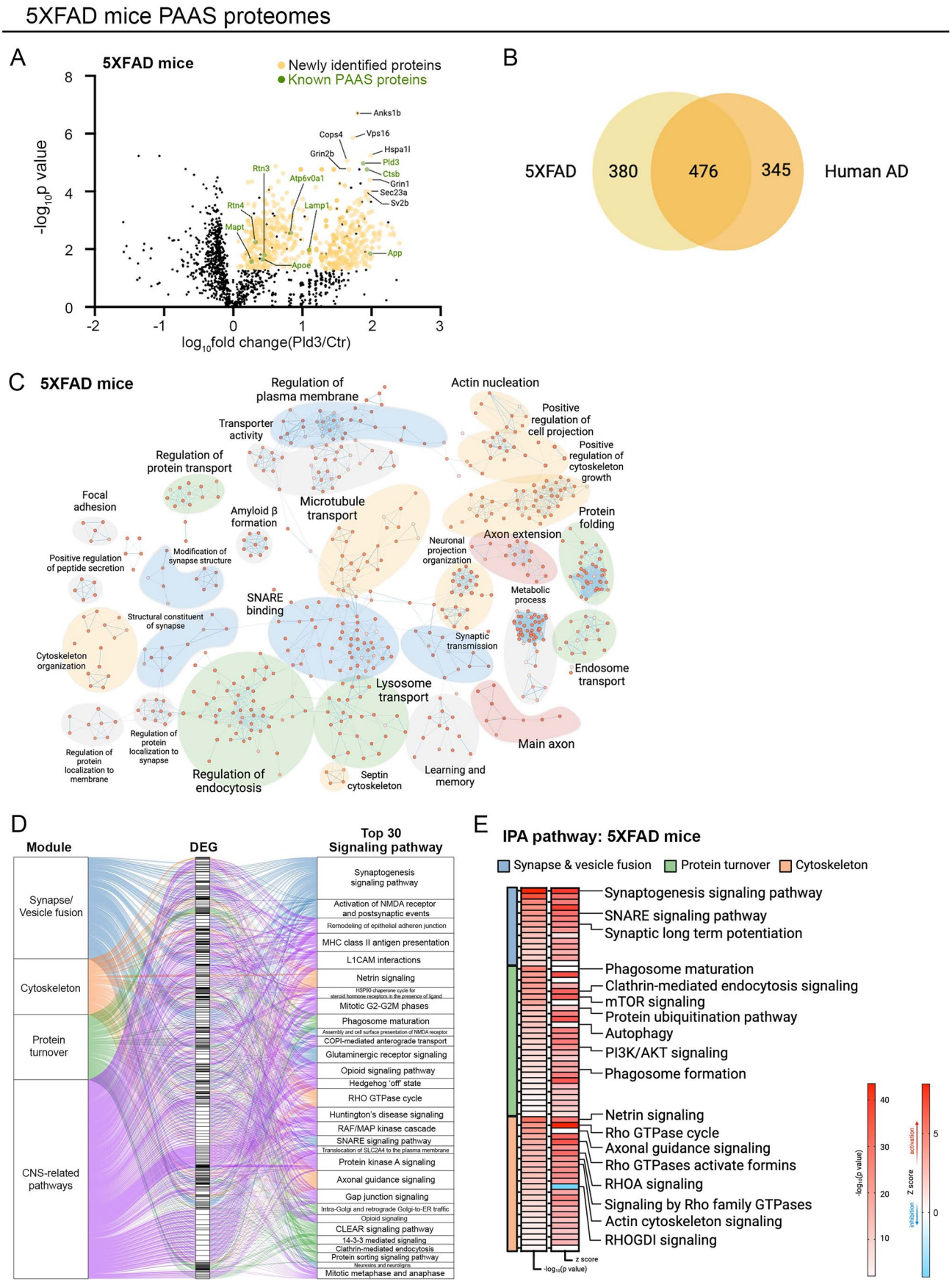

Extended Data Fig. 4 | See next page for caption.

https://doi.org/10.1038/s43587-025-00823-3

Extended Data Fig. 4 | Proteomics analysis of PLD3-labeled PAAS proteomes in 5XFAD mice. A. Volcano plot show proteins (represented by their gene names) that passed the statistical cutoffs (yellow dots) in 5XFAD mice. The top 10 proteomic hits with the lowest p-value and highest fold changes are indicated by their gene names in black. The selected known PAAS proteins are labeled as green dots and their gene names in green. The black dots among the yellow ones represent proteins being filtered by the statistical cutoff as shown in Fig. 2b. (See Table S1 for full list of proteomic hits). **B**. Venn diagram shows shared proteomics hits between AD humans and mice. **C**. Pathway enrichment analysis of PAAS proteome in 5XFAD mice. The Enrichment Map represents a network of pathways where edges connect pathways with many shared genes. Node color reflects the FDR of each pathway. The theme labels were curated based on the main pathways of each subnetwork. Subnetworks with a minimum of four pathways connected by edges are shown. **D**. IPA pathway analysis of the PAAS proteome in 5XFAD mice. Top 30 CNS-related signaling pathways are shown. The signaling pathways are summarized as 4 modules. The alluvium plot shows different modules connect to the differentially expressed genes (DEGs) and the DEGs connects to the pathways that they are involved. **E**. IPA pathways related to the three modules with a p-value less than 0.01 are listed. Heatmaps indicate either the $-\log_{10}$ (p-value) or the z score of each signaling pathway (pathways with a z score in red are predicted to be activated while blue ones are predicted to be inhibited). (**A, E**) Quantification was performed two-sided.

https://doi.org/10.1038/s43587-025-00823-3

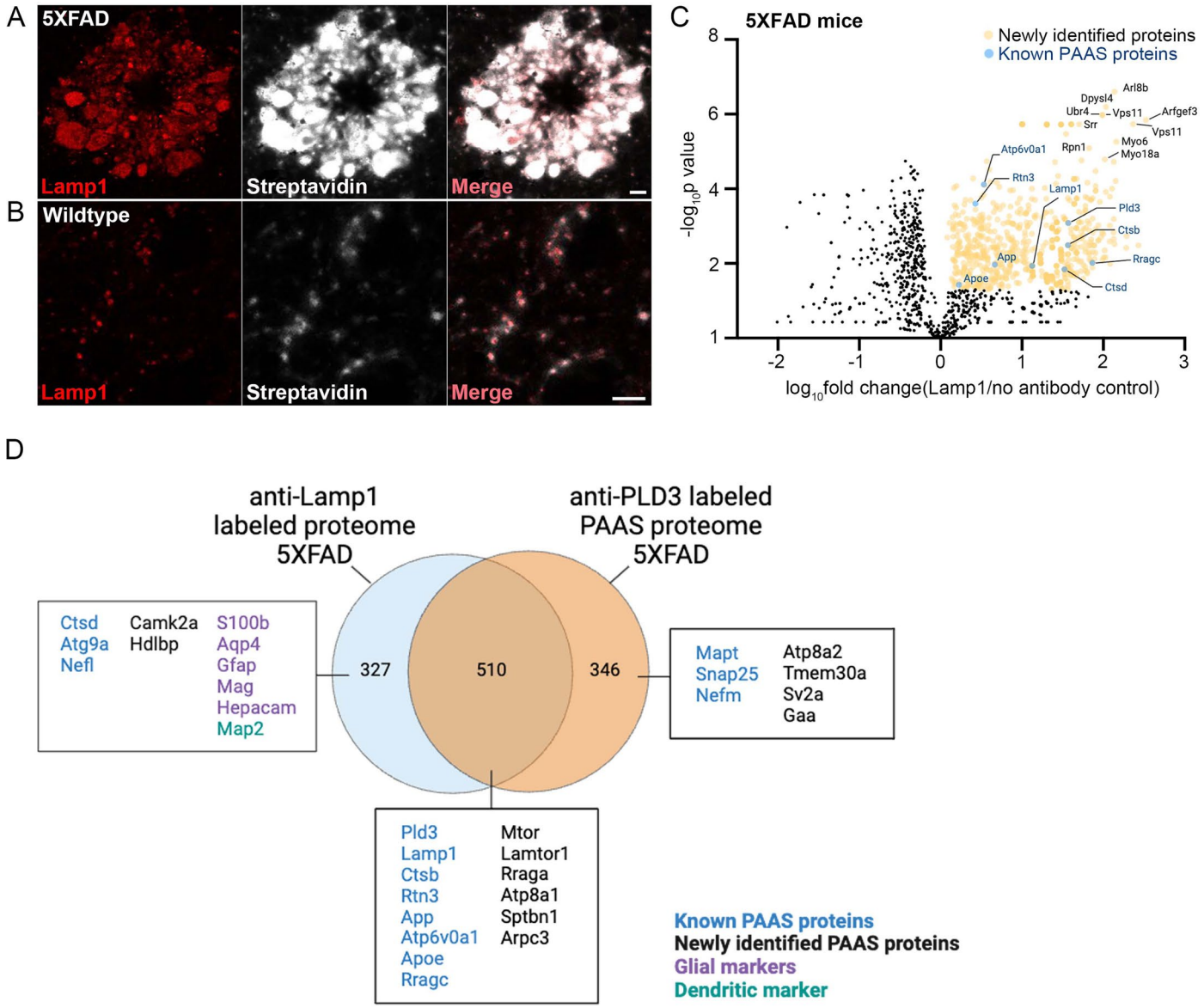

Extended Data Fig. 5 | Comparison between anti-Lamp1 antibody labeled proteome with the anti-PLD3 antibody labeled PAAS proteomes in 5XFAD mice. A-B. Proximity labeling of Lamp1 (red) in (**A**) 5XFAD and (**B**) wild type mice. Lamp1 (red) labeled (**A**) axonal spheroid halo in 5XFAD mice and (**B**) lysosomes in neuronal cell bodies. Biotinylated proteins were labeled by streptavidin. Scale bar 5 µm. **C.** Volcano plot shows proteins that passed the statistical cutoffs (yellow dots) in 5XFAD mice. The gene names of the top 10 proteomic hits with the lowest p-value and highest fold changes are shown in black. The selected known PAAS proteins are shown as dark blue dots with their gene names labeled in blue. Quantification was performed two-sided. (See Table S1 for full list of proteomic hits). **D.** Venn diagram showing comparison of the anti-Lamp1 antibody labeled proteomes with the anti-PLD3 antibody labeled PAAS proteomes in 5XFAD mice. Selected known PAAS proteins are shown in blue, newly identified proteins are shown in black, glial marker proteins are shown in purple and dendritic marker protein is shown in green.

https://doi.org/10.1038/s43587-025-00823-3

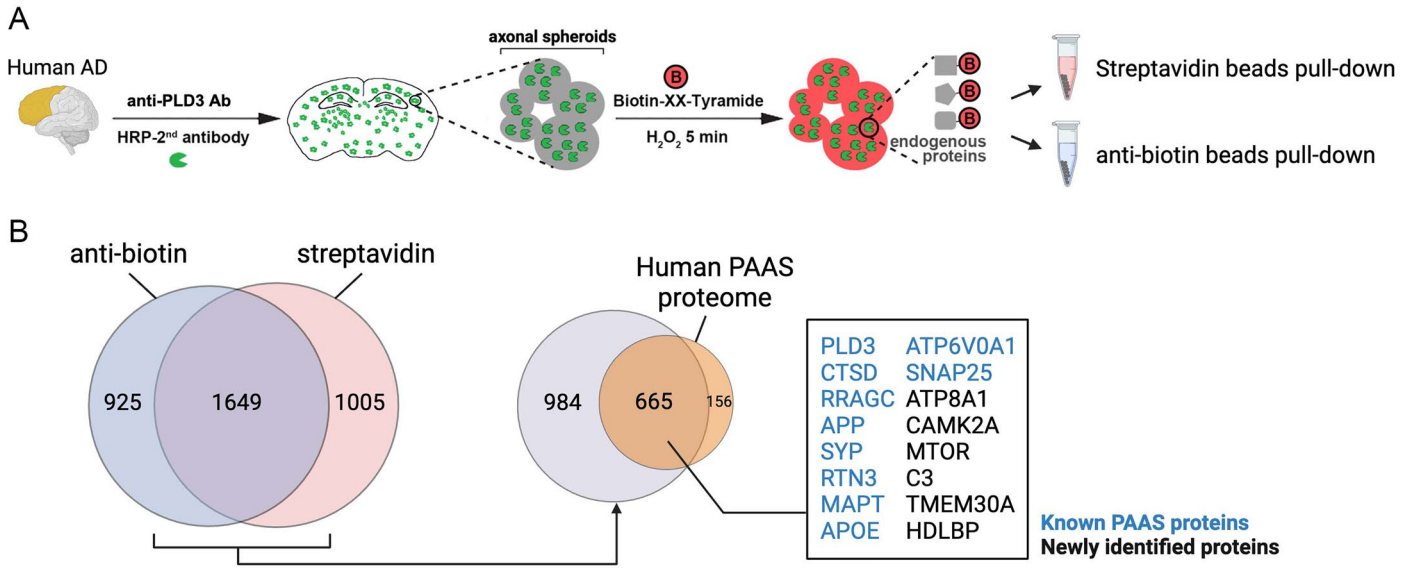

Extended Data Fig. 6 | Comparison between anti-biotin beads pulldown with streptavidin beads pulldown of anti-PLD3 antibody labeled proteomes in AD human brains. A. Schematic showing pipelines for using streptavidin beads or anti-biotin beads to pulldown anti-PLD3 antibody labeled proteomes in AD human brains. For streptavidin beads, tissue sections were lysed and then incubated with streptavidin beads. For anti-biotin beads, protein lysate was digested prior to anti-biotin beads pull down. **B**. Comparison of the proteomes captured using anti-biotin beads and those captured with streptavidin beads. Among the total 821proteomic hits identified in the human PAAS proteome, 665 hits were pulldown by both the streptavidin beads method and the anti-biotin beads method. Selected known PAAS proteins (blue) and newly identified proteins (black) are shown in the box.

https://doi.org/10.1038/s43587-025-00823-3

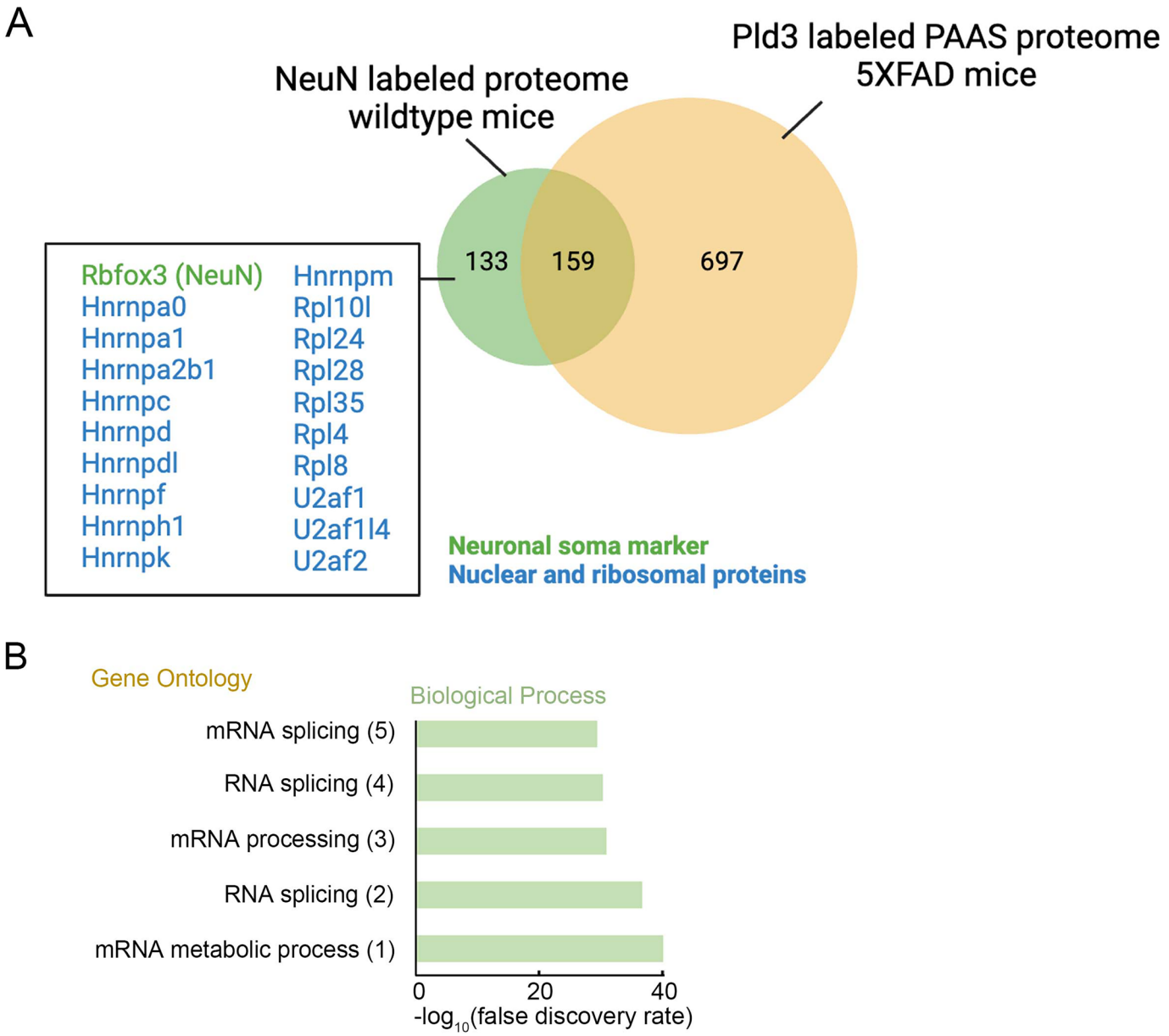

Extended Data Fig. 7 | Proteomics analysis of NeuN-labeled neuronal nuclei and perinuclear cytoplasm proteomes in mice. A. The NeuN-labeled neuronal nuclei and perinuclear cytoplasm proteomes in wildtype C57BL/6 J mice contain 292 proteomic hits. Comparison between the NeuN-labeled proteome and the PLD3-labeled PAAS proteome in mice showed 159 proteins are shared. Among the 133 unique protein hits in the anti-NeuN-labeled proteome, the protein bait and neuronal soma marker NeuN was detected, along with many nuclear and ribosomal proteins. **B** Gene Ontology analysis shows the top ranked biological process terms of the anti-NeuN-labeled proteomic dataset.

https://doi.org/10.1038/s43587-025-00823-3

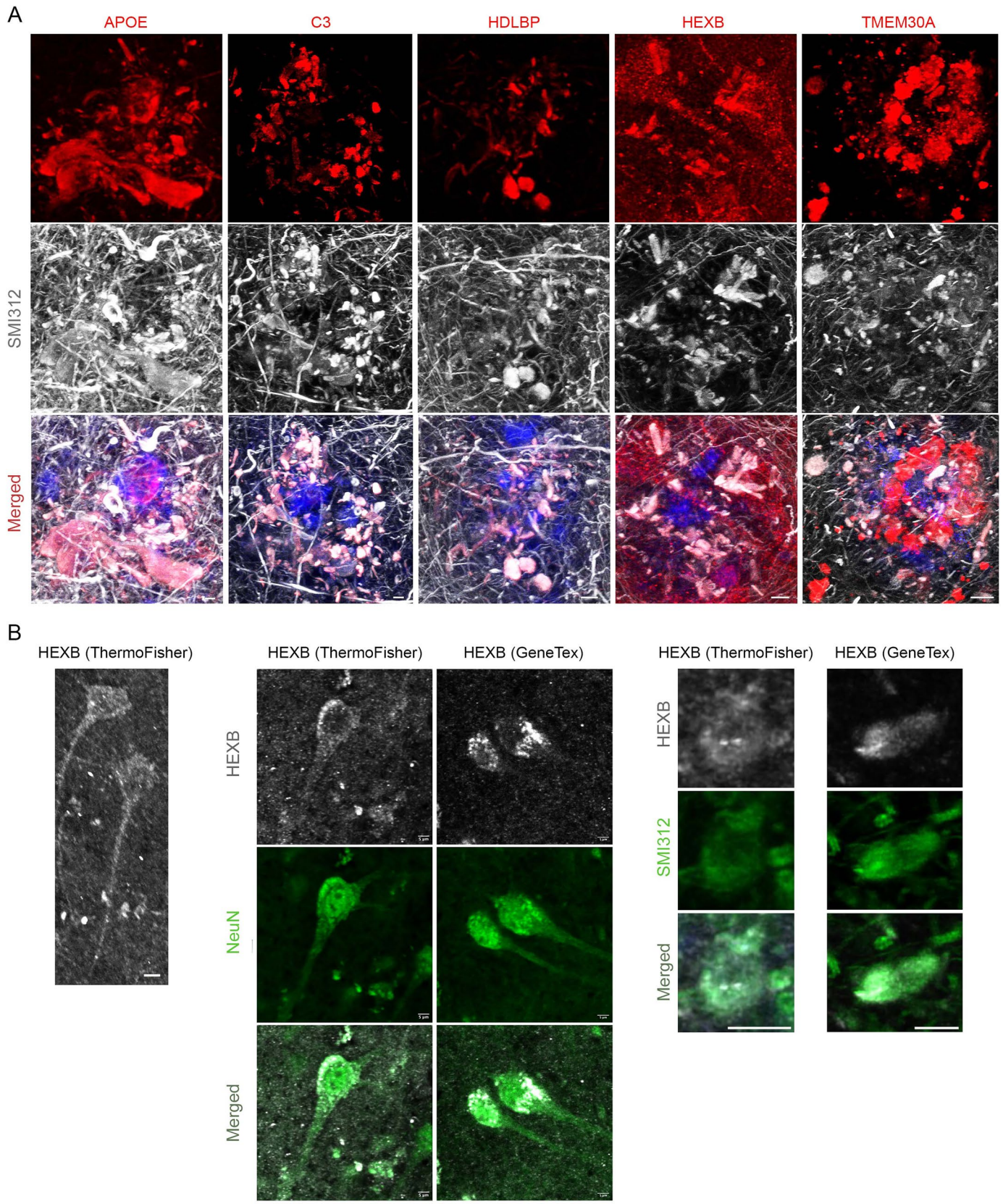

Extended Data Fig. 8 | See next page for caption.

https://doi.org/10.1038/s43587-025-00823-3

Extended Data Fig. 8 | Lipid transport-related proteins are expressed in axonal spheroids around amyloid plaques in AD human postmortem brains. **A**. Representative immunofluorescence confocal images of the top-ranked lipid-related proteomic hits, including APOE, HDLBP, C3, HEXB and TMEM30A in AD humans. Lipid transport-related proteins are shown in red. Neurofilament marker SMI312 (grey) indicates the neuronal branches, and axonal spheroid structures around amyloid plaques (ThioflavinS, blue). Scale bar = 5 µm. Quantification was performed in n = 3 AD human brains. Protein expression quantifications can be found in Table S2. **B**. Immunofluorescence confocal image shows HEXB (grey) expressed in neuronal cell bodies (NeuN, green) and axonal spheroids (SMI312, green) in AD human postmortem brain (n = 3). Two different HEXB antibodies were used for validation. Scale bar = 5 µm.

https://doi.org/10.1038/s43587-025-00823-3

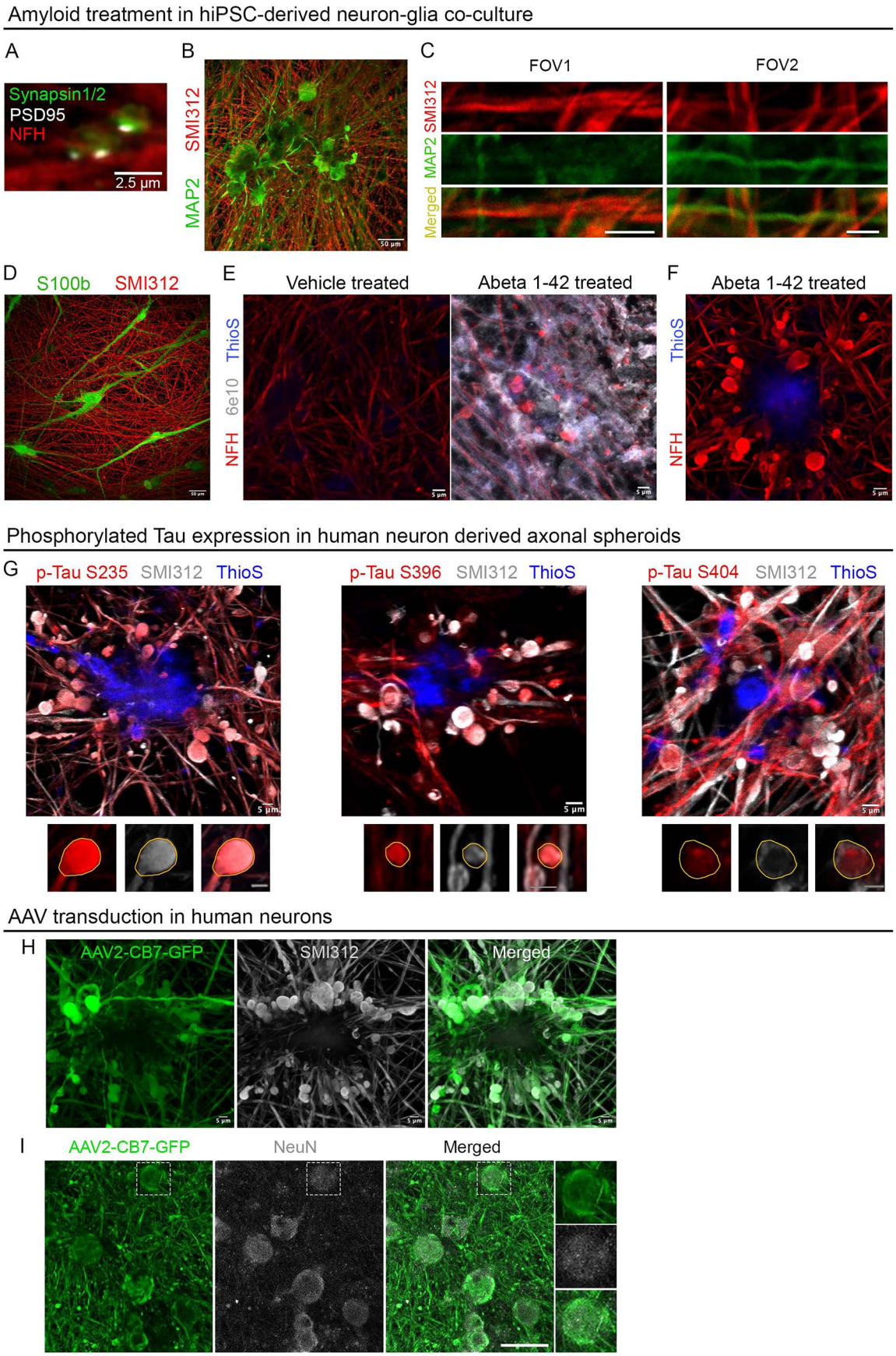

Extended Data Fig. 9 | See next page for caption.

https://doi.org/10.1038/s43587-025-00823-3

Extended Data Fig. 9 | Characterization of the human iPSC-derived neuron-astrocyte coculture AD model. A. Immunofluorescence confocal deconvolved image shows iPSC-derived human neurons (neurofilament H (NFH) labeled) robustly expressing pre- and post-synaptic markers (Synapsin1/2 and PSD95) at day 150 of coculture. Scale bar 2.5 µm. **B-C**. Immunofluorescence confocal image shows neuronal cell bodies and dendritic processes (MAP2 labeled), as well as axonal processes (SMI312 labeled) of iPSC-derived human neurons. (**B**) A low-zoom field of view (FOV). Scale bar 50 µm. (**C**) Two high-zoom FOVs showing dendritic and axonal processes. Scale bar 5 µm. **D**. Immunofluorescence confocal image shows the presence of both neurons (grey, SMI312) and astrocytes (red, S100b) in the coculture. Scale bar 50 µm. **E**. Immunofluorescence confocal images show 6e10 positive (grey) and ThioflavinS positive (blue) amyloid beta deposits formed in human iPSC-derived AD model following treatment with amyloid beta 1-42 peptides. Axonal processes were labeled with neurofilament (NFH, red). Scale bar 5 µm. **F**. Immunofluorescence confocal image shows axonal processes formed spheroids (NFH, red) around amyloid plaque deposit (ThioflavinS, blue). Scale bar 5 µm. **G**. Immunofluorescence confocal deconvolved images show phosphorylated Tau S235, S396 and S404 (red) expression in PAAS derived from human neurons (grey, SMI312). Zoom out images were maximum projected, while the zoom in images show a single plane. Scale bar 5 µm. **H-I**. Immunofluorescence confocal deconvolved images of AAV2-CB7-GFP infected (**H**) human neurons with abundant axonal spheroids (green, anti-GFP staining), co-stained with the axonal spheroid marker SMI312 (grey); (**I**) cell bodies of human neurons, as revealed by both anti-GFP (green) and anti-NeuN (grey) staining, related to Fig. 6o. Scale bar (**H**) 5 µm and (**I**) 50 µm.

https://doi.org/10.1038/s43587-025-00823-3

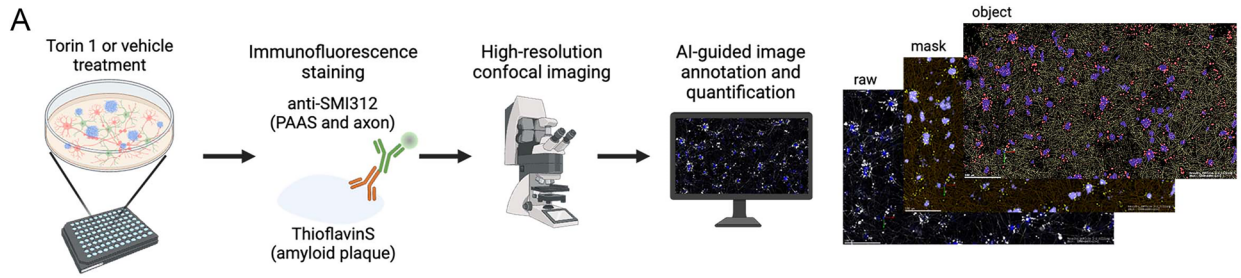

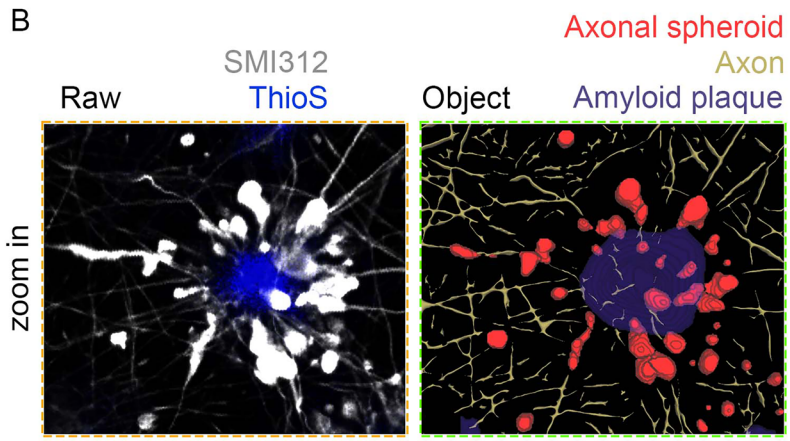

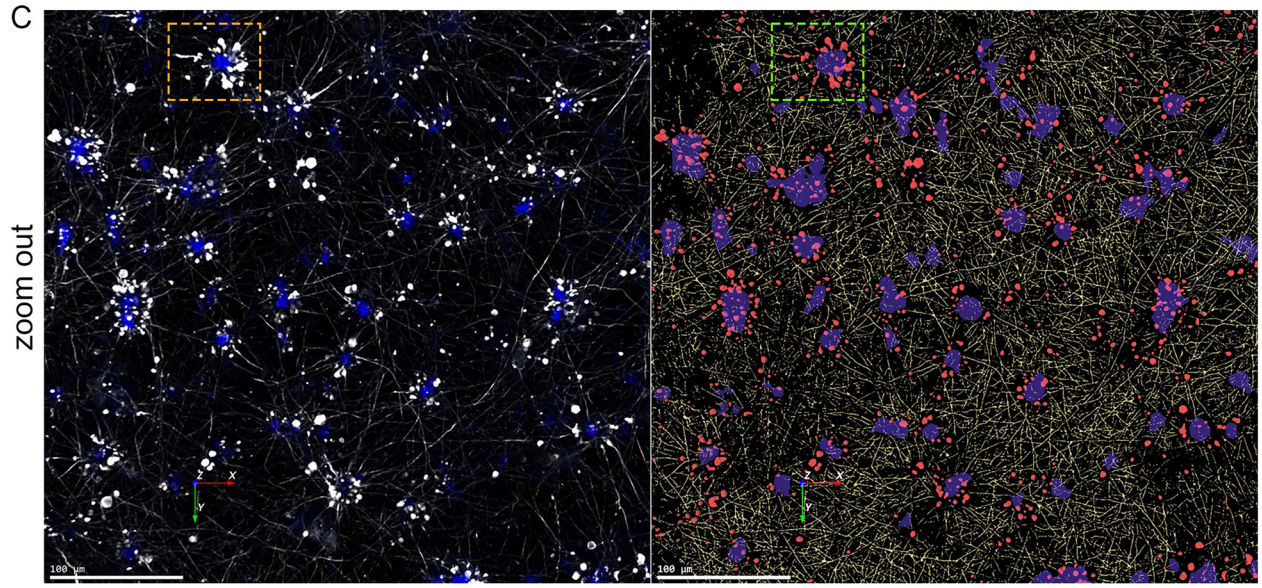

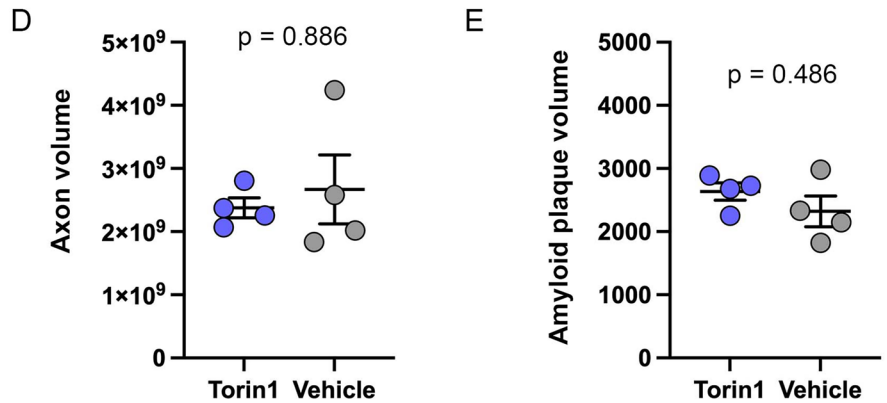

Extended Data Fig. 10 | See next page for caption.

https://doi.org/10.1038/s43587-025-00823-3

Extended Data Fig. 10 | High throughput automated quantification of axonal spheroids, axons and amyloid plaques in human iPSC-derived AD model. A. Schematic showing the workflow of immunofluorescence labeling of axonal spheroids, axons and amyloid plaques in human iPSC-derived AD model, followed by confocal imaging and machine learning-based image analysis and quantification. **B-C**. Zoom in (**B**) and zoom out (**C**) images of immunofluorescence confocal imaging showing SMI312 antibody labeled axonal spheroids and axons (white), ThioflavinS labeled amyloid plaque (blue). Objects of axonal spheroids (red), axons (yellow) and amyloid plaques (purple) were generated according to the raw images after image annotation and analysis. Scale bars = 100 µm. **D-E**. Quantification showing (**D**) axon and (**E**) amyloid plaque volume (related to the experiment in Figs. 6q and 6r). Mann Whitney test (two-tailed) was used for all the statistical analysis. Data are presented as mean values +/- SEM.

nature portfolio

Corresponding author(s): Jaime Grutzendler (Lead contact), Yifei Cai

Last updated by author(s): 06/28/2024

Reporting Summary

Nature Portfolio wishes to improve the reproducibility of the work that we publish. This form provides structure for consistency and transparency in reporting. For further information on Nature Portfolio policies, see our Editorial Policies and the Editorial Policy Checklist.

Statistics

For all statistical analyses, confirm that the following items are present in the figure legend, table legend, main text, or Methods section.

n/a	Confirmed	
☐	☒	The exact sample size (*n*) for each experimental group/condition, given as a discrete number and unit of measurement
☐	☒	A statement on whether measurements were taken from distinct samples or whether the same sample was measured repeatedly
☐	☒	The statistical test(s) used AND whether they are one- or two-sided *Only common tests should be described solely by name; describe more complex techniques in the Methods section.*
☐	☒	A description of all covariates tested
☐	☒	A description of any assumptions or corrections, such as tests of normality and adjustment for multiple comparisons
☐	☒	A full description of the statistical parameters including central tendency (e.g. means) or other basic estimates (e.g. regression coefficient) AND variation (e.g. standard deviation) or associated estimates of uncertainty (e.g. confidence intervals)
☐	☒	For null hypothesis testing, the test statistic (e.g. *F*, *t*, *r*) with confidence intervals, effect sizes, degrees of freedom and *P* value noted *Give P values as exact values whenever suitable.*
☒	☐	For Bayesian analysis, information on the choice of priors and Markov chain Monte Carlo settings
☐	☒	For hierarchical and complex designs, identification of the appropriate level for tests and full reporting of outcomes
☐	☒	Estimates of effect sizes (e.g. Cohen's *d*, Pearson's *r*), indicating how they were calculated

Our web collection on statistics for biologists contains articles on many of the points above.

Software and code

Policy information about availability of computer code

Data collection	All imaging data were collected using default software on the Leica confocal SP8 microscopy (Leica). All the LC-MS-MS data were collected using default software on a Thermo Scientific Q Exactive Plus system (Thermo Scientific).
Data analysis	Excel (Microsoft, v16.7), Prism (GraphPad v9), Qlucore Omics Explorer v3.6 (Qlucore AB, Lund, Sweden), CellProfiler v4.2.1 (Broad Institute), MATLAB (2020a), Python (v3.7), RStudio (4.0.2) and Aivia v12 were used for data analysis and plotting. Custom codes for FIJI and MATLAB were deposited at GitHub (https://github.com/PaulYJ/Axon-spheroid) as we previously described (Yuan et al., ...Grutzendler, Nature, 2022). The Python code for the analysis of calcium imaging data can be accessed at the following location: https://github.com/ShawnQin/calcium_trace. The code for the analysis of STED imaging data can be accessed at the following location: https://github.com/bewersdorflab/Yifei-Lukas-Collab. Peptide identification was analyzed using Proteome Discoverer software v2.2 (Thermo Scientific). Data searching was performed using the Mascot algorithm (version 2.6.1) (Matrix Science) against the SwissProtein database with taxonomy restricted to human (20,368 sequences) or mouse (17,034 sequences) as well as a streptavidin sequence. Scaffold v5.1.2 (Proteome Software Inc., Portland, OR) was used to validate MS/MS-based peptide and protein identifications. The enrichment map was visualized in Cytoscape (v3.9.1). Pathway analysis was performed using Ingenuity Pathway Analysis (IPA) software (QIAGEN, 2022 release version). Gene set enrichment analysis was performed using Broad Institute GSEA software 4.3.2. Principal component analysis was performed using Qlucore Omics Explorer v3.6 (Qlucore AB, Lund, Sweden).

For manuscripts utilizing custom algorithms or software that are central to the research but not yet described in published literature, software must be made available to editors and reviewers. We strongly encourage code deposition in a community repository (e.g. GitHub). See the Nature Portfolio guidelines for submitting code & software for further information.

Data

Policy information about availability of data

All manuscripts must include a data availability statement. This statement should provide the following information, where applicable:

- Accession codes, unique identifiers, or web links for publicly available datasets
- A description of any restrictions on data availability
- For clinical datasets or third party data, please ensure that the statement adheres to our policy

DATA AND CODE AVAILABILITY
Raw proteomics data is provided in Table S1. The mass spectrometry proteomics data have been deposited to the ProteomeXchange Consortium via the PRIDE partner repository with the dataset identifier PXD040310. Reviewer account details: Username: reviewer_pxd040310@ebi.ac.uk, Password: jk3QiALg). The Lamp1 dataset is under the identifier PXD048097, username: reviewer_pxd048097@ebi.ac.uk, password: VXnYLyuk. For sample information see Table S3.

SwissProt database can be accessed here:https://www.uniprot.org/uniprotkb?query=*&facets=reviewed%3Atrue%2Cmodel_organism%3A9606.
Tissue Atlas in The Human Protein Atlas can be accessed here: https://www.proteinatlas.org/humanproteome/tissue
GeneOntology.org database can be accessed here: https://geneontology.org/.
g:profiler database can be accessed here: https://biit.cs.ut.ee/gprofiler/gost
ToppGene Suite search portal can be accessed here: https://toppgene.cchmc.org/
Single cell transcriptomics database can be accessed here: https://brainrnaseq.org/.

Custom codes for FIJI and MATLAB were deposited at GitHub (https://github.com/PaulYJ/Axon-spheroid) as we previously described [4].

The Python code for the analysis of calcium imaging data can be accessed at the following location: https://github.com/ShawnQin/calcium_trace.

The code for the analysis of STED imaging data can be accessed at the following location: https://github.com/bewersdorflab/Yifei-Lukas-Collab.

Human research participants

Policy information about studies involving human research participants and Sex and Gender in Research.

Reporting on sex and gender	The use of postmortem samples is considered 'non-human subject' research. Snap-frozen postmortem human brain specimens of frontal cortices from AD patients and age-matched controls were obtained from the Yale Alzheimer's Disease Research Center and the Banner Sun Health Research Institute. Detailed demographic and clinical information can be found in Figure S1. For proximity labeling proteomics, 6 AD cases with intermediate to high AD level and 8 age-matched unaffected controls were used. To reduce inter-sample variability and maximize signal-to-noise by avoiding brains with low-density amyloid deposition, we carefully inspected ~ 40 individual postmortem brains using microscopy and selected for proteomic analysis 6 AD brains with the highest density of amyloid plaques and axonal spheroids within the frontal cortex. The grey matter regions with high plaque load were microdissected out from AD brain sections using a Leica stereomicroscope. Similarly, the grey matter regions were dissected from unaffected control brain sections. For immunofluorescence proteomic validations, 25 severe AD cases and 14 unaffected control cases were used (Figure S1).
Population characteristics	The use of postmortem samples is considered 'non-human subject' research. 6 AD cases with intermediate to high AD level and 8 age-matched unaffected controls were used. To reduce inter-sample variability and maximize signal-to-noise by avoiding brains with low-density amyloid deposition, we carefully inspected ~ 40 individual postmortem brains using microscopy and selected for proteomic analysis 6 AD brains with the highest density of amyloid plaques and axonal spheroids within the frontal cortex. The grey matter regions with high plaque load were microdissected out from AD brain sections using a Leica stereomicroscope. Similarly, the grey matter regions were dissected from unaffected control brain sections. For immunofluorescence proteomic validations, 25 severe AD cases and 14 unaffected control cases were used (Figure S1).
Recruitment	No donors were recruited by this study.
Ethics oversight	The use of postmortem samples is considered 'non-human subject' research.

Note that full information on the approval of the study protocol must also be provided in the manuscript.

Field-specific reporting

Please select the one below that is the best fit for your research. If you are not sure, read the appropriate sections before making your selection.

☒ Life sciences ☐ Behavioural & social sciences ☐ Ecological, evolutionary & environmental sciences

For a reference copy of the document with all sections, see nature.com/documents/nr-reporting-summary-flat.pdf

Life sciences study design

All studies must disclose on these points even when the disclosure is negative.

Sample size	No statistical power analysis was used to determine sample sizes, but our sample sizes were similar to those generally employed in the field. Three to six biological replicates were used for animal experiments, and six to ten biological replicates were used for human postmortem brain tissue studies (Yuan et al., Nature, 2022; Yuan et al., Neuron 2016).
Data exclusions	No data were excluded from analysis.
Replication	For proximity labeling proteomics, 6 AD human cases with intermediate to high AD level and 8 age-matched unaffected controls were used. For mice proximity labeling proteomics, 3 5XFAD mice and 3 age-matched wildtype mice were used. For immunofluorescence proteomic validations, 25 severe AD human cases and 14 unaffected control cases were used. 3 5XFAD mice and 3 age-matched wildtype mice were used. For AAV2-mediated in vivo molecular manipulation, 5 AD mice and 5 control mice were used. For AAV.PHPeB-mediated in vivo manipulation, 3 AD mice and 3 control mice were used. For in vivo puromycylation, 3 AD mice were used for anisomycin or 3 for vehicle comparison, 3 AD mice were used for Torin1 treatment or 3 or control, 1 mTOR-homozygous mouse was used, 4 mTOR-heterozygous mice were used. For RNAscope, 3 AD mice were used. For human iPSC modeling, two fully characterized, de-identified control human iPSC lines NSB3182-3 (female) and NSB2607 (male) were used in all experiments. No biological replicates were excluded. Usually, 3 mice or human samples were used to test and optimize the protocol, before proceeding to final experiments with large cohorts.
Randomization	For proximity labeling proteomics, 6 AD cases with intermediate to high AD level and 8 age-matched unaffected controls were used. To reduce inter-sample variability and maximize signal-to-noise by avoiding brains with low-density amyloid deposition, we carefully inspected ~ 40 individual postmortem brains using microscopy and selected for proteomic analysis 6 AD brains with the highest density of amyloid plaques and axonal spheroids within the frontal cortex. The grey matter regions with high plaque load were microdissected out from AD brain sections using a Leica stereomicroscope. Similarly, the grey matter regions were dissected from unaffected control brain sections. For immunofluorescence proteomic validations, 25 severe AD cases and 14 unaffected control cases were used. Humans or mice samples were grouped based on their disease stages. Mice were also paired with littermate and sex as described in the method section.
Blinding	Although sample preparation and processing were not performed blindly due to the different condition of treatments, all samples and data were processed in a high-throughput or automated fashion. For the non-automated steps of sample and data processing, all samples and data were processed in a consistent manner.

Reporting for specific materials, systems and methods

We require information from authors about some types of materials, experimental systems and methods used in many studies. Here, indicate whether each material, system or method listed is relevant to your study. If you are not sure if a list item applies to your research, read the appropriate section before selecting a response.

Materials & experimental systems

n/a	Involved in the study
☐	☒ Antibodies
☐	☒ Eukaryotic cell lines
☒	☐ Palaeontology and archaeology
☐	☒ Animals and other organisms
☒	☐ Clinical data
☒	☐ Dual use research of concern

Methods

n/a	Involved in the study
☒	☐ ChIP-seq
☒	☐ Flow cytometry
☒	☐ MRI-based neuroimaging

Antibodies

Antibodies used	Full list of primary antibodies for newly validated and known PAAS proteins can be found in Table S2, including catalog number, RRID, dilution factors and brief staining instructions. Primary antibodies: (name, Catalog number, manufacturer, RRID) Anti-PLD3 antibody, HPA012800 Atlas antibody RRID:AB_1855330; anti-SMI312, 837904 Biolegend RRID:AB_2566782; anti-Cathespin D (CatD), AF1014 R&D Systems RRID:AB_2087218; Anti-Lamp1, 1D4B (mouse) Developmental Studies Hybridoma Bank RRID:AB_2134500; anti-Cathespin B (CatB), AF965 (mouse) NOVUS BIOLOGICALS RRID:AB_2086949; anti-GAA, HPA029126 Atlas antibody RRID:AB_2672918; anti-GBA, NBP1-32271 NOVUS BIOLOGICALS RRID:AB_2109073; anti-TPP1, NBP1-31758 NOVUS BIOLOGICALS RRID:AB_2205907; anti-ATP6V0A1, PA5-54570 ThermoFisher RRID:AB_2638371;

anti-SYT11, HPA064091 Atlas antibody RRID:AB_2685189;
anti-G3BP1, 13057-2-AP Proteintech RRID:AB_2232034;
anti-G3BP2, HPA018304 Atlas antibody RRID:AB_1849350;
anti-ITM2B, HPA029292 Atlas antibody RRID:AB_10601917;
anti-SPTBN1, HPA012685 Atlas antibody RRID:AB_1857433;
anti-SV2A, HPA007863 Atlas antibody RRID:AB_1080135;
anti-ATP2B3, HPA001583 Atlas antibody RRID:AB_1079641;
anti-CAMK2A, MAB7280-SP R&D Systems N/A;
anti-Calmodulin, NB120-2860 NOVUS BIOLOGICALS RRID:AB_2069288;
anti-SYT1, MAB4364 R&D Systems RRID:AB_2199304;
anti-CACNA2D1, NB120-2864 NOVUS BIOLOGICALS RRID:AB_789591;
anti-CACNA1B, PA5-77296 Invitrogen RRID:AB_2735588;
anti-NTRK2, HPA007637 Atlas antibody RRID:AB_1080385;
anti-mTOR, CST#2983T CST RRID:AB_2105622;
anti-p-mTOR S2448, 2971S CST RRID:AB_330970;
anti-PIK3R4, HPA036032 Atlas antibody RRID:AB_10610281;
anti-puromycin-647, MABE343-AF647 RRID:AB_2736876
anti-AKT1, HPA002891 Atlas antibody RRID:AB_1078123;
anti-LAMTOR, NBP1-71689 NOVUS BIOLOGICALS RRID:AB_11017573;
anti-RAGA, #4357 CST RRID:AB_10545136;
anti-RAGC, #9480 CST RRID:AB_10614716;
anti-RHEB, NBP2-75646 NOVUS BIOLOGICALS N/A;
anti-RAPTOR, 424000 ThermoFisher RRID:AB_2533523;
anti-HDLBP, 15406-1-AP Proteintech RRID:AB_2117367;
anti-APOE, ab183597 abcam N/A;
anti-C3, PA5-21349 ThermoFisher RRID:AB_11153785;
anti-HEXB, PA5-101082 ThermoFisher RRID:AB_2850526;
anti-TMEM30A, NBP1-59474 NOVUS BIOLOGICALS RRID:AB_11015954;
anti-ATG9A, NB110-56893SS NOVUS BIOLOGICALS RRID:AB_920677;
anti-Ubiquitin, U5379 Sigma RRID:AB_477667;
anti-RTN3, ABN1723 Millipore Sigma N/A;
anti-synaptophysin, ab14692 abcam RRID:AB_301417;
anti-SNAP25, 111 002 synaptic system RRID:AB_887790;
anti-VAMP2, #13508 CST RRID:AB_2798240;
anti-beta Tubulin III, ab18207 abcam RRID:AB_444319;
anti-GFP (1:500, Aves Labs, Cat# GFP-1020, RRID:AB_10000240);
anti-RFP (1:200, Rockland Cat# 600-401-379, RRID:AB_2209751);
anti-neurofilament H (1:1000, EnCor Biotechnology Cat# CPCA-NF-H, RRID:AB_2149761),
anti-NeuN (1:1000, Abcam Cat# ab104224, RRID:AB_10711040),
anti-NeuN (1:200, Abcam Cat# ab177487, RRID:AB_2532109),
anti-Synapsin1/2 (1:500, Synaptic Systems Cat# 106 006, RRID:AB_2622240),
anti-PSD95 (1:200, Millipore Cat# MABN68, RRID:AB_10807979),
anti-S100b (1:500, Synaptic Systems Cat# 287 011, RRID:AB_2814881),
anti-IBA1 (1:100, Wako #019-19741, RRID:AB_2891289);
anti-6e10 (1:200, BioLegend Cat# 803015, RRID:AB_2565328);
anti-phospho-Tau S235, PA5-104785 Invitrogen RRID:AB_2816258;
anti-phospho-Tau S396, 44-752G ThermoFisher RRID:AB_2533745;
anti-phospho-Tau S404, 20194T CST RRID:AB_2798837;
mTOR substrate antibody sampler kit (CST #9862);
anti-4E-BP1 antibody (CST #9452);
anti-MAP2 (1:200, Abcam Cat# ab32454, RRID:AB_776174).
Secondary antibody:
Alexa dye-conjugated secondary antibodies were used (ThermoFisher Scientific).

Validation

All antibodies were commercially available and have been tested by the manufacturers, and also have been cited by other publications (references are available on the manufacturers websites).

Eukaryotic cell lines

Policy information about cell lines and Sex and Gender in Research

Cell line source(s)	Two fully characterized, de-identified control human iPSC lines NSB3182-3 (female) and NSB2607 (male) were used in all experiments (Hoffman et al., Nature Communication 2017). NGN2-induced glutamatergic neurons were generated and co-cultured with human primary astrocytes (ThermoFisher #N7805200, or ScienCell #1800) for all experiments. HEK 93T cells (Invitrogen, R700-07) were used for lentivirus packaging.
Authentication	iPSC lines showed typical morphology of iPSC colonies, after differentiation into human neurons, neuronal markers NeuN, TUJ1, MAP2, SMI312, PSD92, Synapsin1/2 were tested by immunofluorescence staining. Human primary astrocytes were tested by S100b immunofluorescence staining.
Mycoplasma contamination	The cell lines used were negative for mycoplasma contamination.
Commonly misidentified lines (See ICLAC register)	No commonly misidentified cell lines were used.

Animals and other research organisms

Policy information about studies involving animals; ARRIVE guidelines recommended for reporting animal research, and Sex and Gender in Research

Laboratory animals	All animal procedures were approved by the Institutional Animal Care and Use Committee at Yale University. WT (C57BL/6J), 5XFAD (Tg6799) mice and mTOR-flox (JAX #011009) mice were obtained from Jackson Laboratory. 5XFAD and WT mice, used for proximity labeling proteomics, were euthanized at 15-month-old, followed by transcardial perfusion. Three male mice per genotype (WT and 5XFAD) were used. Animals used for immunofluorescence proteomic validation were euthanized at 2-3 or 12-15 months of age, with 3 biological replicates per experiment. mTOR-flox mice were cross-bred with 5XFAD mice to create an mTOR-flox-5XFAD line. For AAV-mediated mTOR heterozygous knockout experiments, mTOR-flox-5XFAD mice were injected with AAVs at 6 weeks of age. Five biological replicates (combining male and female mice) in each group were used for AAV9-hSyn-cre-2a-tdT experiment, and 3 male mice in each group were used for AAV-PHPeB experiment.
Wild animals	No wild animals were used.
Reporting on sex	Equal sex of male and female animals have been used for proteomics analysis (3 male and 3 female mice). For in vivo genetic manipulation experiments, we tried to match sex, age and genotype as much as we can. For AAV2-mediated knockout in mice, 3 male and 2 female were used for each group. For AAV.PHPeB knockout in mice, 3 male mice were used in treatment group and 3 male were used in control group.
Field-collected samples	No field-collected samples were used.
Ethics oversight	Yale University IACUC 2023-11438.

Note that full information on the approval of the study protocol must also be provided in the manuscript.